Université de Montréal

Cell wall mediated regulation of plant cell morphogenesis: pectin esterification and cellulose crystallinity

par

Bara Altartouri

Département de Sciences Biologiques, Institut de Recherche en Biologie Végétale
Faculté des Arts et des Sciences

Thèse présentée à la Faculté des Arts et des Sciences
en vue de l'obtention du grade de doctorat
en Sciences Biologiques

Mai, 2019

Résumé

La morphogenèse cellulaire est une composante fondamentale du développement d'un organisme. Toute cellule végétale est entourée de parois régulant sa morphogenèse. Cette matrice extra-cellulaire est principalement composée de polysaccharides. Afin de montrer le lien entre la forme et la fonction d'une cellule il est primordial de comprendre la façon dont ces polysaccharides sont modifiés durant le développement et l'expansion cellulaire. Chez les plantes, la mécanique de l'expansion cellulaire est principalement régulée par la cellulose, le biopolymère le plus abondant sur Terre. Comme les microfibrilles de cellulose présentent une forte résistance à la traction le long de leur axe d'orientation principal, elles réguleraient le processus d'expansion en conférant des propriétés mécaniques aux composants pariétaux qui contrôlent l'ampleur et la directivité de la croissance expansive au niveau subcellulaire. Les homogalacturonanes, type de pectine le plus abondant des parois cellulaires primaires, sont des biopolymères également susceptibles d'agir sur l'expansion cellulaire. La distribution spatiale et le degré d'estérification des pectines homogalacturonanes affectent les propriétés mécaniques de la paroi et par conséquent le pattern d'expansion. J'ai utilisé une approche génétique combinée à des stratégies novatrices de biochimie, de biomécanique et d'imagerie, afin de comprendre comment la dynamique spatio-temporelle de la cellulose et des homogalacturonanes régule l'expansion et la morphogenèse cellulaires. Pour ce faire, je me suis basé sur l'étude de deux types de cellules épidermiques de formes différentes: celles du cotylédon et de l'hypocotyle d'*Arabidopsis thaliana*. J'ai prouvé que la formation des ondulations des cellules fondamentales du cotylédon nécessite des modifications spatiales et temporelles des microfibrilles de cellulose et des pectines déméthylestérifiées. Ces modifications régulent la rigidité mécanique de la paroi péricline à deux moments distincts : lors de l'initiation de la formation du lobe et lors de son expansion ultérieure. L'initiation de la formation du lobe requiert une augmentation de la rigidité de la paroi péricline au niveau des potentielles saillies de l'ondulation, et ce par une accumulation locale de pectines déméthylestérifiées. L'expansion ultérieure est quant à elle contrôlée par le degré de cristallinité de la cellulose et par l'alignement perpendiculaire des microfibrilles tangentiellement aux saillies de l'ondulation de la paroi péricline. Durant l'élongation et l'expansion anisotrope des cellules épidermiques de l'hypocotyle, la cellulose et les pectines homogalacturonanes jouent des rôles distincts lors de chaque phase d'élongation. Durant la première phase de développement, une réduction du taux de pectines déméthylestérifiées diminue la rigidité de la paroi et accélère l'élongation des cellules. Lors de la seconde phase du développement, une réduction de la cristallinité de la cellulose diminue la vitesse d'élongation de l'hypocotyle. À partir de l'étude des deux systèmes cellulaires, nous pouvons conclure que, contrairement à l'hypothèse acceptée de longue date, la cellulose ne serait pas un élément essentiel au déclenchement d'évènements morphogénétiques mais qu'elle jouerait plutôt un rôle au sein de mécanismes de rétroaction accentuant le processus de morphogenèse. De plus, la morphogenèse induite par des contraintes joue un rôle clé lors des étapes initiales et serait dépendante du degré d'estérification des pectines. Mes expériences permettent de corréler les données de mécanique cellulaire expérimentale à la biologie cellulaire fonctionnelle et à la génétique.

Mots-clés : morphogenèse, développement, expansion cellulaire, paroi cellulaire, cellulose, cristallinité, estérification des pectines, microtubules corticaux, microscopie de Brillouin, microscopie à fluorescence polarisée.

Abstract

Cellular morphogenesis is a fundamental underpinning of development. All cells in the plant kingdom are surrounded by walls that govern shape formation. This extracellular matrix is composed mainly of polysaccharides. How these polysaccharides are modified during cellular development to regulate cell expansion, and thus cell shape, must be understood to link form with function. In plants, the mechanical aspect of cell expansion is known to be mainly influenced by cellulose, the most abundant biopolymer on Earth. Because cellulose microfibrils exhibit a strong tensile strength along their long axis, they may be used to control the expansion process by conferring mechanical properties to the cell wall material that determine the directionality and the magnitude of expansive growth at subcellular level. Another wall polymer that may influence cell expansion is homogalacturonan pectin, the most abundant type of pectin in the primary wall. The spatial distribution and esterification status of homogalacturonan pectin may affect the mechanical aspects of the wall and, therefore, the expansion pattern. I used a genetic approach combined with novel biochemical, biomechanical and imaging strategies to study the impact of the spatio-temporal dynamics of cellulose and homogalacturonan pectin during cell expansion and shape formation. I investigated cell shape formation in two differently shaped types of epidermal cells: those of the cotyledon and of the hypocotyl of *Arabidopsis thaliana*. I show that undulation formation in pavement cells of the cotyledon requires spatial and temporal changes of cellulose microfibrils and demethyl-esterified pectin. These changes regulate the mechanical stiffness of the periclinal wall at two different stages: lobe initiation and subsequent expansion. Lobe initiation involves an increase in the stiffness of the periclinal wall at the prospective neck region of the undulation through a local accumulation of demethyl-esterified pectin. The subsequent expansion is controlled by the degree of cellulose crystallinity and the perpendicular alignment of the microfibrils at the tangent of the neck side of the undulation at the periclinal wall. During the elongation process and the anisotropic expansion of the epidermal hypocotyl cells, cellulose and homogalacturonan pectin make distinct contributions in each developmental phase of the elongation. During the first developmental phase, reduction in the proportion of demethyl-esterified pectin decreases the wall stiffness and accelerates the elongation. A reduction in the cellulose crystallinity decreases the elongation of the hypocotyl at the second developmental phase. It may be concluded from the two cell systems that cellulose, contrary to a long-established hypothesis, may not be essential for the initiation of morphogenetic events and their function may be reassigned to the feedback-mediated augmentation of cell shaping processes. Moreover, stress-induced shape formation plays a key role during the initiating steps and it is likely to be dominated by the degree of pectin esterification. My data link experimental cell mechanics to functional cell biology and genetics.

Keywords: Morphogenesis, development, cell expansion, cell wall, cellulose, crystallinity, pectin esterification, cortical microtubule, Brillouin microscopy, polarized fluorescence microscopy.

Table of contents

List of figures

List of movies

List of abbreviations and symbols

a.u.	Arbitrary unit
µm	Micrometer
µM	Micromolar
µN	Micronewton
AFM	Atomic force microscopy
any1	Anisotropy1
ATR-FTIR	Attenuated total reflection-fourier transform infrared spectroscopy
BFS	Brillouin frequency shift
BSA	Bovine serum albumin
CESA	Cellulose synthase
CGA	1-cyclohexyl-5-(2,3,4,5,6-pentafluorophenoxy)-1λ4,2,4,6-thiatriazin-3-amine
CLSM	Confocal laser scanning microscopy
cm	Centimeters
COS^{488}	Chitosan oligosaccharides conjugate with Alexa Fluor 488
CSC	Cellulose synthase complex
CSI1	Cellulose synthase interactive protein 1
DAG	Day after germination
DCB	2,6-dichlorobenzonitrile
DMSO	Dimethyl sulfoxide
FucAl	Fucose-Alkyne
g	Gram
GalA	Galacturonic acid
gf	Gram-force
GFP	Green fluorescent protein
GHz	Gigahertz
GPa	Gigapascal
GPI	Glycophosphatidylinositol
H	Hour
HG	Homogalcturonan
Ig	Immunoglobulin
kV	Kilovolt
LP	Left primer
LVDT	Linear variable differential transformer
M	Molar
M'	Longitudinal modulus
mA	Milliampere

mg	Milligram
ml	Milliliter
mm	Millimeter
mM	Millimolar
MPa	Megapascal
MS	Murashige and Skoog
mW	Milliwatts
N	Newton
n	Refractive index
NA	Numerical aperture
nm	Nanometer
nM	Nanomolar
p	Fluorescence polarization
PBS	Phosphate buffer saline
PCR	Polymerase chain reaction
PI	Propidium iodide
PME	Pectin Methylesterase
PMEI	Pectin Methylesterase Inhibitor
POLScope	Polarized light microscopy
RGI	Rhamnogalacturonan I
RGII	Rhamnogalacturonan II
Rha	Rhamnose
Rho	Ras homologous
ROI	Region of interest
RP	Right primer
s	Second
S4B	Pontamine Fast Scarlet 4B
SE	Standard error
T-DNA	Transfer Deoxyribonucleic acid
TIRF	Total internal reflection fluorescence
TUB6	Tubulin6
v/v	Volume/volume
w/v	Weight/volume
θ	Fluorescence orientation
λ	Optical wavelength
π	Pi
ρ	Density
Ω	Brillouin frequency shift

To the best family;
my father and mother,
my sisters and brothers,
and my beloved wife

Acknowledgements

Many people have contributed in various ways during my doctoral journey. I am thankful to all of them.

My sincere thanks to my supervisor, Dr. Anja Geitmann. Thanks for her insightful comments, encouragement and continuous support all these years. She has always been a role model for me, inspiring and motivating me in many aspects of academic life. It is fantastic to work in her lab. Thank you, Anja, very much!

I am grateful to Dr. Mario Cappadocia for his continuous advice and support during very critical times along the way. Thank you very much, Mario. Many thanks to Drs. Charles Anderson, Tomomi Tani and Giuliano Scarcelli who gave me opportunities to learn specialized methods and techniques and gave me full access to their laboratories and microscopes. Thank you!

I am thankful to many colleagues for their support. I thank Youssef Chebli for translating the abstract and providing me, throughout my doctoral study, with technical advice. I also thank Yuki Hamamura for her valuable advice in molecular biology techniques. Many thanks to my best colleagues; Gokcan Sahin, Hana Bertrand, Karuna Kapoor and Souad Mroue for their constant help in various ways. I am grateful to my colleagues and friends, Shafayet Zamil and Amir Bidhendi for their constant stimulated discussions, for answering my numerous questions regarding bioengineering and for the joyful moments in the lab. I also thank Amir for the special moments we shared together in the lab. I learned a lot from Amir regarding bioengineering and computer simulation. Thank you, Amir!

Last but not least, a very special thanks to my family. My parents who were always been there for me, supporting and encouraging me during my study abroad. My sisters and brothers who gave me continuous encouragements and supports, each in her/his way. I am thankful to my wife for her endless support and care throughout working on this thesis. I am grateful for her patience despite the two years that I had to spend away from her. Without their love and supports, this accomplishment could never be completed.

1 Introduction[1]

1.1 General introduction

Plant cells possess features that clearly distinguish them from animal cells. One of these features is the cell wall that was first described in the 17th century by Robert Hooke (Hooke, 1667). This extracellular matrix has been a subject of research interest in recent years for its environmental and industrial importance. It has been used for a variety of applications ranging from biomedical purposes to improve human health to the production of biofuel (Burton and Fincher, 2014; Loque et al., 2015; Pique et al., 2018). Our understanding of cell wall function for the plant, thus, is increasing. Besides its well-known function as structural support for the plant, it plays an important role during pathogen attack and acts as the first line of defense not only pasively but also actively. The cell wall releases oligosaccharide fragments, such as oligogalacturonides, to trigger the plant immune system upon exposure to stresses. Moreover, the cell wall has a crucial role during the growth and differentiation of cells by controlling the three-dimensional changes in cell shape that are important to generate a functional cell (Cosgrove, 2016; Chebli and Geitmann, 2017; Bacete et al., 2018; Engelsdorf et al., 2018).

Cellular growth in the plant results in an increase in the cell size and, typically, in an alteration in the cell shape. Unlike animal cells in which cytoskeletal forces play a direct role in cell shaping and growth, morphogenetic processes in plant cells are governed by the cell wall and turgor pressure inside the cell. Cytoskeletal control of cellular morphogenesis is exerted indirectly through the spatial and temporal regulation of cell wall assembly (Geitmann and Ortega, 2009). In plant cells, typically, two wall layers are distinguished — the primary and the secondary wall. The latter is deposited between the former and the plasma membrane. While this secondary wall in plant cells plays a crucial role for the eventual function of numerous cell types (*i.e.*, in tracheids, fibers, and sclereids), it is generally only deposited once cell growth has

---

[1] This section contains passages modified and updated references from my peer-reviewed article that has been published in 2015 (DOI:10.1016/j.pbi.2014.11.007); "Altartouri B, Geitmann A (2015) Understanding plant cell morphogenesis requires real-time monitoring of cell wall polymers. Curr Opin Plant Biol 23: 76-82"

ceased and it is, therefore, the primary wall that is the crucial determinant in cellular morphogenesis. Cellular growth implies the deformation and stretching of the existing primary wall accompanied by the assembly and insertion of new cell wall material. The process is driven by the turgor pressure that pushes onto and causes tensile stress in the wall. Only when and where the wall yields to this stress can cell growth occur (Schopfer, 2006; Boudaoud, 2010; Cosgrove, 2016). Unlike the flexible shapes of most animal cells, shape-forming processes in plant cells are generally irreversible. Understanding how the plant cell controls growth and shape formation through regulating the material properties of the cell wall is therefore fundamental for the investigation of plant development.

The understanding of the biomechanical aspects of plant cell differentiation has been inspired and guided by numerous conceptual and quantitative models (Thompson, 2005; Geitmann and Dyson, 2013; Bidhendi and Geitmann, 2018) that have spurred subsequent experimentation. Mechanical models, especially quantitative ones, must be informed by structural, geometrical and biochemical data. Given that cellular differentiation and growth are by definition dynamic processes with a temporal component, these data must ideally be acquired over a period of time. This requirement for real-time information on the spatial arrangement and the mechanical behavior of cell wall components at a subcellular level represents a crucial challenge for plant developmental studies. Conventional techniques used for mechanical studies, such as tensile tests, are largely limited to the tissue level and are highly invasive (Bidhendi and Geitmann, 2018). Even in the case of more sophisticated techniques, such as atomic force microscopy (AFM), sample preparation and mounting methods may prevent monitoring live changing in the mechanical behavior of the wall. Live labeling strategies of polysaccharides, in contrast to proteins, cannot be based on the expression of molecular chimeras comprising a fluorochrome as is accomplished in proteins through genetic recombination with green fluorescent protein or its derivatives.

1.2 Background and motivation

1.2.1 Primary cell wall components

The primary cell wall is a mixture of polysaccharides and structural proteins. The polysaccharides are mainly composed of cellulose (15 – 40 %), xyloglucan (20 – 30 %) and a heterogeneous matrix of pectins (30 – 50 %) (Burton et al., 2010; Cosgrove and Jarvis, 2012). During cellular growth, a new assembly of these polymers has to occur in order to regulate the mechanical behavior and form the appropriate thickness of the wall. This typically involves the insertion of new cell wall polymers, either by exocytosis or plasma membrane-located synthesis, and their insertion into the existing wall (Keegstra, 2010). Simultaneously, existing load-bearing bonds between cell wall polymers can be broken and new bonds can be formed. The breakage of load-bearing bonds and reconnection or relaxed bonds between polymers is a relaxation mechanism that allows the turgid cell to release the tensile stress in the cell wall. The chemical structure and the physiochemical properties of these polymers thus defines cell wall deformation and cell growth (Cosgrove, 2005; Peaucelle et al., 2012; Lampugnani et al., 2018).

Cellulose is composed of chains of unbranched β-glucose units held together by β-1,4-linkages. It is synthesized at the plasma membrane by cellulose synthase (CESA) complexes composed of three glycosyltransferases enzymes, mainly CESA1, CESA3, and CESA6 (Desprez et al., 2007). These synthesis proteins are assembled in the Golgi apparatus in an inactive form and then exocytosed as cellulose synthase complexes (CSCs) to the plasma membrane where they are activated. Both cortical microtubules and the actin cytoskeleton are involved in regulating the actions of CESAs (Sampathkumar et al., 2013). The actin cytoskeleton is associated with trafficking of small CESA compartments (Sampathkumar et al., 2013), whereas, cortical microtubules act as a landmark of CESA complex insertion in the plasma membrane and direct the trajectories of newly synthesized cellulose (Paredez et al., 2006; Crowell et al., 2009; Gutierrez et al., 2009). The deposition of cellulose is oriented as a result of the interaction between cortical microtubules and CESAs through cellulose synthases interacting (CSI1) protein (Li et al., 2012). Parallel arrangements of six glucose chains synthesized from each glycosyltransferase enzymes form cellulose microfibrils, 3-5 nm wide (Cosgrove, 2014).

Xyloglucan is another chain that is composed of β-1,4-glucan, however, it is branched and decorated with different mono- di- and tri-glycosyl side chains depending on plant species and tissue type (Scheller and Ulvskov, 2010). It is synthesized by glycosyltransferase in the Golgi apparatus. The variation in the length and branches of the xyloglucan suggest a different role of this polymer. For example, fucosylation of xyloglucan increases its capacity to bind with the excess aluminum cation (Wan et al., 2018). However, the main function of the xyloglucan during cell growth is to provide a spot where a loosening enzyme, expansin, can act (Wang et al., 2013; Park and Cosgrove, 2015).

Pectins are divided into three groups in the primary cell wall, homogalacturonan (HG), rhamnogalacturonan I (RGI) and rhamnogalacturonan II (RGII). Similar to the xyloglucan, pectins are synthesized by glycosyltransferase in the Golgi apparatus. All pectin types have a common 1,4-linked α-d-galacturonic acid backbone except for RGI which is a repetition of galacturonic acid and rhamnose (α-1,4-d-GalA-α-1,2-l-Rha). The three types of pectin are mostly cross-linked with HG being the most abundant. They are classified based on present/absent and the type of the side chain; HG is unbranched part of the galacturonic acid chain, RGI is decorated with arabinan and arabinogalactan side chains and RGII has long and diverse side chains (Mohnen, 2008; Sebastian et al., 2009; Harholt et al., 2010; Pabst et al., 2013). Both cortical microtubules and the actin cytoskeleton are reported to be involved in the deposition and/or modification of pectin in the cell wall (Kim and Brandizzi, 2014; Zhu et al., 2015). Galacturonic acid in the unbranched side can be modified by methyl esterification or *O*-acetylation and the degree of these modification defines the properties of the polysaccharide (Harholt et al., 2010; Palin and Geitmann, 2012).

The interaction between these wall polymers is determined by their physiochemical properties. Cellulose microfibrils exhibit hydrophilic and hydrophobic surfaces. The surface that exposes the axial CH is the hydrophobic surface while hydrophilic surfaces expose the equatorial OH of the glucose chain. The interaction of xyloglucan and pectin with cellulose is influenced by this physical property of the microfibril. Xyloglucan binds with the hydrophobic surface while pectin binds with the hydrophilic surface. The site of the cellulose-xyloglucan interaction is important to reduce wall tension where the loosening enzymes can act to drive the expansion (Park and Cosgrove, 2012, 2012; Wang et al., 2012; Park and Cosgrove, 2015).

1.2.2 Cell wall mechanics and architecture control expansive growth in plant cells

One of the principal motivations for investigating the spatial arrangement and the biomechanical contribution of cell wall components is the fact that they exert spatial and temporal control on cellular morphogenesis and hence plant developmental processes. To be specific, expansive growth of walled cells under the effect of turgor pressure is influenced by at least two parameters characterizing the mechanical behavior of the wall (Sanati Nezhad and Geitmann, 2014). The first parameter is the degree of uniformity of the wall properties, which determines whether the cellular surface expands entirely or only partially, that is, some cellular regions expand rapidly while others resist the turgor pressure. The partial expansion is a result of a non-uniform distribution of particular polymer types and/or of their cross-links. This, in turn, is regulated by the local addition of stiffer or softer cell wall material or by the local secretion of enzymes that break existing linkages between polymers or promote their formation. The spatial map of cell wall stiffness is a crucial determinant for the expansion pattern of individual plant cells (Zerzour et al., 2009; Chebli et al., 2012) and consequently that of complex tissues (Peaucelle et al., 2011; Peaucelle et al., 2015; Bou Daher et al., 2018). The second parameter is the degree of anisotropy in the cell wall rigidity at any given location. The rigidity of a unit section of the cell wall can differ depending on the direction in which the stress is applied. Such anisotropic expansion behavior is created by a non-random orientation of components with high tensile strength, primarily cellulose microfibrils (Baskin, 2005). Anisotropic cell wall expansion can, for example, lead to the longitudinal cell shapes observed in the root and shoot. How the cell wall responds to applied tensile stress is therefore fundamental for the final shape of the cell.

Although the chemical structure of individual cell wall polymers is well known, their biomechanical contributions toward cell growth patterning are still largely elusive. Numerous experimental techniques have been used to quantify the mechanical behavior of the cell wall (Geitmann, 2006). These include methods based on indenting the wall using a calibrated probe at the cellular and subcellular level (Milani et al., 2013; Routier-Kierzkowska and Smith, 2013) as well as the application of tensile stress using an extensometer (Wei et al., 2006; Park and Cosgrove, 2012). Because these techniques are difficult to apply to a part of a living cell, numerous studies used *in silico* simulations to predict the influence of a subcellular mechanical variation on cell expansion (Sampathkumar et al., 2014; Yanagisawa et al., 2015; Bidhendi and Geitmann, 2018; Sapala et al., 2018; Yi et al., 2018). However, *in silico* simulation has to be coupled with the spatial and temporal distribution of the wall polymers during cellular expansion and micromechanical measurements to be validated (Geitmann, 2010). One of the promising techniques that non-invasively characterize the mechanical properties of biological material with subcellular resolution is Brillouin microscopy. This optical method is able to infer the mechanical properties (i.e. longitudinal modulus) from the Brillouin frequency shift. Interaction of an incident visible light with thermally induced acoustic waves within the material or tissue generates the Brillouin frequency shift. These acoustic waves are a result of the fluctuation of the molecules within the tissues. Therefore, an increase in the frequency shift indicates a higher longitudinal modulus (Scarcelli and Yun, 2007; Scarcelli et al., 2015). This method has been successfully used to characterize the mechanical properties of biological materials such as cornea (Scarcelli et al., 2011; Yun and Chernyak, 2018) and recently was used to characterize plant cell wall biomechanics (Elsayad et al., 2016).

An example where the *in silico* simulation was validated by mechanical measurements is the pollen tube, a cell type with highly polarized growth behavior. A cellular outgrowth into a single direction is promoted by highly localized insertion of soft cell wall material — mostly methyl-esterified pectins — into the cell wall. A spatially controlled and enzymatically regulated wall stiffening process ensures that this soft spot remains spatially confined and yields a growing protuberance with a cylindrical shape (Hepler et al., 2013). Micromechanical measurement of the pollen tube confirmed that the cell wall in the growing region of the cell is softer and *in silico* simulation of the growth process predicted a precisely defined spatial gradient of cell wall rigidity that was shown to be reflected in the spatial distribution of cell wall components (Zerzour et al., 2009; Fayant et al., 2010). Immunocytochemical labeling revealed that enzymatic conversion of methyl-esterified into the de-esterified form of HG pectin at the maturing region of the apical cell wall must be the crucial process to stiffen the growing tube and determining its diameter (Chebli et al., 2012).

The methylation status of HG is important during cellular development (Knox et al., 1990). Depending on the de-esterification pattern, HG may rigidify the wall and thus restrict its expansion or soften the wall and allow further expansion. A random demethyl-esterification of HG may attract polygalacturonase enzyme that degrades the HG polymer resulting in wall loosening. On the other hand, non-random (blockwise) demethyl-esterification allows calcium-mediated gelation and thus restricts expansion (Hocq et al., 2017). For example, an increase in the degree of pectin demethyl-esterification induces organ growth and reduces the stiffness of the shoot apical meristem in *Arabidopsis thaliana* (Peaucelle et al., 2011), whereas an increase in the demethyl-esterified pectin in the dark-grown hypocotyl of *Arabidopsis* restricts its elongation (Derbyshire et al., 2007). Thus, investigating the role of HG pectin in cell expansion requires micromechanical measurements.

Although the mechanical role of the principal pectin polymers in cell expansion has been studied in several biological systems (Palin and Geitmann, 2012; Peaucelle et al., 2012; Bidhendi and Geitmann, 2016), the role of other pectin polymers, in particular, RGI requires further investigation. It has been shown that the spatial distribution of RGI changes during cell expansion (Anderson et al., 2012). The arabinan side-chains of RGI show heterogeneity in their structure, linear and branched, between tissues and even within a single cell as revealed by specific immunocytochemical labeling (Verhertbruggen et al., 2009). Interestingly, these side-chains have been shown to influence the flexibility of the cell wall (Caffall and Mohnen, 2009; Verhertbruggen et al., 2013). An increase in stiffness of the inflorescence stem was shown in mutant *Arabidopsis* displaying a reduction in the linear arabinan structure (Verhertbruggen et al., 2013). It would be interesting to assess whether the heterogeneity and/or the spatial distribution of RGI polymers have a mechanical impact on the expanding cells in this system.

The mechanical strength of cellulose microfibrils arises from the numerous inter- and intramolecular hydrogen bonds linking the polymers. Highly bonded cellulose microfibrils give cellulose a high degree of structural order, or crystallinity, and thus a high tensile strength along their long axes (Eichhorn and Young, 2001; Somerville, 2006). In the primary cell wall, cellulose microfibrils are a mixture of crystalline and non-crystalline (amorphous) portions. The crystalline portion corresponds to about one third of the amorphous portion (Fujita et al., 2011; Cosgrove, 2014). Despite having a lower abundance, it is believed that crystallinity plays an important role during cell expansion. Decreased cellulose crystallinity is associated with an increase in the growth rate of the cell (Fujita et al. 2011). Inversely, increased crystallinity is known to control cellular expansion when microfibrils are arranged in a non-random manner in the plane of the wall (Baskin, 2005). In the elongated cylindrical epidermal cells, for example, cellulose microfibrils in the inner tangential wall display an orientation transverse to the axial expansion direction of the cell (Crowell et al., 2011). As cell growth slows and stops, the orientation of microfibrils becomes more isotropic (Anderson et al., 2010; Crowell et al., 2011). The authors suggest that this spatial configuration of microfibrils in the inner tangential wall of the epidermis is causal for the anisotropic growth behavior in the fast-growing regions of the hypocotyl and root tissues analyzed in these studies. While many observations suggest a correlation between microfibril orientation and shape formation, the mediation of the effect may be complicated since certain mutants with swollen (isotropically growing) cells do not show the predicted random orientation of microfibrils but an ordered configuration instead (Sugimoto et al., 2003; Fujita et al., 2011). The cellulose-mediated anisotropic expansion of the elongated cylindrical epidermal cells of the hypocotyl is preceeded by changes in the de-esterification status of the side wall of the cells. Such changes can initiate the anisotropic expansion while cellulose microfibrils play a role after this step (Peaucelle et al., 2015; Bou Daher et al., 2018). Whether an increase or decrease in the demethyl-esterified pectin at the longitudinally oriented side walls of the cylindrical cell initiates the anisotropic expansion needs further investigation since two recent studies showed opposite results using the same genetic mutation (Peaucelle et al., 2015; Bou Daher et al., 2018).

The orientation of cellulose microfibrils and the spatial distribution of homogalacturonan pectin have been investigated in geometrically simple cells such as the cylindrical cells of the shoot and root (Anderson et al., 2010; Crowell et al., 2011; Peaucelle et al., 2015; Bou Daher et al., 2018), in cells with more complex geometry the spatial arrangement of these wall polymers during cell formation is still to be examined. Leaf epidermal cells exhibit complex geometries by forming interdigitated jigsaw-puzzle shapes, with necks in one cell being tightly connected to the lobes in the neighboring cell. The cells typically have a tabular geometry consisting of two periclinal walls parallel to the surface of the leaf and an anticlinal wall lining the circumference perpendicular to it. During cellular morphogenesis, the surface of the projection of the cell viewed from above, and hence the two periclinal walls, increases in size and shape complexity, whereas the anticlinal wall expands in a highly anisotropic manner. Its horizontal dimension increases with the expanding cell, whereas its vertical dimension remains nearly unaltered. Because of this unique geometry, pavement cells have been the subject of multiple studies to answer why and how it takes such a shape (Panteris and Galatis, 2005; Jacques et al., 2014; Sapala et al., 2018; Bidhendi et al., 2019). It has been hypothesized that the interlocking shape of pavement cells provides more surface for cell to cell adhesion and thus increases the mechanical strength of the epidermal layer to protect the underlying mesophyll layers (Glover, 2000). This has been only conceptually supported by the peeling test of different pattern of fabricated material (Lee et al., 2000). A recent study suggested that epidermal pavement cells employ lobeyness to minimize the largest area of the periclinal wall that is generated through expansion of polyhedral shapes and thus reduces the stress on the periclinal wall (Sapala et al., 2018). Although the relationship between cell area and lobeyness was drawn from several species, further studies on additional taxa would be helpful to corroborate this concept. To answer how pavement cells develop interlocking shapes, several studies have focused on the dynamics of cytoskeletal elements. At the junction of the external periclinal wall with the anticlinal wall, microtubule arrays are associated with neck regions while actin filaments are associated with lobe regions of pavement cell (Fu et al., 2002; Fu et al., 2005; Panteris and Galatis, 2005; Sampathkumar et al., 2014; Armour et al., 2015). Although the deposition of the wall polymers is guided by the cytoskeletal filaments which has prompted many researchers to use the latter as proxy for the former, the spatial correlation of microfibrils with morphogenetic events remains to be investigated. One of the main reasons for this lack of knowledge is the limited availability of wall polymer probes that allow live-cell observation at high spatial resolution. Immunogold labeling of cell wall epitopes shows that softer wall polymers, such as galactans and arabinans, are spatially confined to the neck region of the curved anticlinal wall (Majda et al., 2017). Based on this evidence, Majda et al. (2017) suggested that these polymers soften the prospective neck region to allow undulation formation at the anticlinal wall under the effect of a tensile force. Although this is supported further by mechanical measurement of the anticlinal wall and *in silico* simulation (Majda et al., 2017; Majda et al. 2019), this mechanism is based only on anticlinal wall mechanics and does not seem to function when the periclinal wall is considered. *In silico* simulations by Bidhendi and Geitmann (2019) show that the anticlinal wall may involve in coordinating changes between the outer and inner periclinal walls, however it is not involved in the initiation process of the undulation, whereas the periclinal wall is of crucial importance for the initiation of the process (Panteris and Galatis, 2005; Bidhendi and Geitmann, 2019). At the periclinal wall, the enrichment of cellulose microfibrils occurs in the regions where cell expansion is restricted. This has been shown only in the fully developed cells (Panteris and Galatis, 2005; Sampathkumar et al., 2014; Bidhendi et al., 2019). However, how cellulose and other wall polymers regulate the initiation and further development of necks and lobes in the pavement cells has not been addressed.

The regulatory mechanism leading to shape formation in pavement cells is likely based on a feedback mechanism in which shape, or rather, shape-induced stress influences the deposition of microfibrils (Sampathkumar et al., 2014). This is consistent with the effect of externally applied stress on the reorientation of microtubules and, by consequence, on cellulose microfibril deposition (Hamant et al., 2008). Whether the spatial arrangement of non-cellulosic cell wall polymers, in particular, pectins, is subject to such stress-induced mechanisms in pavement cells is largely unknown. It is reasonable to assume that this is the case since cylindrical epidermal cells exhibit this order of events and since it has been shown that the secretory machinery delivering new pectin material can be relocated actively by the cell in order to achieve a change in its growth pattern as a response to an external trigger (Bou Daher and Geitmann, 2011). Real-time imaging of dynamic changes in the spatial configuration of cell wall polymers will provide important information for our understanding of these feedback mechanisms.

1.2.3 Real-time imaging of cell wall polysaccharides

Visualizing the dynamics of cell wall polymers requires microscopic techniques combined with appropriate characteristic features or labeling tags that allow the identification of the observed components (Gonneau et al., 2012). Insight into cellulose architecture can be obtained by both transmission electron and scanning electron microscopy. The latter requires the use of a field emission gun for sufficient resolution and enables the observation of microfibrils on the cell wall surface facing the plasma membrane or on the outer surface of epidermal or single cells (Himmelspach et al., 2003; Aouar et al., 2010). No particular labeling is used in these studies since microfibrils have a uniquely fibrous morphology and dimension. Observation of microfibrils through the thickness of the wall is only possible if inner wall layers are made accessible to the electron beam, for example by producing grazing sections or by cryo-fracturing the wall (Fujita and Wasteneys, 2014). The same limitation applies to imaging cellulose microfibrils with atomic force microscopy which only allows the accessible polymers to be visualized (Kafle et al., 2014; Zhang et al., 2014). A view through the central layers of the cell wall can be obtained in transmission electron microscopy. Particularly valuable for this technique are highly oblique or grazing sections that have enabled observation of the varying orientations of cellulose microfibrils through the thickness of the wall (Emons and van Maaren, 1987). While the electron microscope techniques provide exquisite detail in terms of spatial resolution, they require the fixation of the specimen, and hence do not allow following any dynamic changes over time. Imaging of fresh and never dried samples is possible using atomic force microscopy, but attaining the most important microfibrils, those facing the plasma membrane, still requires sacrificing the specimen and hence making developmental time course imaging impossible.

Various types of optical microscopy have been used to visualize the cell wall including darkfield and differential interference contrast. However, the most prominent type of analysis of the biochemical composition of the cell wall has been based on the use of fluorescent probes and antibodies with affinity to particular cell wall components. Antibodies can be produced to recognize a distinct epitope present in glycans and thus represent a specific labeling method that can even distinguish between different chemical configurations of individual polymers

(Verhertbruggen et al., 2009; Pattathil et al., 2010; Chebli et al., 2012). As is the case for electron-based techniques, the cells generally need to be fixed for the labeling to be administered and, therefore, provide only a snapshot of the glycans at a particular time-point and fail to depict a full picture of their dynamics during the morphogenetic process. Moreover, antibody-based labeling methods are associated with long sample preparation, fixation artifacts and limited tissue permeability which often pose a challenge.

An alternative to antibodies are fluorescent probes, small molecules that have a more or less specific affinity with a particular cell wall polymer. As with all labeling methods, the use of fluorescent probes and interpretation of the data must be performed with caution and caveats. Specificity for a particular polymer is often tacitly assumed or erroneously interpreted but does not necessarily correspond to reality. For example, calcofluor white has been widely used to visualize cellulose microfibrils, but it is also known to bind other wall polymers with an affinity that is as high as that for cellulose microfibrils (Anderson et al., 2010). Knowing the mechanism and the target of fluorescent probe binding is therefore essential (Anderson et al., 2010; Rounds et al., 2011).

Generally, the experimental protocols necessary for fluorescent probe labeling are simpler than those for antibodies. Some require fixation, but others can be applied to living tissues or cell cultures (Anderson et al., 2010; Rounds et al., 2011). When this is done and cells or tissues are observed over time it must be ensured that the presence of the dye is neither toxic nor influences cell growth or division. Yariv reagent, for example, a dye that labels arabinogalactan proteins present in the cell wall, interferes with cell growth (Mollet et al., 2002). Propidium iodide (PI) is commonly used to label cell walls in growing plant tissues (Tian et al., 2006; Peaucelle et al., 2011). Used at moderate concentrations, this dye does not seem to interfere with growth processes even if these are fast and/or oscillatory such as in root hairs and pollen tubes. In these cells, propidium iodide has been used to label demethyl-esterified HG (Rounds et al., 2011). Demethyl-esterification of galacturonyl residues leaves a negatively charged carboxyl group which enables gel formation through binding to positively charged calcium ions. The authors showed that the positive charges of propidium iodide bind the negative galacturonyl residues competing with calcium ions but without cross-linking HG chains (Fig. 1.1). Using this dye allowed the authors to characterize the oscillatory pattern of demethyl esterification, which was found to be in agreement with the oscillatory secretion in the pollen tube apex of pectin methylesterase — an enzyme that converts methyl-esterified HG into the demethyl-esterified form (McKenna et al., 2009).

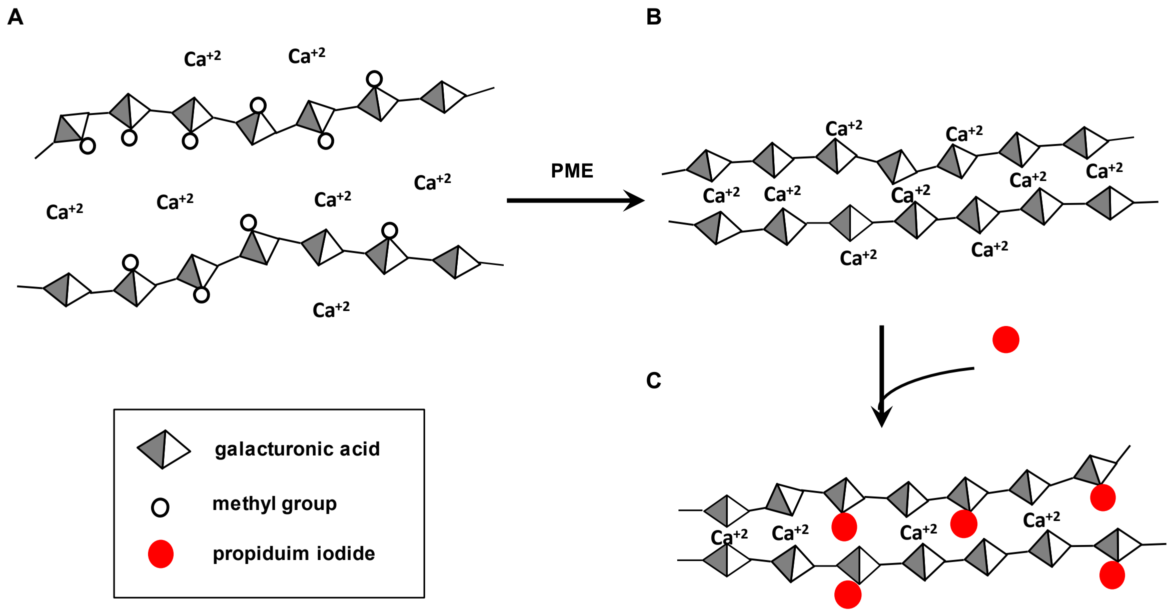

Figure 1.1: Interaction of methyl and de-methyl esterified HG with calcium ions and propidium iodide.

A, Methyl groups on the galacturonyl residues render the molecule neutral and the pectin material relatively liquid. **B,** Removing the methyl groups by the action of pectin methyl esterase allows the negatively charged carboxyl groups on the galacturonyl residues to bind calcium ions thus forming a gel of the HG chains. **C,** A model of the positively charged propidium iodide molecules competing with calcium ions to bind the negatively charged residues of de-methyl esterified HG polymers as proposed by (Rounds et al., 2011).

A recently explored dye is Pontamine Fast Scarlet 4B (S4B), a dye that stains cellulose with high specificity (Anderson et al., 2010) and the fluorescence of which is polarization-dependent. It has successfully been used for *in vivo* time-lapse imaging of cellulose microfibrils in the expanding cell walls of growing root epidermal cells. The observations revealed the reorientation of cellulose microfibrils during cellular elongation. Cellulose microfibrils were found to be deposited perpendicular to the axial expansion and then to reorient to the longitudinal direction confirming the previously postulated notion that older microfibrils reorient passively as a result of the turgor-driven expansion of the cell wall material (Preston, 1982; Anderson et al., 2010).

A promising recent development in terms of polysaccharide visualization is based on metabolic labeling using bio-orthogonal chemistry. This strategy relies on chemical reactions that occur inside of living systems without interfering with native biochemical processes. Bio-orthogonal labeling has proven valuable in visualizing glycans in living animal (Prescher and Bertozzi, 2005; Laughlin and Bertozzi, 2009) and bacterial (Siegrist et al., 2013) cells and has recently been introduced to plant cell walls (Anderson et al., 2012; Bukowski et al., 2014; Dumont et al., 2016). In general, the reaction used for glycan labeling consists of two steps. The first step is the administration of a modified analog monosaccharide with an azide or alkyne group (chemical reporters) that is incorporated into the specific polysaccharide through its synthetic pathway. The second step is a reaction between the chemical reporter and the imaging probe (Fig. 1.2). The azide and alkyne groups have special characteristics that allow them to be used in living systems. They are small functional groups, biological inert, metabolically stable and able to react with other bio-orthogonal functional groups at physiological pH (Laughlin and Bertozzi, 2009). Taking advantage of this well established principle, several analogs were successfully synthesized and used to study the spatial and temporal localization of wall polymers including RGI, RGII and lignin (Anderson et al., 2012; Bukowski et al., 2014; Pandey et al., 2015; Dumont et al., 2016; Pandey et al., 2016). For instance, Anderson et al. (2012) used Fucose-Alkyne (FucAl) to visualize RGI in the root elongation zone of *Arabidopsis* seedlings. Interestingly, chasing FucAl during cell elongation enabled the authors to observe changes in the spatial distribution of RGI. The distribution of RGI after 12 h of chasing starts to assume a pattern identical to cellulose. This is consistent with the fact that RGI side-chains, similar to xyloglucans, have been found to form non-covalent linkages with cellulose microfibrils (Zykwinska et al., 2007). The ability of RGI polymers to binds with cellulose and the observation that they change their spatial distribution raises questions about their role in determining cell wall mechanics during cell expansion. Clearly, plant cells are able to take up an unnatural sugar and incorporate it in a desired donor polymer that can be used to perform a reaction with an exogenous probe without affecting the physiological behavior of *Arabidopsis* seedlings (Anderson et al., 2012; Pandey et al., 2015; Dumont et al., 2016). Introducing different types of synthesized sugar analogs will, therefore, be highly useful to visualize cell wall polymers in live plant cells (Wang et al., 2016).

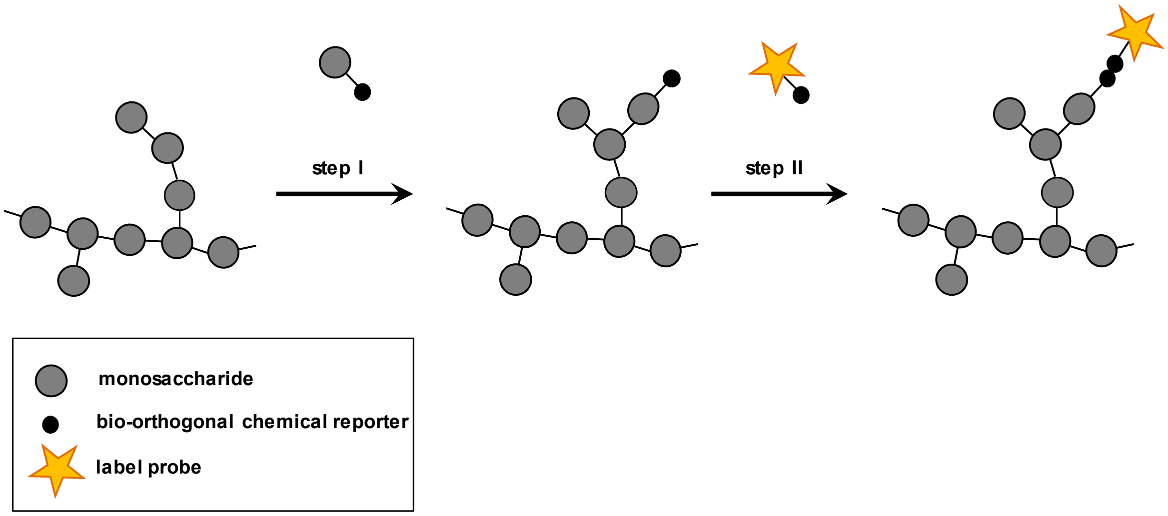

Figure 1.2: Strategy of the metabolic bio-orthogonal labeling used for glycans.

Step I, an exogenous monosaccharide linked with the chemical reporter (Azide or Alkyne groups) incorporates into the target glycans through their synthesis pathway. Step II, a bio-orthogonal chemical reaction between the different chemical reporters of the monosaccharide and the exogenously administered labeling probe.

1.3 Research question and objectives

The research project described in this thesis aimed at investigated the role of the cell wall in the complex cell shaping occurring in epidermal cells of Arabidopsis. The main question addressed in this research is how cellulose microfibrils and homogalacturonan pectin contribute to cell shape during cell growth and expansion. The contribution of these polymers during cell expansion was identified based on their expression, spatial distribution, and mechanical impact. These aspects were approached by using genetics and novel cell mechanical and imaging methods. Two types of cell shapes were examined in this study: epidermal pavement cells of cotyledons (jigsaw-puzzle shape) and epidermal cells of the hypocotyls (cylindrical shape) of *Arabidopsis thaliana*.

The research objectives can be articulated as follows:

1. To characterize the spatiotemporal events of lobe formation in the epidermal pavement cells of *Arabidopsis* cotyledons.

   This objective can be broken down to the following sub-objectives:

   - To investigate cellulose orientation at the two sides of the undulation using polarized fluorescence microscopy.
   - To evaluate the spatial distribution of demethyl-esterified pectin during lobe formation.
   - To assess the cell wall rigidity at a subcellular level during lobe formation using Brillouin scattering microscopy.

2. To study the impact of the cellulose crystallinity and esterification status of homogalacturonan pectin in the elongation pattern of dark-grown hypocotyl of *Arabidopsis*.

   This objective can be broken down to the following sub-objectives:

   - To identify a correlation between these wall components and the anisotropic expansion of the cell.
   - To identify a correlation between these wall polymers, wall expansion and the mechanical properties of the wall.

1.4 Thesis structure

This thesis is organized as follows, chapter 2 addresses the first objective of this study. The second objective is addressed in Chapter 3. Finally, Chapter 4 summarizes the research outcomes and discusses future perspectives.

2 Cellular morphogenesis in lobed pavement cells involves a multi-step mechanism governed by pectin chemistry and cellulose crystallinity

The impact of cellulose microfibrils and the homogalacturonan pectin and their spatial distribution during the morphological process of pavement cells are presented in this chapter. This chapter presents a manuscript that has been accepted in Plant Physiology journal (in press). The authors of this manuscript are:

Bara Altartouri[a], Amir J Bidhendi[a], Tomomi Tani[b], Johnny Suzuki[c], Christina Conrad[c], Youssef Chebli[d], Na Liu[e], Chithra Karunakaran[e], Giuliano Scarcelli[c], and Anja Geitmann[a,d]

[a] Département de sciences biologiques, Université de Montréal, Montréal, QC H1X2B2, Canada
[b] Eugene Bell Center for Regenerative Biology and Tissue Engineering, Marine Biological Laboratory, Woods Hole, MA 02542, USA
[c] Fischell Department of Engineering, University of Maryland, College Park, MD 20742, USA
[d] Department of Plant Science, McGill University, Sainte-Anne-de-Bellevue, QC H9X3V9, Canada
[e] Canadian Light Source, 44 Innovation Boulevard Saskatoon, SK S7N 2V3, Canada

I am responsible for all experimental design, data acquisition, processing and analysis, and discussing the results. I am also responsible for writing the manuscript. Amir J Bidhendi participated in the experimental design of visualizing pectin by the COS^{488} probe and immuno labelling. I worked together with Tomomi Tani to visualize cellulose microfibrils by polarized fluorescence microscopy. I worked together with Johnny Suzuki and Christina Conrad to acquire the Brillouin data and I analyzed the data. Christina Concard and Giuliano Scarcelli participated in the writing the Brillouin part of the manuscript. Giuliano Scarcelli and Anja Geitmann supervised this part of the work. For the FTIR experiment, I designed the experiment and prepared the samples, Na Liu acquired the data, Youssef Chebli analyzed the data. Chithra Karunakaran and Anja Geitmann supervised this part of the work. Anja Geitmann supervised all the research process and the experimental design and helped in the preparation of the manuscript with edits and advice on content.

Keywords: Cellulose microfibril, pectin, pectin methylesterase, cell expansion, cell wall mechanics, cortical microtubule, polarized fluorescence microscopy, Brillouin microscopy

2.1 Abstract

The generation of simple plant cell morphologies such as cylindrical shoot cells is known to be determined by the extensibility pattern of the primary cell wall thought to be largely dominated by cellulose microfibrils. The mechanism leading to more complex shapes such as the interdigitated patterns in the epidermis of eudicotyledon leaves, on the other hand, is much less well understood. Details about the manner in which cell wall polymers at the periclinal wall regulate the morphogenetic process in epidermal pavement cells and mechanistic information about the initial steps leading to the characteristic undulations in the cell borders are elusive. We used genetics and novel cell mechanical and imaging methods to study the impact of the spatio-temporal dynamics of cellulose and homogalacturonan pectin during lobe formation in the epidermal pavement cells of *Arabidopsis thaliana* cotyledons. We show that non-uniform distribution of cellulose microfibrils and demethylated pectin correlate with spatial differences in cell wall stiffness but may intervene at different developmental stages. Our data suggest that lobe initiation involves a modulation of cell wall stiffness through local enrichment in demethylated pectin, whereas subsequent increase in lobe amplitude is mediated by the stress-induced deposition of aligned cellulose microfibrils. Our results reveal a key role of non-cellulosic polymers in the biomechanical regulation of cell morphogenesis.

2.2 Introduction

Cellular differentiation in plants involves dramatic alterations in cell shape leading to highly specialized cell types such as trichomes, fibers or guard cells. Cell growth and shaping involve a turgor driven deformation of the cell wall and is assumed to be governed by at least two crucial parameters related to the material properties of the primary cell wall (Sanati Nezhad and Geitmann, 2014; Altartouri and Geitmann, 2015). The first parameter is the degree of spatial uniformity of the wall stiffness that is controlled by the extensibility of the cell wall material and the dimensions (thickness) of the wall. The second parameter is the degree of anisotropy of the wall material properties that control the directionality of the expansion. These parameters can be modulated by the local addition of stiffer or softer cell wall material (Zerzour et al., 2009;

Chebli et al., 2012; Szymanski, 2014; Peaucelle et al., 2015; Yanagisawa et al., 2018) and/or by the local secretion of enzymes or wall modulating agents that break existing linkages between polymers (Cosgrove, 1998, 2016). Cellular processes such as exocytosis, polymer synthesis and wall assembly thus determine the expansion pattern of individual plant cells and consequently the morphogenesis of complex tissues (Szymanski and Cosgrove, 2009; Szymanski and Staiger, 2018). Cellulose microfibrils play a major role in determining the expansion directionality of the plant cell wall. When these polymers are arranged in non-random manner in the plane of the cell wall, they restrict expansion in parallel but allow expansion in the direction perpendicular to their net orientation (Diddens et al., 2008; Anderson et al., 2010). This is related to the strong tensile strength these polymers exhibit along their long axis which increases with increased degree of structural order of the microfibrils (i.e. crystallinity) (Eichhorn and Young, 2001; Kerstens et al., 2001; Thomas et al., 2013; Cosgrove, 2014). Mutation or drug-induced reduction in cellulose crystallinity cause radial swelling of cylindrical cells (Aouar et al., 2010; Fujita et al., 2013). While the concepts of cell shaping are increasingly well characterized in geometrically simple shapes such as the cylindrical cells of the shoot and root, the mechanism of complex shape formation remains poorly understood.

The epidermal layer of eudicotyledon leaves exhibits several types of such complex cell geometries that are generated from a simple shape: trichomes, guard cells and pavement cells. Depending on the species, pavement cells can be brick-shaped or they form an interdigitated jigsaw-puzzle pattern, with indents (necks) and protrusions (lobes) of neighboring cells being tightly connected to each other and forming undulations. This phenomenon is widely distributed, although with substantial variations (Vofely et al., 2019). The lobed pattern has been proposed to reduce the stress in the periclinal walls of larger epidermal cells (Sapala et al., 2018). Our understanding of the shape formation and developmental processes at cellular level is largely based on inferences made from the observations of cytoskeletal dynamics ((Fu et al., 2005; Panteris and Galatis, 2005; Kotzer and Wasteneys, 2006; Zhang et al., 2011; Szymanski, 2014; Armour et al., 2015; Eng and Sampathkumar, 2018). Because in living cells, cytoskeletal proteins are easier to observe than cell wall polysaccharides, and because the deposition of the latter is often regulated by the former, cytoskeletal dynamics are frequently used as a proxy for developmental changes occurring in the cell wall. Notably, it has been hypothesized that the spatial arrangement of cortical microtubules alters cell wall stiffness through deposition of cellulose microfibrils to restrict the expansion of the cell at neck regions of pavement cells, while lobe regions continue to expand during cell growth (Panteris and Galatis, 2005; Szymanski, 2014; Armour et al., 2015). Although there is evidence for the correlation between the alignment of cortical microtubules with the expansion direction in which cellulose microfibrils are deposited, for instance, in the cylindrical epidermal cells of plant roots (Anderson et al., 2010), there is no clear evidence for such correlation in the lobe formation of pavement cells. Cellulose microfibrils are arranged in a fan-like configuration in the neck regions of the periclinal wall in pavement cells of several eudicotyledons (Panteris et al., 1994; Panteris and Galatis, 2005), but so far this has only been shown for mature cells of *Arabidopsis thaliana* that possess fully developed lobes (Sampathkumar et al., 2014), whereas information on early developmental stages is elusive. This arrangement of cellulose microfibrils at the neck region is thought to allow the wall to expand perpendicularly to the direction of the microfibrils and, thus, initiate waviness (Panteris and Galatis, 2005; Szymanski, 2014). At the lobe region of the periclinal wall, two configurations of cellulose microfibrils are suggested. First, a net-like configuration that allows isotropic expansion of the lobe region (Armour et al., 2015). Second, an arrangement parallel to the tangent of the lobe tip that allows anisotropic expansion toward the long axis of the lobe (Szymanski, 2014; Elsner et al., 2018). A recent study showed that treatment with cellulase alters *Arabidopsis thaliana* pavement cell shape, but does not prevent the generation of waviness (Higaki et al., 2017). The exact role of cellulose microfibrils at various stages of pavement cell development has not been examined. In silico simulation predicts an important role for the stress-induced deposition of cellulose microfibrils during the development of wavy cell shapes (Sampathkumar et al., 2014; Armour et al., 2015; Bidhendi et al., 2019). However, whether cellulose actually contributes to or is essential for the early stages of lobe formation is unknown.

The differentiation of pavement cells is proposed to be governed by spatial variations in the expansion rate of the periclinal wall between the opposing sides of the undulation (Armour et al., 2015; Bidhendi et al., 2019). Such spatial variation suggests the presence of subcellular variation in cell wall stiffness. This is supported conceptually by recent studies on shoot epidermal cells and pollen tubes (Zerzour et al., 2009; Chebli et al., 2012; Peaucelle et al., 2015).

It has been shown that differences in the stiffness of the anticlinal walls of the shoot epidermal cells are required to allow promote cell elongation. The spatial difference in cell wall stiffness in these cells was shown to be regulated by the activity of pectin methyl esterase (PME), an enzyme that promotes gelation of the homogalacturonan (HG) pectin since it removes methyl-groups rendering the polymers negatively charged (Peaucelle et al., 2015; Bou Daher et al., 2018). Similarly, in the rapidly growing pollen tube, the local stiffness of the cell wall varies with softer material characterizing the growing region of the cell (Zerzour et al., 2009). This subcellular variation in cell wall stiffness reflects the spatial distribution of cell wall polymers (Fayant et al., 2010; Chebli et al., 2012). For pavement cells, various scenarios have been proposed to explain the formation of undulations, including a cellulose-based stiffening in the periclinal wall (Panteris and Galatis, 2005; Bidhendi et al., 2019) or the presence of mechanochemical heterogeneities in the adjacent anticlinal walls (Majda et al., 2017). The latter scenario is based on the presence of softer wall components, such as galactans and arabinans, at the neck region of the anticlinal wall, but the role of cellulose microfibrils was not examined in this study. The external periclinal wall of pavement cells is suggested to have a major role during lobe formation (Panteris and Galatis, 2005; Sampathkumar et al., 2014; Bidhendi et al., 2019). Panteris et al. (1994) show that in Cyperus papyrus pavement cells, cortical microtubules bundle at the periclinal wall, and that these bundles are not extended into the depth of the anticlinal wall. The depth of the anticlinal wall does not exhibit waviness in this species pointing at an important role for cellulose microfibrils for the propagation of the morphogenetic process in 3D space. Here, we investigate the role of cellulose microfibrils and demethyl-esterified pectin during the morphogenetic process of lobe development, focusing on the initiation of the process at the periclinal wall. We used live cell imaging to study the arrangement of the cellulose microfibrils at high spatial resolution and the distribution of the demethyl-esterified pectin in the pavement cells of the cotyledon of *Arabidopsis thaliana* wildtype and *anisotropy1* (*any1*) mutant which is characterized by a significant reduction in cellulose crystallinity without reduction in overall cellulose content (Fujita et al., 2013). Moreover, we used Brillouin microscopy to infer the spatial stiffness map of the periclinal wall in living pavement cells. Finally, we tested the influence of the PME and pectin methyl esterase inhibitor (PMEI) on the shape of pavement cells. The results of this study provide crucial evidence for the initiation mechanism of cell shaping and the roles of cellulose microfibrils and demethyl-esterified pectin during the developmental process of the undulations of pavement cells.

2.3 Results

2.3.1 Lobe can be initiated at a substantially reduced degree of cellulose crystallinity

To understand the role of crystalline cellulose during lobe development, we investigated pavement cell shape in cotyledons of wildtype *Arabidopsis thaliana* and of the *any1* mutant (Fig. 2.1A; Supplemental Fig. 2.1). The total content of cellulose in the cell wall of this mutant was reported to be unaltered, while the relative amount of crystalline cellulose is reduced substantially. Moreover, epidermal pavement cells in this mutant have a swelling phenotype (Fujita et al., 2013). As this is thought to be caused by the reduced degree of cellulose crystallinity and hence reduced stiffness of the cell wall, we wanted to quantitatively assess the effect of this modulation in the wall molecular configuration on the lobed shape of the pavement cells. To this end, we measured the circularity ratio and the number of lobes per cell. Circularity is used here to evaluate shape changes of pavement cells during their developmental stages (Fig. 2.1A) as was done in previous works (Zhang et al., 2011; Armour et al., 2015). The circularity ratio is a number between 1 and 0 with 1 indicating a perfect circle. In *any1* the mean cell circularity ratio was significantly higher compared to the wildtype pavement cells at 2, 3 and 4 days after germination ($P < 0.001$) (Fig. 2.1B). While in the wildtype the circularity ratio decreased over the course of two days, the value remained almost unaltered in the mutant over the same period of time. The decrease in circularity ratio does not discriminate between a potential increase in depth of existing undulations and the increase in the number of undulations. To untangle the two, we quantified the number of lobes and determined the aspect ratio of individual lobes. Only true lobes were taken into account and newly dividing cells were excluded as detailed in the Supplementary Material (Supplementary Note 2.1; Supplemental Fig. 2.2, Fig. 2.1G). We applied a convex hull-fitting algorithm on the shape of pavement cell and calculated the period of lobes by dividing the square root of the convex hull area by the lobe number. This ratio was chosen in order to exclude any differences between wildtype and *any1* mutant that are generated from the difference in the overall growth of the cell (Figs. 2.1C, D and G; Supplemental Fig. 2.2B). The mean lobe period in the *any1* mutant was significantly different from the wildtype over the four-day observation period (Fig. 2.1E). The aspect ratio of lobes was determined by calculating the depth over the width of a given lobe (Figs. 2.1F,G). This parameter showed that lobes in *any1* were shallow compared to the wildtype pavement cells when observed at 4 days after germination. Importantly, this difference was generated by cellular development over the preceding 3 days since at 1 day after germination the lobe aspect ratio was identical in *any1* and the wildtype (Fig. 2.1F). While the lobe period was increased compared to the wildtype, *any1* mutant cells were able to initiate lobes during pavement cell differentiation. Clearly, the amplitude of these lobes is not further increased during subsequent developmental steps. This suggests that high crystallinity is more critical for lobe expansion than for lobe initiation.

2.3.2 Well-aligned cellulose microfibrils are required for lobe expansion more than lobe initiation

It has been shown in several plant species that the alignment of cellulose microfibrils at the neck regions of mature pavement cells is fan-like, radiating from the tip of the neck (Panteris et al., 1994; Panteris and Galatis, 2005). Such orientation was shown for the neck region of young and fully formed pavement cell undulations in *Arabidopsis* cotyledons (Sampathkumar et al., 2014; Bidhendi et al., 2019). It is suggested that the perpendicular alignment restricts the expansion of the neck region, but there is no direct evidence for this correlation in the early stages of lobe formation. To examine whether lobe initiation and subsequent expansion in the wildtype and *any1* pavement cells is correlated with the reported alignment of the cellulose microfibrils, we investigated the degree of the alignment (the anisotropy degree, hereafter) of cellulose at both neck and lobe regions with high spatial resolution in living cells. We stained cellulose microfibrils with the fluorescent dye Pontamine Fast Scarlet 4B (S4B) that specifically binds to cellulose (Anderson et al., 2010) and used polarized fluorescence microscopy (Mehta et al., 2016; Swaminathan et al., 2017) to examine the anisotropy degree of cellulose microfibrils (Thomas et al., 2017). The anisotropy of S4B's fluorescence polarization reflects the anisotropy degree of cellulose in the periclinal wall of the pavement cells at pixel-by-pixel resolution. The reliability of this technique for determining the molecular alignment of cellulose in plant cell walls was confirmed by testing it on plant cells whose cellulose microfibril orientation is well established (Supplemental Figs. 2.3A,B). These calibration tests suggest that the ensemble fluorescence polarization orientation of S4B bound to cellulose is parallel to the orientation of cellulose microfibrils.

At later developmental stages, cellulose microfibrils on the neck side of an undulation had a preferential orientation perpendicular or fan-like to the tangent at the tip of the undulation (Fig. 2.2A; Supplemental Figs. 2.3C,D). This is in agreement with the previously suggested (Sampathkumar et al., 2014) and reported orientation of the microfibrils in developed pavement cells (Panteris et al., 1994; Panteris and Galatis, 2005; Bidhendi et al., 2019). More importantly, we were able to quantify the anisotropy degree of cellulose microfibrils at subcellular resolution in the early stages (1 day after germination) of pavement cell development (Fig. 2.2B) by using the anisotropy values of fluorescence polarization. The difference in average anisotropy degree between neck and the corresponding lobe regions was statistically significant in the wildtype pavement cells ($P < 0.0001$, *paired t*-test) but not in *any1* cells ($P > 0.05$, *paired t*-test) (Fig. 2.2C). Given that *any1* mutants did have lobes, albeit shallow, these results suggest that highly aligned cellulose microfibrils at the indentation side of the undulation are involved in augmenting lobe amplitude during differentiation, but that the initiation of lobes does not seem to require a differential in the alignment of cellulose microfibrils.

The net-like configuration of cellulose microfibrils at the lobe region of the early stages in the wildtype (Fig. 2.2C) suggests isotropic expansion of that region. We measured the expansion rate of the lobe depth and width of each lobe during the first 24 hours of its development to assess the direction of the expansion. The difference in the expansion rate between lobe width and lobe depth was close to zero (Fig. 2.2D). These results suggest that during the early stages, the periclinal wall in the lobe undergoes isotropic expansion, in agreement with observations of fiducial marker displacement reported by Armour et al. (2015).

2.3.3 Subcellular variation in periclinal wall stiffening is associated with lobe initiation and subsequent expansion

Sampathkumar et al. (2014) showed that the outer face of the periclinal wall in fully lobed cells exhibits fibrillar structures, presumably cellulose microfibrils, that were speculated to increase the local stiffness when probed with the orthogonally acting atomic force microscope. Our data indicate that enrichment of microfibrils at the neck side appears already early during development and that pectin may potentially cause an even earlier stiffness inhomogeneity, but the visual evidence of these polysaccharides is no proof for actual mechanical differentials. We therefore wanted to assess the stiffness of the cell wall material at undulations in the *any1* mutant and compare it to the wildtype.

To map stiffness through the thickness of the wall rather than just at the outer face, we used Brillouin microscopy, an all-optical method that can be used to non-invasively characterize mechanical properties of biological materials (Scarcelli et al., 2015). It has, for example, been used successfully to characterize corneal biomechanics (Yun and Chernyak, 2018). The phenomenon of Brillouin scattering arises due to the interaction of an incident visible light (photons) with inherent sound waves (phonons) within the material. Generally, instrumentation comprises a Brillouin spectrometer and a standard inverted confocal microscope. As with any confocal modality, 3D mapping can be performed with high spatial resolution, dictated by the objective lens. The distance between the peaks of the Brillouin spectrum and the incident laser is the Brillouin Frequency Shift (BFS) and lies in the gigahertz (GHz) frequency range. Inputting index of refraction and density values of the measured material, the BFS can be converted to longitudinal modulus, the ratio of axial stress to axial strain in a constrained setting (Supplemental Eq. 2.1). When comparing longitudinal modulus measured by the high-frequency Brillouin scattering with the traditional low-frequency Young's modulus, it is critical to note that these measures have large expected differences in magnitudes (gigapascals vs. kilopascals). The high-frequency used in the Brillouin measurement gives only little time to the polymers to relax and contribute to the softness of the material. Therefore, a modulus in GHz can be obtained. In recent years, several works have examined the correlation between the BFS and longitudinal modulus with the Young's modulus and found that these two moduli trend in the same direction, with the underlying biophysical properties, and thus, within a given material, BFS could be used to extract relative information about modulus changes (Scarcelli and Yun, 2007; Scarcelli et al., 2011; Scarcelli et al., 2015). The suitability of Brillouin technique for determining the stiffness of plant cell walls was addressed earlier by Elsayad et al. (2016). Further details of this technique are provided in the supplementary material (Supplementary Notes 2.2 and 2.3; Supplemental Fig. 2.4).

Here, we observed that cellulose crystallinity contributes to the stiffness of the pavement cells. Firstly, we found that, when measured in the central regions of the periclinal walls, the Brillouin shift in the *any1* mutant displayed a significantly decrease compared to the wildtype ($P < 0.001$, *student's t*-test) (Figs. 2.3A,B). The reduction in the stiffness of the cell wall in the *any1* mutant was corroborated by performing a mechanical tensile test on the dark-grown hypocotyl of the wildtype and the *any1* mutant. This mechanical tensile test revealed that the apparent Young's modulus of the dark-grown hypocotyl was reduced significantly in the *any1* mutant compared to the wildtype (Supplemental Fig. 2.5). These results show that general reduction in cellulose crystallinity in the *any1* mutant causes reduction in wall stiffness and that the Brillouin technique is a reliable tool to non-invasively detect such change in the wall stiffness.

Secondly, the Brillouin shift revealed differences in stiffness at the lobe and the corresponding neck regions at an early stage of development (1 day after germination). Consistent with our previous findings, for both the neck and lobe regions, the BFS and longitudinal modulus of the wildtype was significantly higher than that in the *any1* mutant ($P < 0.001$, *student's t*-test) (Figs. 2.3C,D). For the wildtype, the neck had a significantly higher BFS and longitudinal modulus compared to the lobe region ($P < 0.0001$, *paired t*-test) (Figs. 2.3C,D). This corroborates and expands on the information previously obtained on fully developed pavement cells using atomic force microscopy (Sampathkumar et al., 2014). Interestingly, a significant, albeit less substantially elevated BFS and longitudinal modulus of the neck was found for the *any 1* mutant pavement cells ($P < 0.001$, *paired t*-test) (Figs. 2.3C,D). These results suggest that the high degree of cellulose crystallinity translates to a stronger stiffness differential between neck and lobe in the wildtype which we hypothesize to promote the amplitude development of the lobe at later stages.

2.3.4 Cortical microtubules are not affected by the reduction of cellulose crystallinity and their localization evolves during lobe formation

The hypothesized role of cellulose microfibrils during lobe formation arises from the observation of cortical microtubules at the periclinal wall of the pavement cells (Szymanski, 2014; Bidhendi et al., 2019). The initiation of lobes involves the reconfiguration of a typically net-like configuration of the cortical microtubules to one that is aligned perpendicular or fan-like to the tangent of the neck region in the periclinal wall (Fu et al., 2005; Zhang et al., 2011; Armour et al., 2015; Higaki et al., 2017). We crossed *any1* with GFP:TUB6 in order to examine whether the cortical microtubule organization is correlated with the initiation of the undulation in the pavement cells of *any1* mutant. The mean circularity and lobe number per cell of GFP:TUB6/*any1* mutant pavement cells was found to be similar to that of *any1* (Supplemental Figs. S6A,B). The organization of microtubules in the epidermal cells of the leaf, hypocotyl and roots is not affected in the *any1* mutant (Fujita et al., 2013). Moreover, the perpendicular bundles of cortical microtubules at the neck regions of the periclinal wall were not affected in *any1* pavement cells compared to the wildtype (Supplemental Fig. 2.6C). We monitored the cortical microtubules and the changes in the cell wall of pavement cells in the wildtype and *any1* mutant over 18 hours with 6-hour time-lapse intervals (Figs. 2.4A-F). We quantitatively determined the alignment (i. e. degree of anisotropy) of cortical microtubules in the periclinal wall (Figs. 2.4C,F). The anisotropy degree at the prospective neck region at time 0 was higher in both wildtype and *any1* mutant compared to the prospective lobe regions of the same undulation at the periclinal wall (Fig. 2.4G). In order to confirm the tight relation of cortical microtubule bundles with undulation formation, both GFP:TUB6 and GFP:TUB6/*any1* were grown in the presence of oryzalin, a herbicide that leads to the depolymerization of cortical microtubules (Supplemental Fig. 2.6C) (Morejohn et al., 1987). In both lines, the mean lobe number was significantly reduced compared to the same developmental stage of the control pavement cells (Supplemental Figs. 2.6D,E). This indicates that cortical microtubules in both wildtype and *any1* mutant cells play a significant role in lobe development.

2.3.5 Demethyl-esterified pectin may play a role during lobe initiation and is localized at the neck regions

To answer how undulations are initiated at reduced cellulose crystallinity in the pavement cells of *any1*, we investigated the role of HG pectin in cell shaping. HGs are secreted in highly methylated form and can be modified *in muro* through the activity of PMEs. The degree of pectin esterification is known to control the cellular expansion in several biological systems (Chebli et al., 2012; Palin and Geitmann, 2012; Peaucelle et al., 2015; Bou Daher et al., 2018). Demethyl-esterified pectin is known to gelate by binding to calcium ions which increases the stiffness of this polymer material *in vitro* (Ngouemazong et al., 2012) and *in muro* (Bou Daher et al., 2018). This polymer is also reported to be associated with neck region of *Arabidopsis* pavement cells (Bidhendi et al., 2019). We investigated the shape of pavement cells in several PME and PMEI mutants (Supplemental Fig. 2.7A) selected based on their expression levels in the cotyledon (Winter et al., 2007). Although several of the mutants (*pme3, pme44 and pmei41*) showed a significantly elevated number of lobes per cell (Supplemental Fig. 2.7A), the effect seemed to result from an increased overall growth rate of the cell rather than an increase in lobe initiation events since lobe period remained unaltered (Supplemental Fig. 2.7B).

Next, we wanted to test whether pectin plays a more prominent role when the crystallinity of cellulose is reduced. To examine this hypothesis, we grew the mutants in the presence of CGA 325’615 (CGA). This herbicide reduces cellulose crystallinity at picomolar concentrations and increases the relative abundance of amorphous cellulose (Peng et al., 2001). It has no significant effect on overall cellulose content (Supplemental Fig. S8A). Moreover, it has no effect on the cytoskeleton and Golgi bodies (Crowell et al., 2009). Cellulose crystallinity was reduced significantly in the *Arabidopsis* cotyledons of the wildtype seedlings when they were grown in the presence of CGA compared to the control (Bidhendi et al., 2019). Moreover, the degree of cellulose crystallinity in the CGA treated seedlings is comparable to that of the *any1* mutant (Supplemental Fig. 2.8B). The mean circularity and lobe number of pavement cells of the CGA treated seedlings were similar to those of the *any1* mutant (Figs. 2.1A-E; Supplemental Figs. 2.8C-G). The orientation of cortical microtubules in the pavement cells was not altered under the effect of CGA compared to the wildtype (Supplemental Fig. 2.8H). In the presence of the drug, pavement cells of *pmei37* showed a significantly reduced lobe period compared to the wildtype (Fig. 2.5A; Supplemental Figs. 2.7B,C). However, when the drug was present, neither in the wildtype nor in the mutant did the aspect ratio of the lobes reach that of the respective untreated control (Fig. 2.5B). In the *pmei37* mutant treated with CGA, the percentage of esterification was significantly reduced compared to wildtype in presence of CGA (Supplemental Figs. 2.9A,B).

Next, we investigated the localization of demethyl-esterified pectin in the *any1* mutant and compared it to the wildtype pavement cells. The localization of this polymer is connected with the neck side of the undulation in several angiosperms and in *Arabidopsis* pavement cells (Sotiriou et al., 2018; Bidhendi et al., 2019). In the wildtype and *any1* pavement cells, demethyl-esterified pectin was enriched at the neck side as revealed by the antibody label (Supplemental Fig. S10). In order to quantitatively compare the abundance of demethyl-esterified pectin at lobe and neck regions, we used COS^{488}, a molecular probe specific for this configuration of pectin (Mravec et al., 2014), and compared the fluorescence intensity at the neck and the corresponding lobe of the same undulation. This difference was high in the early developmental stages in *any1* mutant cells, similar to wildtype cells (Figs. 2.5C,D). Furthermore, we monitored the spatial pattern of demethyl-esterified pectin over time in order to correlate its dynamics with that of cortical microtubules and changes in cell shape. Monitoring was done over 18 hours with 6-hour time-lapse intervals. We used propidium iodide (PI), a dye that is commonly used to stain cell walls and can be used to evaluate the esterification status of cell walls (Rounds et al., 2011). PI staining showed similar spatial pattern at the periclinal wall compared to the COS^{488} probe (Fig. 2.6A). Quantitative determination of the changes in the abundance of demethyl-esterified pectin and the enrichment of cortical microtubules at prospective neck regions at the periclinal wall revealed that the former preceded the latter during the onset of curvature formation (Figs. 2.6B-H; Supplemental Fig. 2.11). These results support the notion that demethyl-esterified pectin in the wall of pavement cell plays a major role in lobe initiation.

2.4 Discussion

In this study, we asked how the cell wall regulates the developmental process of the undulation formation in the epidermal pavement cells of *Arabidopsis thaliana*. Our results are consistent with the concept of a two-step mechanism consisting of distinct and differently regulated processes: initiation and subsequent expansion (Fig. 2.7). The initiation step involves an increase in the stiffness of the periclinal wall at the prospective neck side of the undulation through a local accumulation of demethyl-esterified pectin. The subsequent expansion is controlled by the gradual enrichment in cellulose microfibrils aligned perpendicularly to the tangent of the neck side of the undulation.

Cellulose microfibrils had been suggested to control both the initiation and the subsequent expansion of the undulation because of their strong tensile strength along their long axis (Kerstens et al., 2001; Suslov and Verbelen, 2006). We show that cellulose crystallinity is correlated with the stiffness of the cell wall, with higher stiffness characterizing higher crystallinity ratio. The increase in the circularity of the *any1* mutant pavement cells was associated with a reduction in cellulose crystallinity and, thus, a swelling phenotype (Fujita et al., 2013). However, pavement cells of *any1* were still able to restrict the expansion at specific spatial regions and initiate undulations. We hypothesized that this might result from a subcellular difference in the arrangement of cellulose microfibrils at the neck/lobe regions as shown previously (Panteris et al., 1994; Panteris and Galatis, 2005; Sampathkumar et al., 2014). At early stages of lobe formation in the wildtype, the anisotropy degree of cellulose microfibrils increased at the neck side compared to the lobe side of an undulation. This accumulation of cellulose was associated with an increase in lobe depth during subsequent cell development. We posit that this correlation is causal since in the *any1* mutant the difference in anisotropy degree at the two opposing sides of the undulation was smaller than in the wildtype and, consistent with that, lobe depth did not augment significantly during subsequent cell development. Given that *any1* mutants are capable of initiating lobes and this initiation was not associated with a marked difference in the cellulose anisotropy between opposing sides of the undulation, we conclude that high crystallinity and the perpendicular orientation of cellulose microfibrils are strongly correlated with depth augmentation of the lobe, more than with the initiation process of the lobe. We speculate that the increased lobe period in the *any1* pavement cells might be a consequence of the inability of the cells to stabilize initiated lobes. Many barely initiated lobes may be straightened during further growth of the cell unless robustly stabilized by cellulose enrichment in the neck.

The orientation of cellulose microfibrils at the neck and the lobe sides in the wildtype suggests that these periclinal wall regions resist turgor driven expansion differently. Upon lobe initiation, expansion at the lobe region may be isotropic, whereas the neck region undergoes less, but anisotropic expansion parallels to the tangent of the lobe as suggested by the displacement of fiducial markers (Armour et al., 2015). During lobe expansion, the periclinal wall in the lobe seems to undergo anisotropic expansion as reported by Elsner et al. (2018), likely promoted by the transverse alignment of cellulose microfibrils at the base of the lobe perpendicular to its long axis (Sampathkumar et al., 2014; Bidhendi et al., 2019).

The spatial stiffness map of the periclinal wall reflects the mechanism that leads to the formation of the undulation in the wildtype and *any1* mutant. The stiffness at the cell periphery of the periclinal wall, at the early developmental stages, varies with the material at the neck being stiffer compared to the lobe regions in the wildtype. This explains the low expansion rate at the prospective neck side of the undulation compared to the lobe side as suggested by (Armour et al., 2015) and (Bidhendi et al., 2019). The higher stiffness value at the neck region of the wildtype is in agreement with the reported stiffness of the neck regions at the late stages of pavement cell development that is obtained by atomic force microscopy (Sampathkumar et al., 2014). Also, it is correlated with the presence of both higher degree of cellulose crystallinity and high anisotropy ratio of cellulose in the wildtype. The presence of cortical microtubules and cellulose microfibrils extending from the periclinal wall into the depth of the anticlinal wall (Zhang et al., 2011; Belteton et al., 2017; Bidhendi et al., 2019) suggests that cell wall stiffness on the neck side extend into the depth of the anticlinal wall, although we did not show this here. While this would be consistent with most studies, it is difficult to reconcile with the concept by Majda et al. (2017) who proposed that the neck side of the anticlinal wall is softer than the lobe side. A possible explanation could be that atomic force microscopy is more sensitive to other wall polymers when probing parallel to the direction of the cellulose microfibrils, but additional research is clearly warranted.

Remarkably, in the *any1* mutant pavement cells, a small difference in the stiffness between the two opposing sides of the undulation was detected in the initial developmental stages. This raises the question of the biochemical underpinning of this differential. We speculated that the relative quantities of amorphous cellulose at the opposing sides of the bend are different, or that other strengthening polymers at the neck regions are involved. We suspected demethyl-esterified pectin to play a role as suggested by (Bidhendi et al., 2019) and consistent with this, the *pmei37* mutant showed a reduction in lobe period under conditions of pharmacologically reduced cellulose crystallinity. Moreover, demethyl-esterified pectin as evidenced with COS^{488} was enriched at the neck regions compared to the lobe regions in both wildtype and *any1* mutant cells. The association of this polymer with the stiffness of the wall and, therefore, the restriction of the expansion can be due to the ability of this polymer to form gelation in the presence of calcium ions (Ngouemazong et al., 2012). The spatially confined enrichment of this polymer is associated with stiffer regions in the pollen tube (Zerzour et al., 2009; Chebli et al., 2012). Overexpression of *PME5* increases the stiffness of the wall in the etiolated hypocotyl (Bou Daher et al., 2018). Moreover, increasing the demethyl esterification of the wall can restrict the growth and the expansion of the wall as shown in the pollen tube and elongated shoot cells (Bosch et al., 2005; Derbyshire et al., 2007). Therefore, demethyl-esterified pectin may play a significant role by increasing the stiffness of the periclinal wall at prospective neck regions leading to the initiation of an undulation. This process also changes the stress distribution at the periclinal wall that plays an important role during lobe formation since it regulates, in a feedback mechanism, the arrangement of cortical microtubules and the auxin-Rho-GTPase signaling pathway, that has been proposed to control pavement cell development (Fu et al., 2005; Hamant et al., 2008; Jacques et al., 2013; Sampathkumar et al., 2014; Bidhendi et al., 2019).

The suggested role of cellulose microfibrils in the initiation of the undulation was based on the observation that cortical microtubules are oriented perpendicular or fan-like to the tangent of the neck region at the periclinal wall of mature pavement cells (Zhang et al., 2011; Sampathkumar et al., 2014). Armour et al. (2015) showed that cortical microtubules at the periclinal wall are present at the prospective neck regions in wildtype pavement cells (Armour et al., 2015). We show that this microtubule configuration applies equally to the *any1* mutant pavement cells in which cellulose crystallinity is known to be reduced and the alignment of cellulose is more random. Additionally, when wildtype and *any1* mutant seedlings were grown in the presence of oryzalin, pavement cells failed to expand lobes. Based on these results we propose that the early accumulation of cortical microtubules may be the result of a locally confined increase in stress caused by the presence of demethyl-esterified pectin and a resulting stiffening of the wall and lobe initiation. Cellulose microfibrils are important primarily for the second developmental step, the augmentation of lobe depth.

The advantage of the two-step mechanism over concepts that suggest the initiation of undulations based on cellulose microfibrils is that it can explain how pavement cells, during the developmental process, are able to initiate new neck regions not only in straight walls but also within existing lobes where the orientation of cellulose is more random. This is supported by the observation of mutation in PMEI that allowed initiation of new lobes when cellulose crystallinity was reduced. The demethylation process of the esterified pectin at the existing lobe region can increase the stiffness and therefore the stress that subsequently results in increased local bundling of cortical microtubules (Hamant et al., 2008; Jacques et al., 2013).

2.5 Acknowledgements

We thank Drs. Geoffrey Wasteneys and Miki Fujita (University of British Columbia) for providing the *any1* mutant seeds. We thank Dr. Pierre R.L. Dutilleul (McGill University) for advice on statistical methods. We thank Dr. Shalin B. Mehta for providing a mathematical code for fluorescence anisotropy analysis. COS^{488} probe was generously provided by Dr. William George Tycho Willats (University of Copenhagen). This project was supported by grants from the Natural Sciences and Engineering Research Council of Canada (NSERC) and the Canada Research Chair Program. Part of the research described in this paper was performed at the Canadian Light Source, which is supported by the Canada Foundation for Innovation, Natural Sciences and Engineering Research Council of Canada, the University of Saskatchewan, the Government of Saskatchewan, Western Economic Diversification Canada, the National Research Council Canada, and the Canadian Institutes of Health Research.

2.6 Materials and Methods

2.6.1 Plant materials

Arabidopsis (*Arabidopsis thaliana*) wildtype (ecotype Columbia-0), GFP-TUB6 (accession number; CS6550), *pme1* (AT1G53840; SALK_120021), *pme3* (AT3G14310; CS2103492), *pme15* (AT2G36710; CS859505), *pme25* (AT3G10720; SALK_021426C), *pme44* (AT4G33220; CS837906), *pmei37* (AT3G47670; SALK_068827C) and *pmei41* (AT3G62820; SALK_027168C) were obtained from Arabidopsis Biological Resource Center. *any1* mutant seeds were obtained from the lab of Dr. Geoffrey Wasteneys (University of British Columbia, Canada) (Fujita et al., 2013). *any1*/GFP-TUB6 was obtained by crossing plants expressing p35S::GFP-TUB6 with *any1* plants, and F2 progeny expressing GFP-TUB6/*any1* were used for visualizing microtubules. T-DNA insertions were confirmed by PCR from genomic DNA with the following LP/RP primer pairs; 5'-TCAGTTTATTGGTGGTGGAGG-3' and 5'-TCGATCAGATCTCCACAAACC-3' for *pme1*, 5'-AATTGGTTGAATGACGAAACG-3' and 5'-TACGTACCTGCCCCTTCAAC-3' for *pme3*, 5'-TGGATTCTATGGGGCTCAAG-3' and 5'-TTTATGGGAGAGCCATGGAC-3' for *pme15*, 5'-GCGTAATCGACAAAGTGACG-3' and 5'-ACTCAGCTCCGATAACTCGC-3' for *pme25*, 5'-AGCAACCAGTTTCACAAACG-3' and 5'-CTTTTGTACCAGCGAAACCC-3' for *pme44*, 5'-TGTGGTCTACCGTTTTCACG-3' and 5'-TCACTATGCTCCGTGACTCG-3' for *pmei37* and 5'-ACCAACGAATTGTTATCGGC-3' and 5'-TACTCGTTAGGTGGCATGGG-3' for *pmei41*.

Seeds were sterilized and kept at 4°C in the dark for 2 days. Seeds were grown in plates containing 0.5x Murashige and Skoog salt (MS; Fisher Scientific - cat# ICN2623220), 1% (w/v) sucrose and 0.8% (w/v) plant agar (Sigma-Aldrich – cat# A1296). The germination condition was 22°C under 8/16-h dark/light cycle.

The abaxial side of the cotyledon was used in this study. Images were taken from the mid-section of the cotyledon (Supplemental Fig.1). For image acquisition, samples were mounted between slide and cover slip for imaging. For time-lapse imaging, samples were placed immediately back to the *in vitro* growth chamber following each image acquisition.

2.6.2 Labeling methods

For cellulose labeling, the seed coat was removed 18 – 22 hours after germination to allow the penetration of the dye into the cotyledon of the wildtype and the *any1* mutant cells. The living seedlings were placed in 1.5 mL microcentrifuge tubes containing 0.02% (w/v) S4B (Sigma-Aldrich, cat# 212490) in liquid 0.5x MS medium and 1% sucrose for 3 hours at dark condition; then samples were washed three times with liquid 0.5x MS medium before observation. The cuticle layer of the cotyledons after 3 days of germination prevented the S4B dye from accessing the periclinal wall of pavement cells. Therefore, to allow observing cellulose microfibrils at this stage, the cuticle layer was removed or damaged by gently brushing the surface of the cotyledon with a paint brush prior applying the dye.

To label demethyl-esterified pectin, we used both a molecular probe (COS^{488}) and immunolabeling (monoclonal antibody LM19) on 1 day old seedlings of wildtype and *any1*. For COS^{488} label, living seedlings were placed in 1 µl/ml of the dye for 20 minutes and washed several times before observation in distilled water. For immunolabeling, seedlings were fixed with freshly prepared 3.5% formaldehyde in phosphate buffered saline (PBS; 135 mM NaCl, 6.5 mM Na2HPO4, 2.7 mM KCl, 1.5 mM KH2PO4, pH 7.3) and 1% Triton for 2.5 hours followed by three washes with PBS buffer. Next, seedlings were washed three times with 2.5% (w/v) bovine serum albumin (BSA) in PBS buffer. The first antibody (LM19; rat IgM – PalntProbes) was diluted (1:50) in the BSA-BPS buffer and 1%Triton. Seedlings were incubated in the first antibody for 2.5 hours. For controls, either the primary or the secondary antibody were excluded. Seedlings were washed three times with the BSA-BPS buffer after applying the first and the second antibody. The secondary antibody (Alexa Fluor 594 anti-mouse IgG - PalntProbes) was diluted 1:100 in the BSA-BPS buffer and 1%Triton. Seedlings were incubated in the secondary antibody for 2.5 hours.

For cell shape metrics analysis and time-lapse imaging, cell walls were labelled with 0.01 mg/ml propidium iodide (PI; Sigma-Aldrich, cat# P4170) for 20 min, followed by three washes with distilled water before observation. For time-lapse imaging, labelling was applied at each time point before the observation.

2.6.3 Drug treatments

Oryzalin (Riedel-de-Haën, cat# 36182) was used to depolymerize the cortical microtubules. The final working concentration was 10 µM (stock concentration was 10 mM dissolved in DMSO (Sigma-Aldrich, cat# D8418)). The same volume of DMSO (v/v) was used for the control experiment. Seedlings were grown in a solidified 0.5x MS medium in the presence of the drug. CGA (CGA 325'615, 1-cyclohexyl-5-(2,3,4,5,6-pentafluorophenoxy)-1λ4,2,4,6-thiatriazin-3-amine; (Syngenta - Basel, Switzerland)) was used to reduce cellulose crystallinity. The final working concentration was 0.9 nM (prepared from a 10 µM stock solution dissolved in DMSO). The same volume of DMSO (v/v) was used for the control experiment.

2.6.4 Measurement of cellulose and pectin contents

Arabidopsis seedlings (4 days after germination) were fixed in 100% methanol for 4 hours. Methanol was substituted with 100% ethanol and samples were critical point dried using a Leica EM CPD300. The epidermal surface composition was analyzed using FTIR Attenuated Total Reflection (ATR) at the mid-infrared beamline at the Canadian Light Source synchrotron (Lahlali et al., 2014). The globar source was employed as the infrared source. This ATR method used a germanium crystal (angle of incidence of 45°) attached to an Agilent Cary 600 Series FTIR spectrometer. Each infrared spectrum was recorded in the mid-infrared range of 4000 – 800 cm^{-1} wavenumbers at a spectral resolution of 4 cm^{-1}.

The data were analyzed with Orange 3.14. The data were corrected by performing a baseline correction (Rubber band) and by subtracting the background. The data were then normalized using the vector normalization algorithm and a Gaussian smoothing of 7 points was applied. The corrected data were transferred into the second derivative form by using the Savitzky–Golay algorithm. The estimation of components was determined by integrating the area between the baseline and specific bands, for cellulose (1170-1140 cm^{-1}), total pectin (1270-1215 cm^{-1}) and esterified pectin (1763 – 1723 cm^{-1}).

2.6.5 Measurement of cellulose crystallinity

X-Ray Diffractometer (Bruker D8 Discovery) was used to detect the amount of crystalline cellulose in the cotyledons of *Arabidopsis*. A Cu-source generated X-rays at 40 kV and 40 mA. The diffraction intensity was collected at the range of 4^{o} – 60^{o} with 0.005^{o} steps. The intensity data from 5^{o} – 40^{o} in the 2-theta angle range were used in the analysis. Cotyledons were critical point dried and flattened before the measurement. The amount of crystalline cellulose was measured using curve-fitting method assessed by the DIFFRAC.EVA (Bruker AXS GmbH) software.

2.6.6 Tensile testing of hypocotyls

Dark-grown *Arabidopsis* hypocotyls (5 days after germination) of wildtype and *any1* mutant were plasmolyzed with 0.8 M mannitol (Sigma-Aldrich, cat# M9647) for 20 minutes. The mid-region of the etiolated hypocotyl was mounted on a custom-built tensile device between two gripping ends that were 4 mm separated from each other by a linear motorized stage (Thorlabs). The sample was kept moisturized by adding a drop of the mannitol solution. The force was measured by a micro load cell sensor attached to one of the gripping ends. The sensor used in this experiment was designed for forces up to 5 gf (0.049 N) allowing reliable measurement of forces as small as 10 μgf (0.098 μN). The sensor was calibrated against a series of known weights each time that the device was reconfigured. The displacement of the grips was measured with micrometer resolution by a linear variable displacement transducer (LVDT). The forces generated by sample stretch were collected at the PC and registered using a custom Python code. These force-displacement data were used to generate the stress-strain curves. The custom-built tensile device was used under a Zeiss Discovery V8 stereomicroscope, 0.63x and 8x zoom, to allow measuring the diameter of each sample to calculate the area of the hypocotyl cross section. The apparent Young's modulus was calculated from the slope in the elastic range of the stress-strain curve. The density of the cell wall material per cross section in wildtype and mutant was not significantly different ($P > 0.05$) allowing direct comparison of the calculated apparent Young's moduli. The density was measured from 5 different patches of dry etiolated hypocotyls. Sections of identical length were cut from hypocotyls of wildtype and *any1* mutant. The diameter of the hypocotyls was measured under a Zeiss Discovery V8 stereomicroscope, 0.63x and 8x zoom. 4 – 5 pools of hypocotyls were prepared; each pool contained 40 – 50 hypocotyls. Each pool of hypocotyls was air dried at room temperature for two days. Then, the weight of each pool was recorded using a 0.1 mg microbalance. The density was calculated as dried mass divided by the volume of the hydrated hypocotyl. The average densities were 0.035 g/cm3 ± 0.003 (SE) and 0.034 g/cm3 ± 0.004 (SE) of wildtype and *any1* mutant, respectively.

2.6.7 Microscopy and image acquisition

Three types of microscopy were used in this study. Confocal laser scanning microscopy (CLSM), polarized fluorescence microscopy (LC-POLScope; laboratory of Dr. Tomomi Tani, Marine Biological Laboratory) and Brillouin microscopy (laboratory of Dr. Giuliano Scarcelli, University of Maryland).

For CLSM a Zeiss LSM 510 LSM 5LIVE/Axiovert 200M system was used. The 5LIVE/Axiovert 200M system was used for shape metrics analysis and time-lapse of cortical microtubules. The 532-nm laser was used with an emission filter 590-625 nm to visualize the cell wall (labelled with PI). The 488-nm laser was used with emission filter 500-530 nm to visualize GFP-TUB6. The time-lapse images were acquired every 6 hours. 63x oil-immersion objective lens (NA = 1.4) was used for time-lapse of microtubules and 20x objective lens (NA = 0.8) was used for the shape metrics measurement.

The Instantaneous FluoPolScope (Mehta et al., 2016; Swaminathan et al., 2017) was used in this study to address the anisotropy of cellulose at subcellular regions (i.e. neck and lobe). The 561-nm laser (Coherent OBIS, 20mW) was used for the total internal reflection illumination through an oil-immersion objective lens (Nikon TIRF 60x, NA = 1.49) to image cellulose labelled with S4B. The side length of a single pixel of the images captured with a camera (Andor iXon+ EMCCD camera) corresponds to 0.12 µm at the sample stage. A quadrant imaging system as described in (Mehta et al., 2016) was used for instantaneous analysis of fluorescence emission of cellulose-bound S4B along four polarization orientations at 45° increments. Back-ground corrected polarization-resolved fluorescence intensities (I0, I45, I90, I135) were used to compute polarized fluorescence orientation (θ) and the anisotropy of fluorescence polarization (*p*) per pixel as follows:

$$\theta = \tan^{-1}\frac{\mathrm{I0}-\mathrm{I90}}{\mathrm{I45}-\mathrm{I135}} \qquad \text{(Eq. 2.1)}$$

$$p = \frac{\sqrt{(I0-I90)^2+(I45-I135)^2}}{0.5\times(I0+I45+I90+I135)} \qquad \text{(Eq. 2.2)}$$

Brillouin microscopy was used to assess the stiffness of the periclinal wall of pavement cells. The detailed setup of the Brillouin microscopy can be found in our previous publications (Scarcelli and Yun, 2011). Briefly, a green laser of 532 nm with an optical power on the sample of 2.5 mW was used. The laser was focused onto the sample using an objective lens of 40x and a numerical aperture of 0.6. The resolution was 0.54 µm laterally (x-y) and 0.90 µm (z) axially. x-y sectional images were obtained by translating x-y motorized stage (Prior Scientific, Inc., Rockland, MA) with exposure time of 0.2 second. After epi-detection of the Brillouin scattering light, a two-stage VIPA spectrometer and an EMCCD camera (iXon Du-897; Andor, Belfast, Northern Ireland) were used to image the Brillouin frequency shifts. LABVIEW (National Instruments, Austin, TX) was used for system automatic control and the data acquisition.

For all image acquisition, samples were mounted between slide and cover slip for imaging. For the time-lapse imaging, samples were placed immediately back to the in vitro growth chamber following each image acquisition. ROIs were traced at each time point manually; after taking an image of the ROI at time 0, the shape of the cotyledon was roughly drawn in a squared notebook using the 5x objective. The ROI was identified on the drawing. Based on the drawing, the ROI was traced back at the following time points.

2.6.8 Image analysis

Cell shape metrics analysis was done with ImageJ software (http://imagej.nih.gov/ij). Maximum projections of z-stack images were used for the analysis. Cell outlines were traced manually. Area, perimeter, convex hull fit and circularity (4π (area/perimeter2)) were determined automatically for each cell by the ImageJ software. The lobe number was counted manually and represents all convex bends in the cell wall excluding those at tricellular junctions (Supplementary Note 1). The aspect ratio of the lobe represents the ratio of depth/width of the lobe. The width is the length of the tangent between the farthest points (troughs) of the lobe. The depth is the distance between the midpoint of the width and the tip of the lobe. Any curvature that has a width of at least one pixel (0.66 μm) was considered as a lobe. Data of the cell shape metrics at days 1, 2, 3, and 4 after germination were taken from different seedlings. Shape metrics data of 1 day after germination represent all the cells in the image excluding dividing cells and stomata. In order to exclude newly divided cells, the shape metrics data of 2, 3 and 4 days after germination considered all cells in an image that had an area above the smallest area value measured in the dataset of the previous day.

For all analyses, the tips of the lobe/neck regions were defined as follows. A straight line (reference line) was drawn as a tangent between the troughs of the lobe. The reference line was then shifted in parallel direction until it reached the farthest point of the lobe of interest. The point was considered as the tip of the lobe. For the anisotropy of cortical microtubules, dynamics of demethyl-esterified pectin, cellulose alignment and the stiffness of the periclinal wall analysis, ROIs were selected as circular shapes with area of 4-9 μm^2 at the tip of lobe/neck region. Relative difference in the signal intensity between neck and corresponding lobe region equals (signal intensity at the neck region - signal intensity at the lobe region) / signal intensity at the neck region. To examine the temporal correlation between the dynamics of demethyl-esterified pectin and cortical microtubules at developing cell border curvatures, maximum projections of z-stacks were used. The cell border segment of interest was chosen based on the curvature at 18 H, and traced back to a straight segment at time 0. The circular ROI was placed on the neck side of the cell border at a (future) peak curvature and two identically sized ROIs were placed left and right on the same side of the border. The signal intensity of the central ROI was divided by the mean intensity signal of the two adjacent ROIs. Brightness and contrast adjustments were done on individual z-stack to ensure optimal contrast of microtubules and propidium iodide staining on the presented micrographs. For each image, the signal from unstained regions was considered as background signal for the analysis of microtubules and spatial occurrence of demethyl-esterified pectin. The average value of the background signal was subtracted from the fluorescence intensity value determined for the ROI. The grayscale of some fluorescence micrographs was inverted for better visualization. All quantitative analyses were done on the original grayscale fluorescence micrographs.

The FibrilTool plugin was developed to measure the orientation of fibrillar structures (i.e. cytoskeleton) in plant cells (Boudaoud et al., 2014). It was used in this study to determine the anisotropy of the cortical microtubules during the time-lapse analysis. Maximum intensity projections of z-stack images were used for the analysis. The curvature of the lobe during the time-lapse analysis was determined using Kappa, a Fiji plugin for curvature analysis.

To examine the cellulose alignment in the periclinal wall of the pavement cells, an optical section showing the periclinal wall of the ROI was used. The signal from unstained regions, for each image independently, was considered as a background signal. This value was subtracted from the signal value of the ROI. The anisotropy analysis was based on the fluorescence emission at the different angles (Eq.3). The mean orientation and anisotropy at each pixel were measured based on the variation of fluorescence intensity that was detected by different emission paths. A MATLAB code, RTFluorPolGUI developed by Dr. Shalin B. Mehta of the Marine Biological Laboratory, Woods Hole, USA (Mehta et al., 2016), was used to measure the fluorescence anisotropy of the cellulose stained with S4B at each pixel. Brightness and contrast adjustments were done on the presented micrographs.

For Brillouin scattering analysis, spectrum data acquired by the camera were fitted with the Lorentzian function to determine Brillouin frequency shifts. De-ionized water and the bottle glass with known Brillouin frequency shift were used for the calibrations of the frequency-pixel conversion ratio (GHz per pixel) and the free spectral range in our spectrometer. Before and after Brillouin measurement, fluorescence images of pavement cells were taken for the co-localization of the ROI. A defined region of the fluorescence image was further chosen for the Brillouin measurement. After the measurement, the fluorescence image of the cell wall and the Brillouin frequency shift image were aligned using ImageJ software. The grayscale value of each pixel in the Brillouin scattering image represents the frequency shift in the GHz. ROI at the tip of the neck/lobe regions was defined and the pixel values were recorded.

2.7 Figures

Figure 2.1

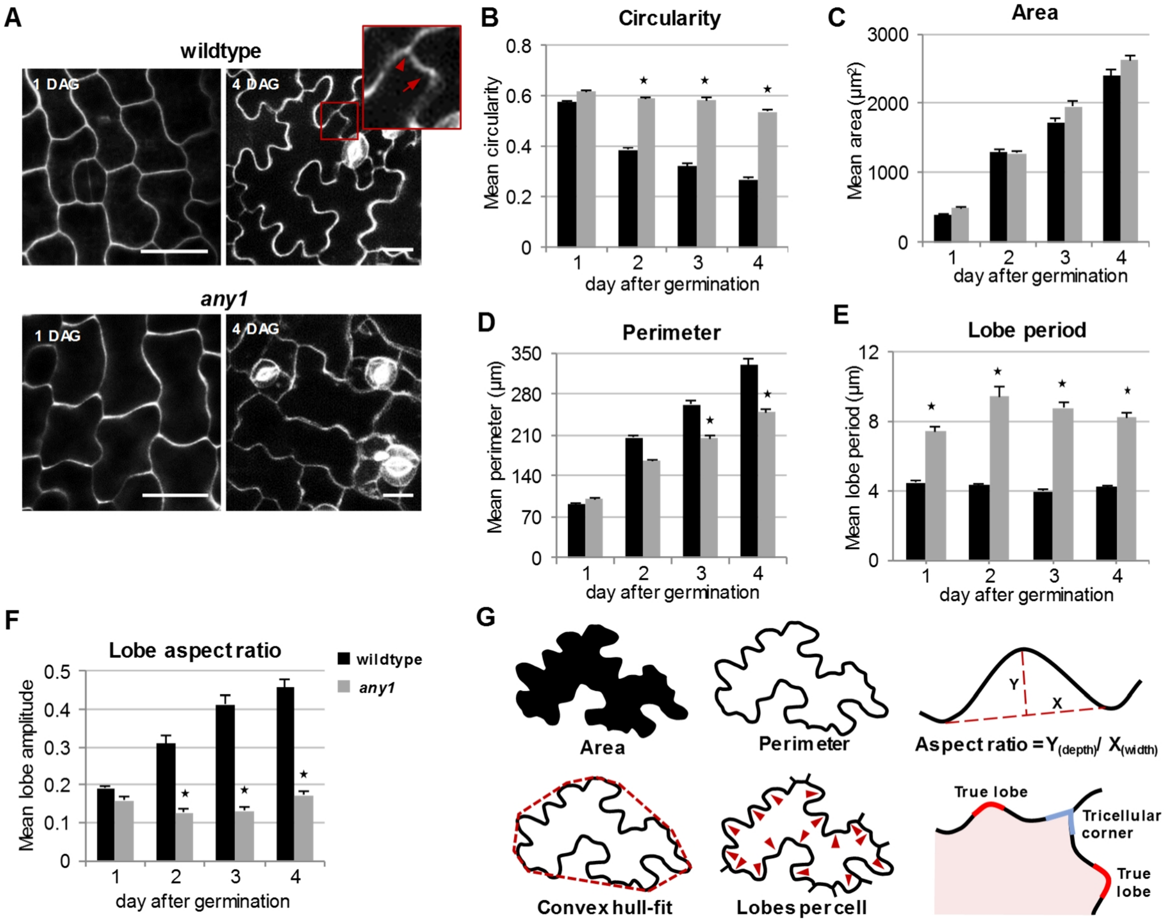

Figure 2.1: Shape analysis of *Arabidopsis* pavement cells of wildtype and *any1* mutant.

A, Fluorescence micrographs of pavement cells on the abaxial side of a cotyledon at 1 day (left panel) and 4 days (right panel) after germination of wildtype (upper row) and *any1* mutant (lower row) stained with propidium iodide. Scale bar = 20 µm. Cell border enclosed in the red rectangle is magnified to show the difference between true lobe (arrow) and tricellular junction (arrowhead). **B to F**, Developmental changes in the mean circularity (B), cell area (C), cell perimeter (D), lobe period (E) and lobe aspect ratio (F) of the wildtype (black bars) and *any1* mutant (gray bars) pavement cells from 1 to 4 days after germination. Lobe period equals square root convex hull area divided by number of lobes per cell. **G**, Illustrations of cell area, cell perimeter, lobe aspect ratio, convex hull-fit, number of lobes per cell and difference between true lobe and tricellular junction. Lobe aspect ratio in F is the ratio of depth/width of the lobe. Error bars represent the standard error. 55 > N > 40 cell from 6 to 8 seedlings for each measurement. Asterisks indicate statistically significant differences between wildtype and *any1* mutant pavement cells of the same developmental stage ($P < 0.001$, *student's t*-test). The mean lobe aspect ratio in F represents all the true lobes in the measured cells.

Figure 2.2

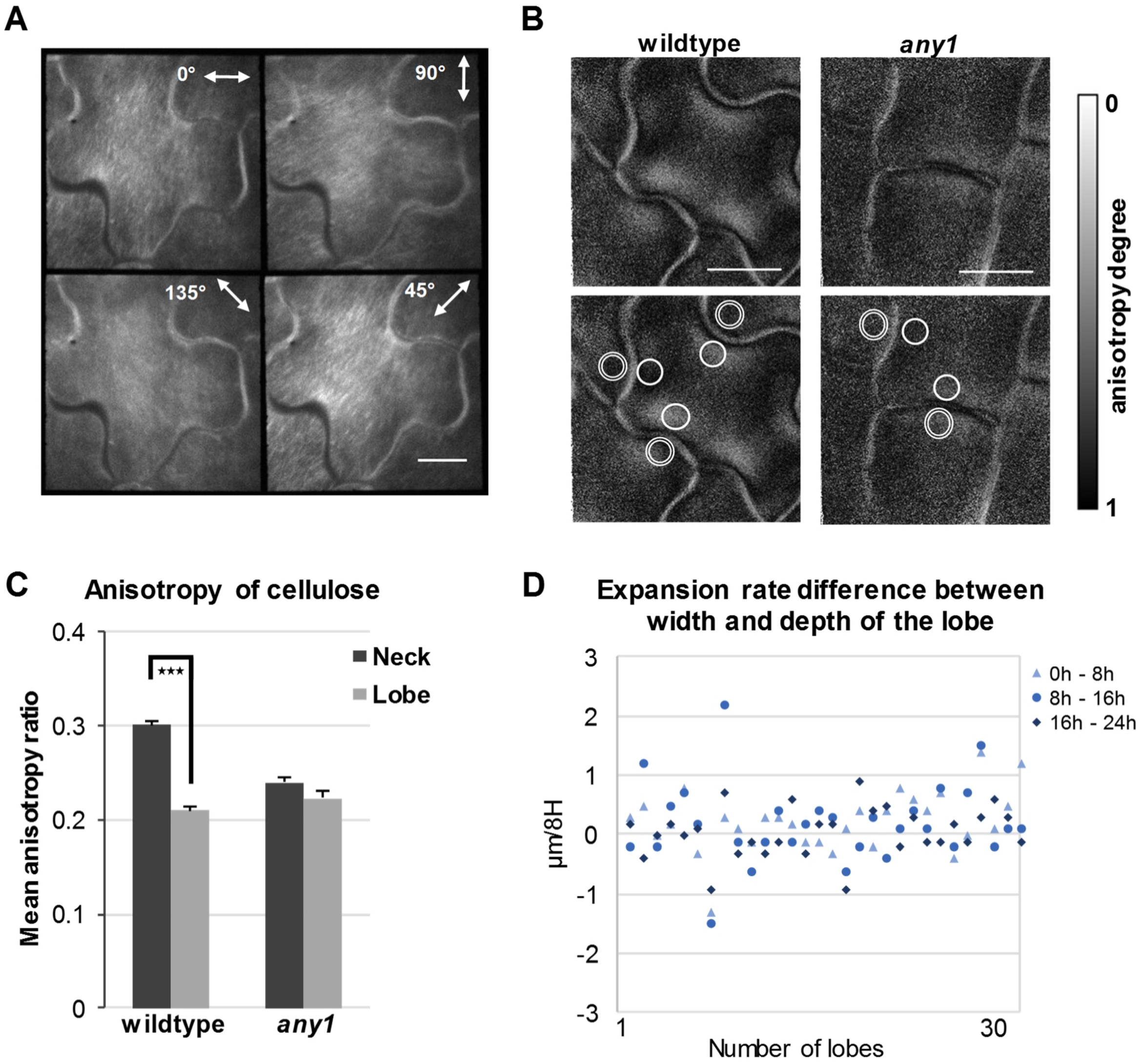

Figure 2.2: Cellulose alignment at the periclinal wall of wildtype and *any1* mutant pavement cells.

A, Fluorescence polarization at four different angles of cellulose microfibrils stained with S4B at 3 days after germination of wildtype pavement cell. **B**, Anisotropy degree of cellulose microfibrils represented by the pixel intensity at 1 day after germination of wildtype (left panel) and *any1* mutant (right panel) pavement cells. Upper and lower panels represent the same micrographs. Double lined circles (lobe regions) and solid lined circles (neck regions) in the lower panel indicate examples of ROIs used for graph C. Scale bars = 10 µm. **C**, Anisotropy of cellulose alignment at the neck and the corresponding lobe regions of the wildtype and *any1* mutant at 1 day after germination measured based on the signal intensity of each pixel at different emission angles. Error bars represent the standard error. Asterisks indicate statistically significant differences ($P < 0.001$, *paired t*-test). N = 54 necks and adjacent lobes of the same undulation. All necks from 2 or 3 cells taken from 13 and 16 seedlings for wildtype and *any1* mutant, respectively, were used in this analysis. **D**, Difference in the expansion rates between the width and the depth of the lobe at the early stages of lobe formation in the wildtype. The same lobe was monitored over 24H at 8H intervals. The difference in expansion rates between the width and the depth of the lobe was calculated as ((width$_{tH}$ – width$_{tH\text{-}8H}$) – (depth$_{tH}$ – depth$_{tH\text{-}8H}$)). N = 30 lobes. All lobes from 2 cells from 3 different seedlings were used in the analysis.

Figure 2.3

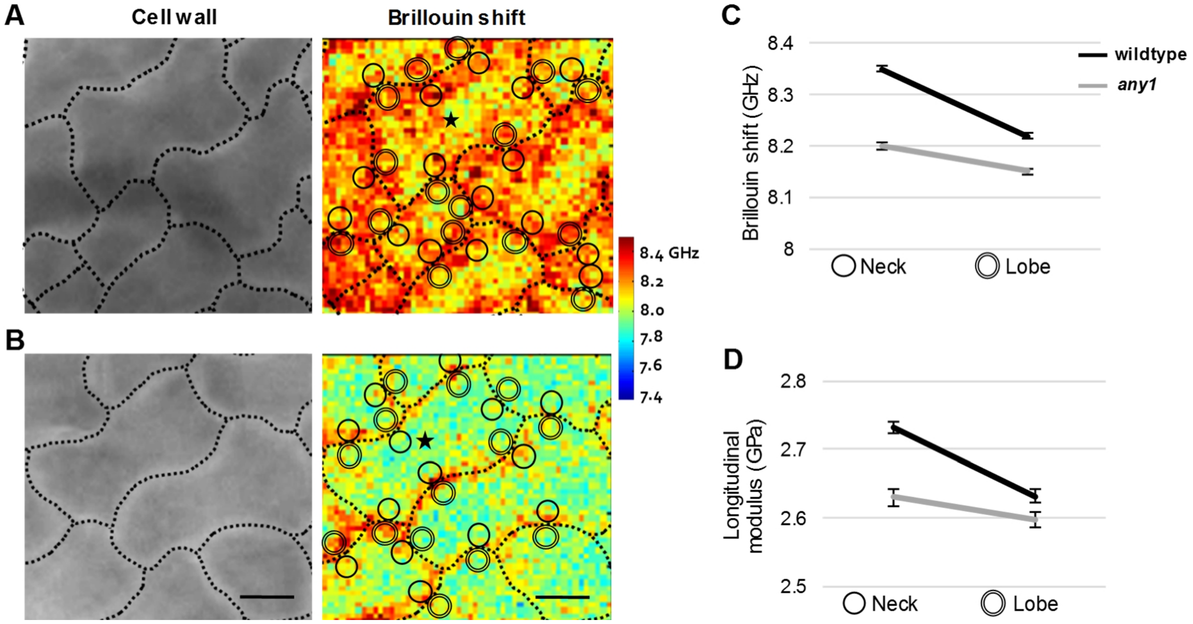

Figure 2.3: Mechanical stiffness of the periclinal wall of the wildtype and *any1* mutant pavement cells assessed by Brillouin microscopy.

A and B, Fluorescence micrograph (propidium iodide label, left panel) and Brillouin shift (stiffness map, right panel) of wildtype (A) and *any1* mutant (B) pavement cells at 1 day after germination. The Brillouin shift is given in GHz and presented as heatmap. In the micrographs, the dotted lines indicate cell outlines. Double lined circles (lobe regions) and solid lined circles (neck regions) indicate examples of ROIs used for figures C and D. ROI = 9 µm^2 and pixel size = 1 µm^2. Asterisks indicate the central region of a cell where the Brillouin shift in the *any1* mutant is significantly reduced compared to the wildtype (P < 0.001, *student's t*-test). N = 25 cells for wildtype and *any1* mutant. **C and D**, The mean value of Brillouin shift (C) and the calculated longitudinal modulus (D) of the neck and the corresponding lobe regions in the wildtype (black line) and *any1* mutant (gray line) pavement cells. Error bars represent the standard error. N = 40 necks and corresponding lobes of the same undulation. All necks from 2 or 3 cells from 6 seedlings for wildtype and *any1* mutant were used in this analysis. Scale bar = 10 µm.

Figure 2.4

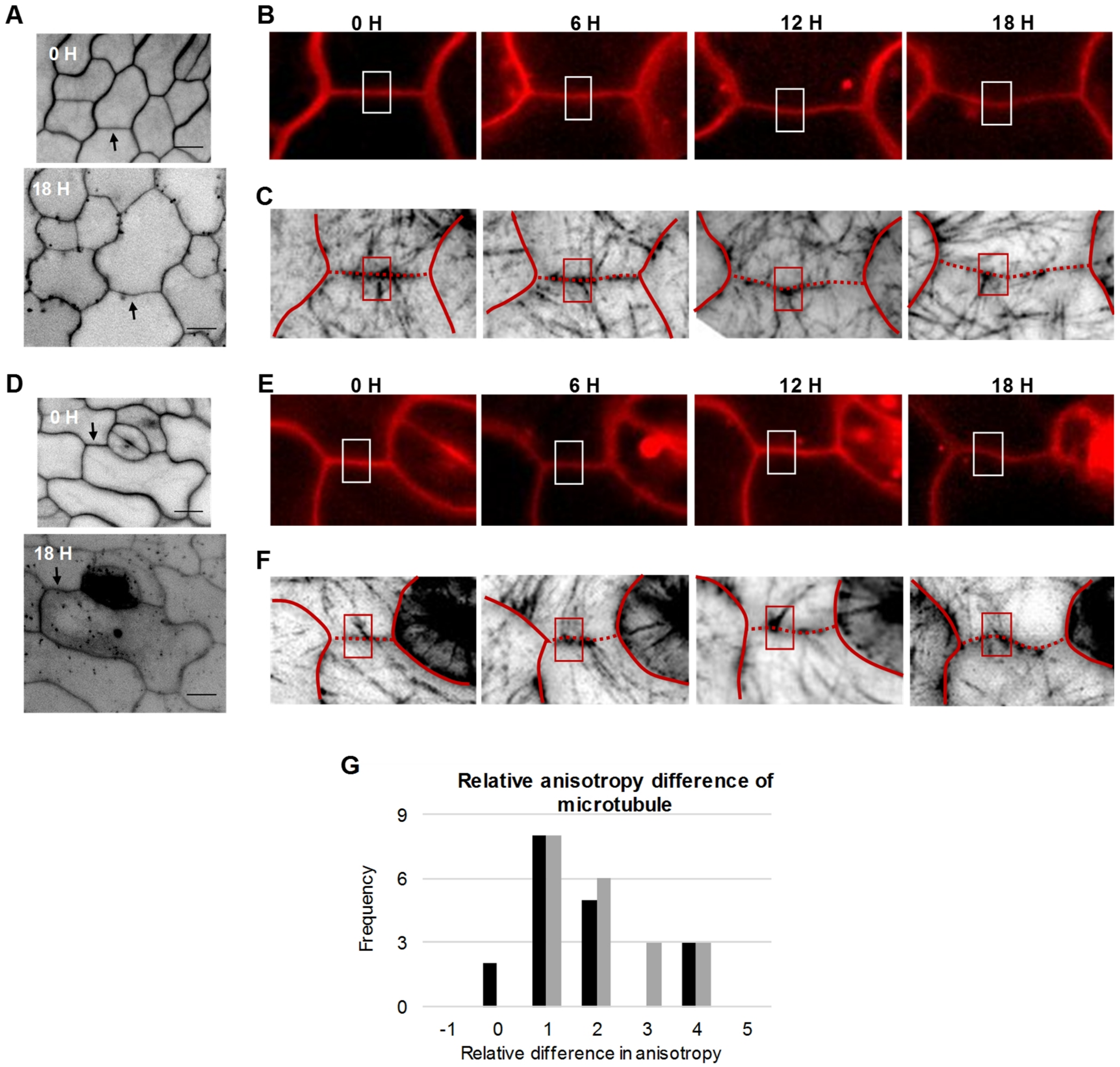

Figure 2.4: Arrangement of cortical microtubules during the development of undulations in wildtype and *any1* mutant pavement cells expressing GFP:TUB6.

A to F, Fluorescence micrographs of wildtype (A - C) and *any1* mutant (D - F) pavement cells at 1 day after germination monitored over 18 hours. The cell wall (stained with propidium iodide in A, B, D and E) and cortical microtubules (GFP:TUB6, C and F) were visualized in 6 hour time-lapse intervals. Arrows in A and D indicate the cell wall region that is represented in time-lapse images. Rectangles in in B and E indicate the region on the anticlinal wall forming an undulation. C and F show the arrangement of cortical microtubules at the periclinal wall during the initiation and the development of the bend (rectangles). Red lines in C and F trace the anticlinal wall that is shown in B and E, respectively. The dotted regions in C and F represents the anticlinal wall of interest. **G**, Frequency of the relative difference in cortical microtubule anisotropy between the prospective neck and the corresponding lobe of the same undulation at time 0 at the periclinal wall in GFP:TUB6 (black bars) and

GFP:TUB6/*any1* (gray bars). N = 18 necks and 18 adjacent lobes from 7 seedlings for GFP:TUB6 and 20 necks and 20 adjacent lobes from 11 seedlings for GFP:TUB6/*any1* mutant. Scale bars = 10 µm.

Figure 2.5

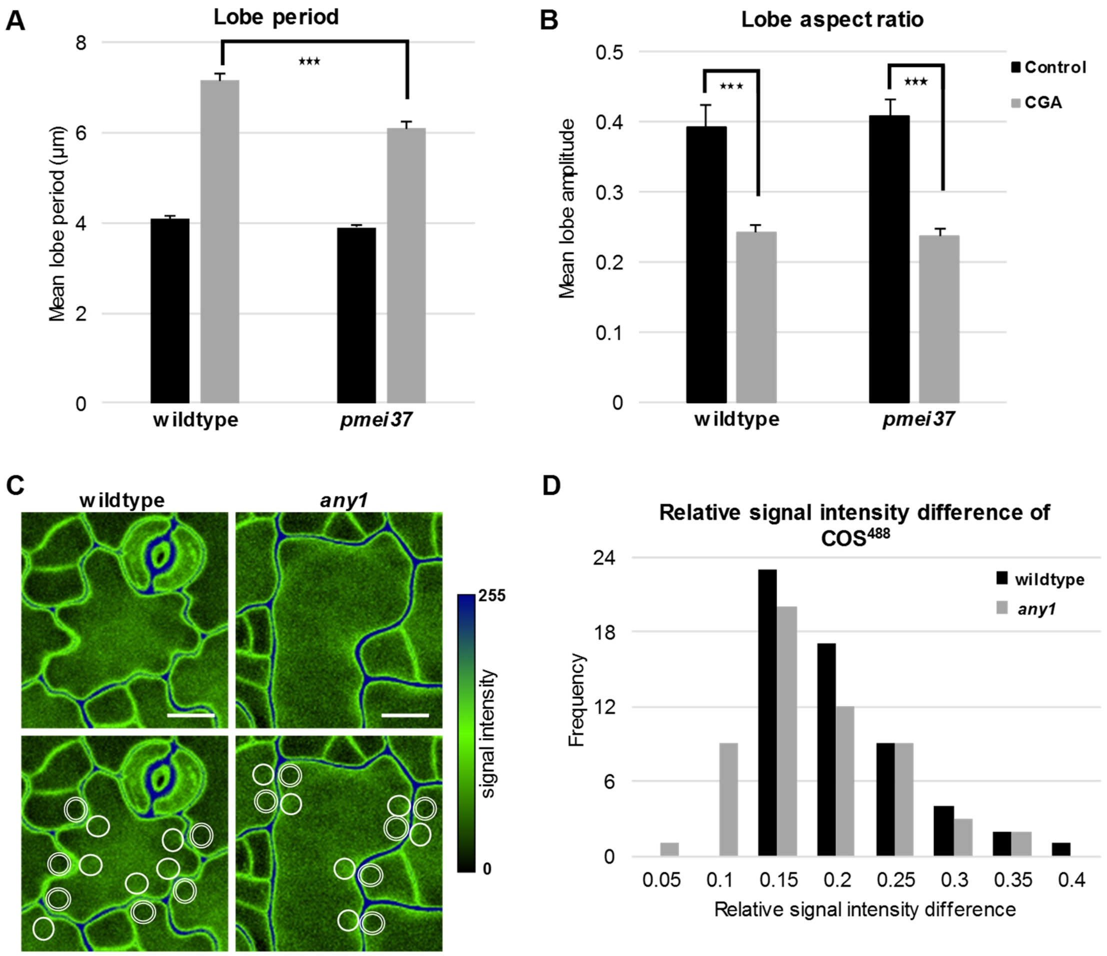

Figure 2.5: Role of demethyl-esterified pectin in the shaping of pavement cells.

A and B, Mean lobe period (A) and mean lobe aspect ratio (B) in wildtype and *pmei37* at 4 days after germination for control (DMSO; black bars) and seedlings grown in the presence of CGA (grey bars). Error bars represent standard error. 70 > N > 50 cell from 10 to 15 seedlings for each measurement for A and N = all lobes of 12 cells from 8 seedlings for each measurement for B. Asterisks indicate statistically significant differences ($P < 0.001$, *student's t*-test). **C**, Fluorescence micrographs (maximum projection of z-stacks) of wildtype (left panel) and *any1* (right panel) at 1 day after germination of the pavement cells stained with COS^{488}. Upper and lower panels represent the same micrographs. Double lined circles (lobe regions) and solid lined circles (neck regions) in the lower panel indicate examples of ROIs used in figure D to calculate the abundance of demethylated pectin at lobe/neck pairs. Scale bar = 10 µm. **D**, Distribution of the relative differences in the signal intensity of COS^{488} between the neck and the corresponding lobe of the same undulation. N = 56 necks and 56 corresponding lobes from 7 seedlings for wildtype and *any1*.

Figure 2.6

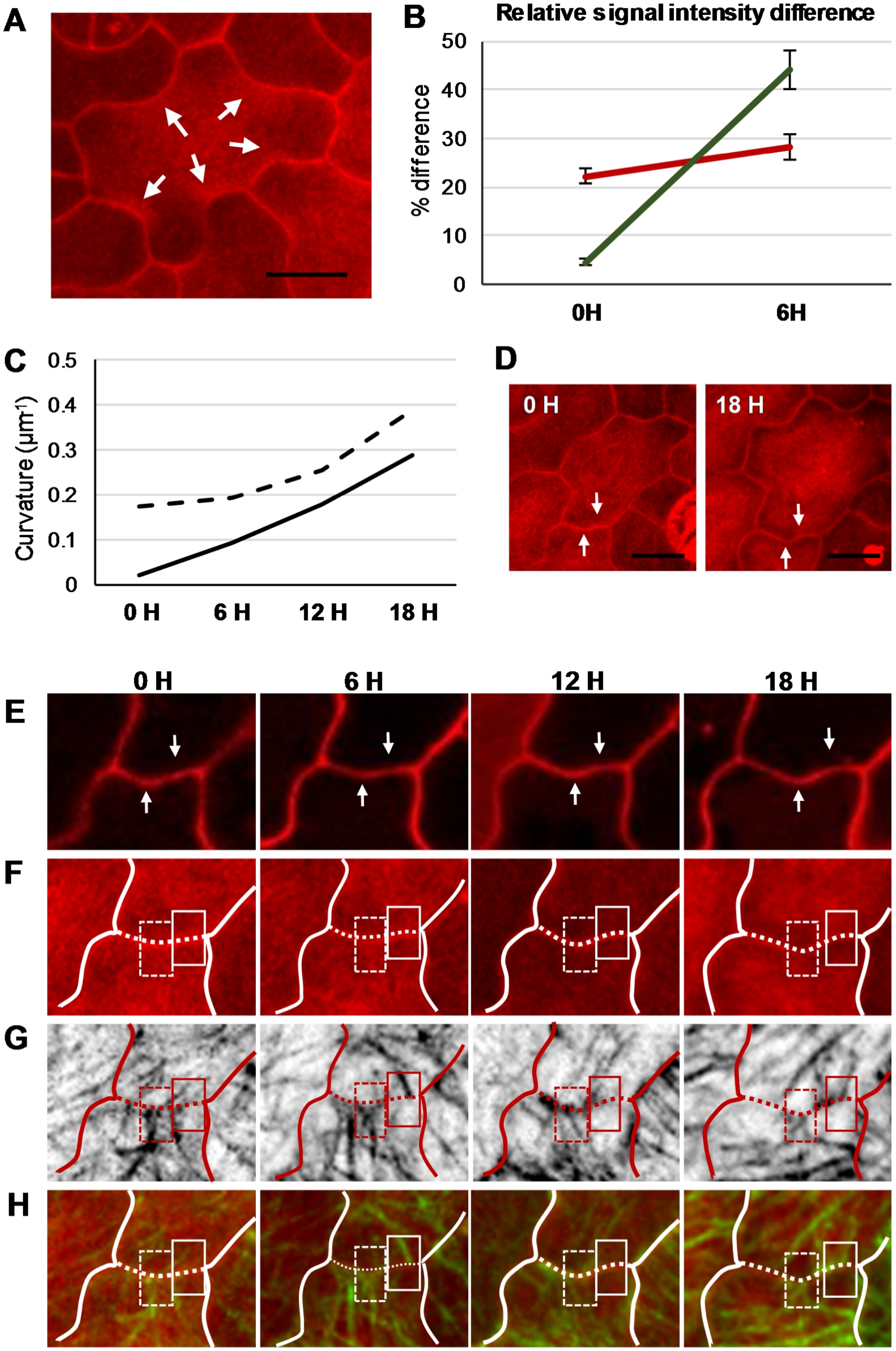

A
B
Relative signal intensity difference
% difference
0
10
20
30
40
50
0H
6H
C
Curvature (μm⁻¹)
0
0.1
0.2
0.3
0.4
0.5
0 H
6 H
12 H
18 H
D
0 H
18 H
0 H
6 H
12 H
18 H
E
F
G
H

Figure 2.6: Temporal correlation between the dynamics of demethyl-esterified pectin and cortical microtubules at developing cell border curvatures.

A, Fluorescence micrograph (maximum projection of z-stack) of pavement cells stained with propidium iodide of wildtype at 1 day after germination. Arrows indicate local enrichment in propidium iodide label at the neck regions of developed cell border curvatures. **B**, Relative differences in the signal intensity of propidium iodide (red) and GFP:TUB6 (green) label between prospective necks and adjacent regions at the periclinal wall at times 0 and 6 hours. N = 17 prospective neck regions from 3 seedlings. Error bars represent the standard error. At time 0 all measured cell border regions were straight, whereas at 6h they showed slight but discernible curvature. **C**, Evolution of curvature (calculated as reciprocal of its radius) in the two cell border regions indicated in D-H over a 18 hour observation period. Black dashed and solid lines represent the cell border segments identified by white dashed and solid rectangles in F-H, respectively. The black/white dashed line/rectangle indicates a cell border segment that is already curved at time 0, whereas the black/white solid line/rectangle identifies a cell border segment that is straight at time 0 and develops a curvature by 18h. **D-H**, Fluorescence micrographs of wildtype epidermis monitored over 18 hours and visualized in 6 hour time-lapse intervals. **D**, Maximum projections of z-stacks of sample shown in E-H, stained with propidium iodide. **E**, Single optical sections of sample shown in D, showing the anticlinal wall stained with propidium iodide over time. Arrows in D and E indicate two cell border segments monitored in the time-lapse series (upward pointing arrow – curvature present at time 0; downward pointing arrow – straight at time 0). **F**, Maximum projections of z-stacks showing propidium iodide signal for demethyl-esterified pectin. **G**, Maximum projections of z-stacks showing cortical microtubules at the periclinal wall (GFP:TUB6). In F and G, the dashed rectangles indicate a segment of cell border that is already curved at time 0 illustrating that demethylated pectin and microtubules are enriched at the neck side from the beginning of the observation and through the subsequent hours. The solid rectangles indicate a segment of cell border that is straight at time 0 and starts curving during the subsequent hours. The solid rectangles illustrate enrichment of demethylated pectin at the prospective neck region before the curve appears and no difference in microtubule density between the two sides of the line before the curvature appears (i.e. time 0) with microtubule signal only appearing after time 6h. **H**, Merge of the propidium iodide and the GFP:TUB6 signals. White lines in F and H and red line in G trace the anticlinal wall that is shown in E. The dotted regions of the white lines in in F-H represent the anticlinal wall of interest. Scale bars = 10 µm.

Figure 2.7

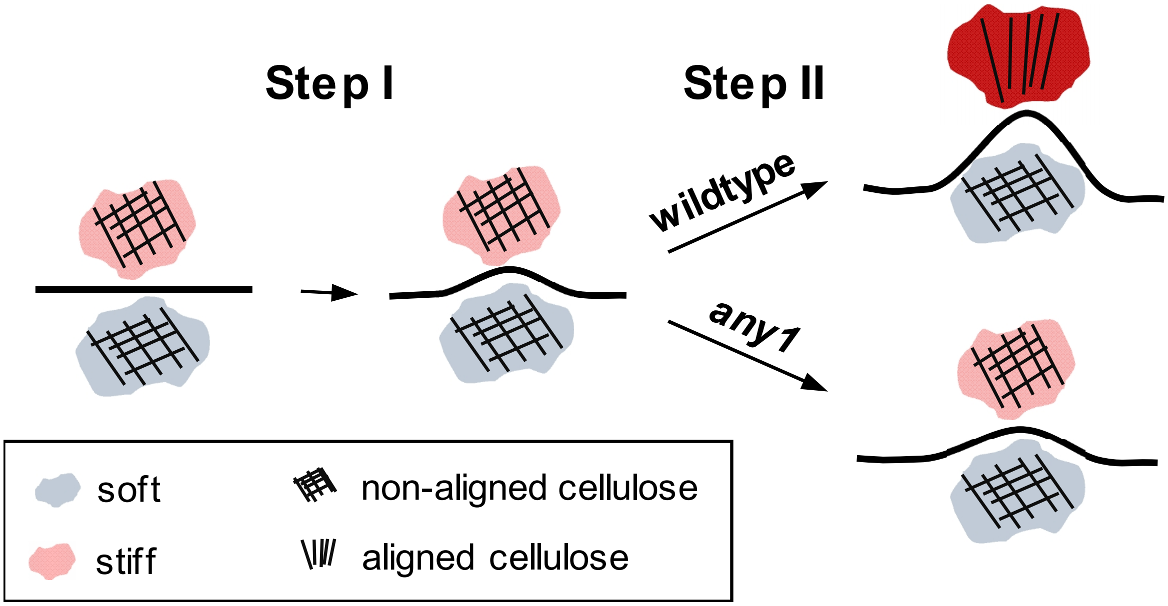

Figure 2.7: Proposed two-step mechanism for undulation formation during the development of pavement cells.

In the first step, an increase in the wall stiffness at a prospective neck region is generated through localized enrichment in demethylated pectin. The increased stiffness at the prospective neck side of the undulation leads to differential expansion of the periclinal wall during cell growth with the neck side expanding less than the opposing lobe side. The resulting symmetry break and stiffness differential generate a local elevation of stress (Sampathkumar et al., 2014; Bidhendi et al., 2019), which in turn attracts accumulation of microtubules at the neck (Hamant et al., 2008), resulting in deposition of cellulose, and by consequence, an augmentation of lobe expansion through a feedback loop. This feedback driven augmentation of lobe depth is absent in the *any1* mutant, where cellulose crystallinity and alignment are low.

2.8 Supplemental data

2.8.1 Supplementary Note 2.1: Distinction between true lobes and tricellular junctions

Pavement cells have two types of protrusions that are generated by entirely different processes. Tricellular junctions are formed through the deposition of a dividing wall during cytokinesis (Supplemental Fig. 2.2A), whereas undulations in an existing wall segment are formed through the processes discussed in the present paper. Although they resemble lobes, tricellular junctions were therefore excluded from the lobe count analyses. Recently developed automated lobe counting tools such as skeleton methods and lobe finder (Wu et al., 2016) do not distinguish between true lobes and tricellular junctions in pavement cells, but we consider this distinction crucial. Our choice is supported by the fact that including tricellular junctions in the lobe number count partially masks the difference between the *any1* mutant and the wildtype (Supplemental Figs. 2.2B,C). Thus, in this study, we focus exclusively on true lobes. To distinguish a true lobe from a straight cell border it had to have a curvature with the depth (Fig. 2.1G) of at least one pixel. In our study one pixel equals to 0.66 μm.

We opted for the terms lobe (also used by Fu et al. (2002), Panteris and Galatis (2005) and Zhang et al. (2011)) and neck (Fu et al., 2002; Fu et al., 2005) for ease of reading. Terms used by others include ‘constriction’ (Panteris and Galatis, 2005) ‘indent’ or ‘indentation’ (Fu et al., 2005) (‘neck’ in our terminology) and protrusion (Zhang et al., 2011) (‘lobe’ in our terminology). We avoid the terms ‘convex’ and ‘concave’ since they require a reference frame and might therefore lead to misunderstanding (‘convex’ is used by Zhang et al. (2011) to indicate a protrusion (lobe) using the cell as a reference, but by Armour et al. (2015) and Majda et al. (2017) to indicate an indent (neck) with the anticlinal wall as reference). We prefer to avoid all nomenclature related confusion while keeping the terms as intuitive as possible.

2.8.2 Supplementary Note 2.2: Calculating the longitudinal modulus

The Brillouin frequency shift (BFS) is related to the longitudinal modulus of material based on the following equation (Scarcelli and Yun, 2007; Scarcelli et al., 2015):

$$M' = {}^{\Omega^2 \lambda^2 \rho}\!/_{4n^2} \qquad \text{(Eq. 2.3)}$$

Where M' is the longitudinal modulus, Ω is the BFS, λ is the optical wavelength, ρ is the material density, n is the refractive index. Importantly, the component of the modulus measured is along the direction of the incident laser beam, that is perpendicular to the periclinal wall and thus cellulose microfibrils. Here, we assumed the refractive index to be 1.1 g/cm^3 and the density of the primary cell wall to be 1.41 (Elsayad et al., 2016). While density and refractive index may differ between lobe and neck regions because of the different abundance of cellulose microfibrils, in biological materials, it has been shown that the ratio between the two, ρ/n^2, does not vary significantly. Therefore, BFS can be assumed to be directly related to the longitudinal modulus (Scarcelli et al., 2015; Elsayad et al., 2016).

2.8.3 Supplementary Note 2.3: Effect of cell geometry on the detected BFS

In Brillouin spectroscopy, one consequence of geometrical effects of the sample could be local variations in signal intensity that are not caused by the mechanical properties of the material but by its geometry. Brillouin shift is normally independent from signal intensity of Brillouin scattering. However, in the circumstance of a large loss in signal intensity, an artifact may be present only due to an inability to fit the Lorentzien function to the spectrum during post-processing. In the present study, to ensure that there was no substantial variation in signal intensity caused by pavement cell geometry, we quantitatively measured the Brillouin signal intensity corresponding to the neck and lobe ROIs. The difference in the signal intensity between the neck and the corresponding lobe of the same undulation was typically below 15 percent (Supplemental Figs. S4B and C). Importantly, the data points did not show any bias for lobe or neck as they were evenly distributed above and below 0% difference.

2.8.4 Supplementary figures

Supplemental Figure 2.1

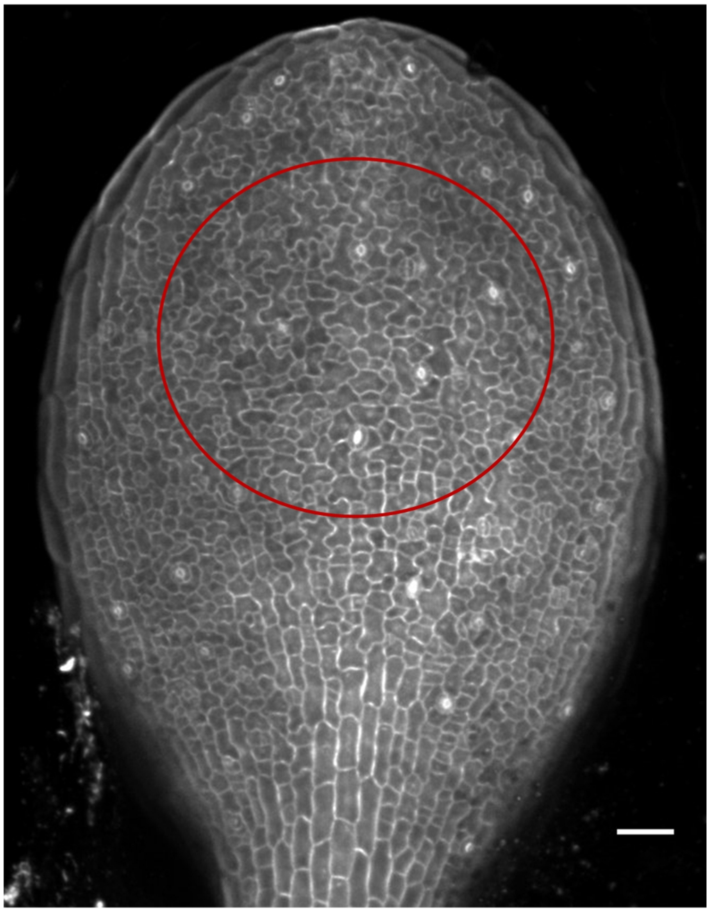

Supplemental Figure 2.1: Region of interest (ROI) used in this study.

Fluorescence micrograph of pavement cells on the abaxial side of a cotyledon stained with PI at 1 day after germination of wildtype showing the region of interest used in this study (red circle). Scale bar = 50 µm.

Supplemental Figure 2.2

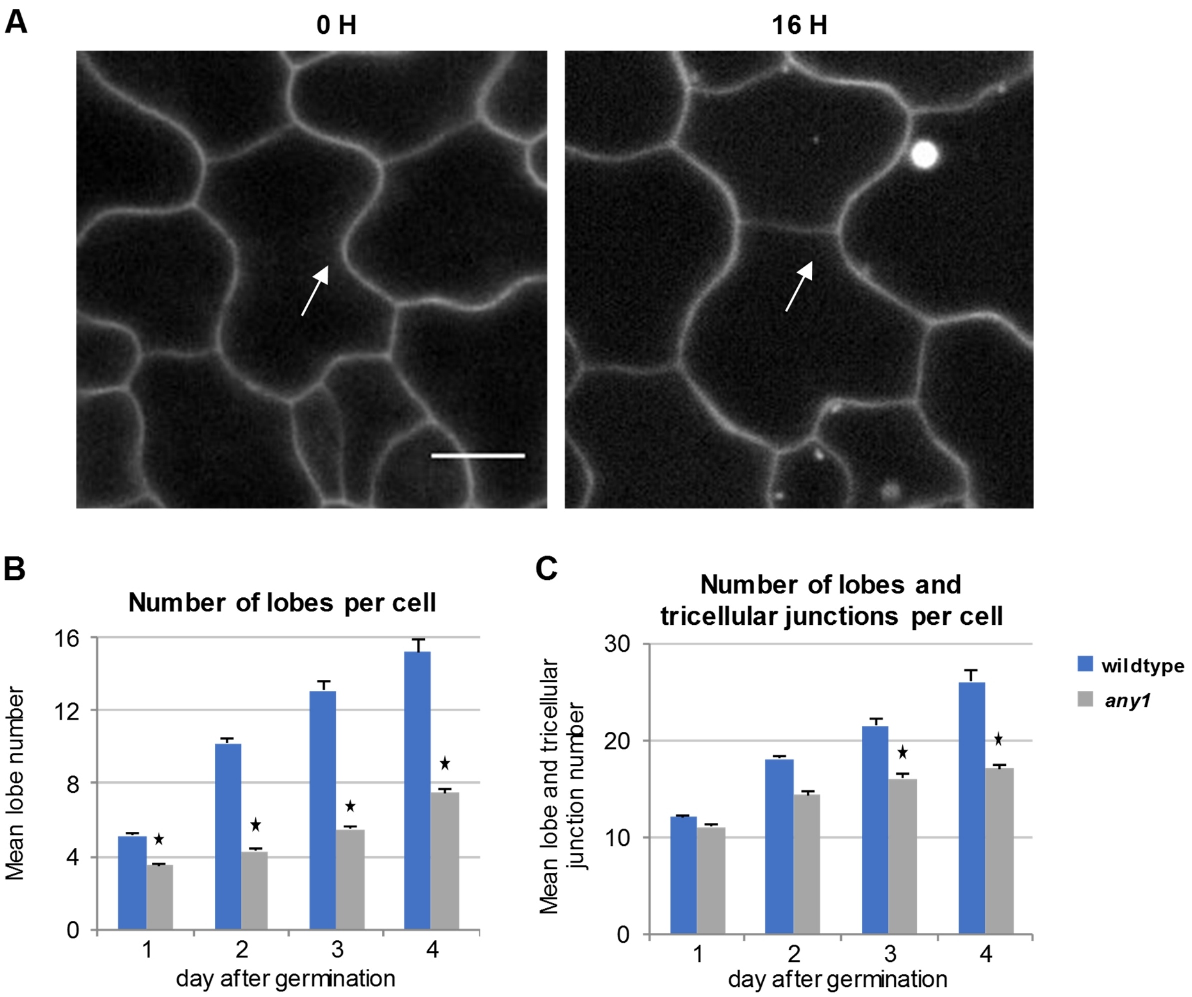

Supplemental Figure 2.2: Difference between true lobe and tricellular junction.

A, Two-time points during the development of cotyledon epidermis that illustrate the formation of tricellular junctions in pavement cells through cytokinesis. Arrow indicates the formation of the lobe-like region through the deposition of a new cell plate. Scale bar = 10 μm. **B and C**, Mean lobe number (B) and combined lobe and tricellular junction number per cell (C) in wildtype (blue bars) and *any1* mutant (gray bars) pavement cells. 55 > N > 40 cell from 6 to 8 seedlings for each measurement. Asterisks indicate statistically significant differences between wildtype and *any1* mutant pavement cells of the same developmental stage ($P < 0.001$, *student's t*-test).

Supplemental Figure 2.3

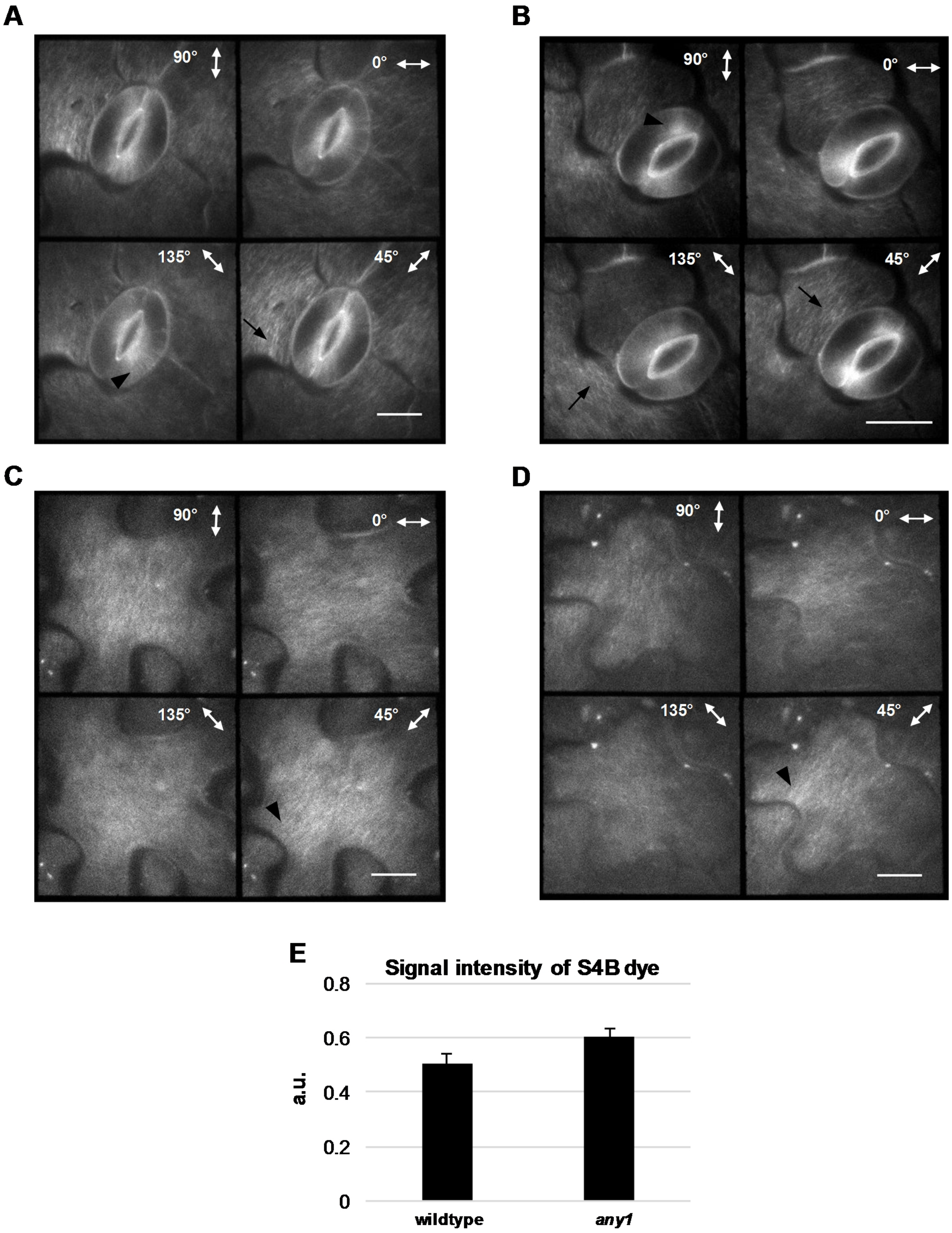

Supplemental Figure 2.3: Fluorescence polarization of S4B dye reflects the anisotropy degree of cellulose.

A and B, Polarized fluorescence signals in guard cells and surrounding pavement cells in the *Arabidopsis* wildtype at 3 days after germination stained with S4B. In A and B, the four images represent the polarization orientations at 0°, 45°, 90° and 135°. The polarized S4B signal indicated microfibrils to be arranged in radial orientation in the guard cells (arrowheads). This pattern is consistent with the documented orientation of cellulose microfibrils in this cell type (Fujita and Wasteneys, 2014). Moreover, S4B labeled cellulose microfibrils have a circular orientation in the pavement cells surrounding the guard cells (arrows), consistent with the orientation of cortical microtubules and stress patterns demonstrated previously (Sampathkumar et al., 2014). These results indicate that S4B molecules bind to cellulose microfibrils and can be used as a proxy to determine their alignment. **C and D**, Fluorescence polarization orientation of cellulose microfibrils stained with S4B, obtained from four images with different polarization orientations at 3 days after germination of wildtype pavement cells. Arrows indicate instances of predominantly perpendicular alignment of cellulose to the neck side of the undulation. Scale bars = 10 µm. **E**, Signal intensity of S4B dye staining cellulose at the neck region of wildtype and *any1* mutant pavement cells. Error bars represent standard errors. N = 54 necks and adjacent lobes of the same undulation.

Supplemental Figure 2.4

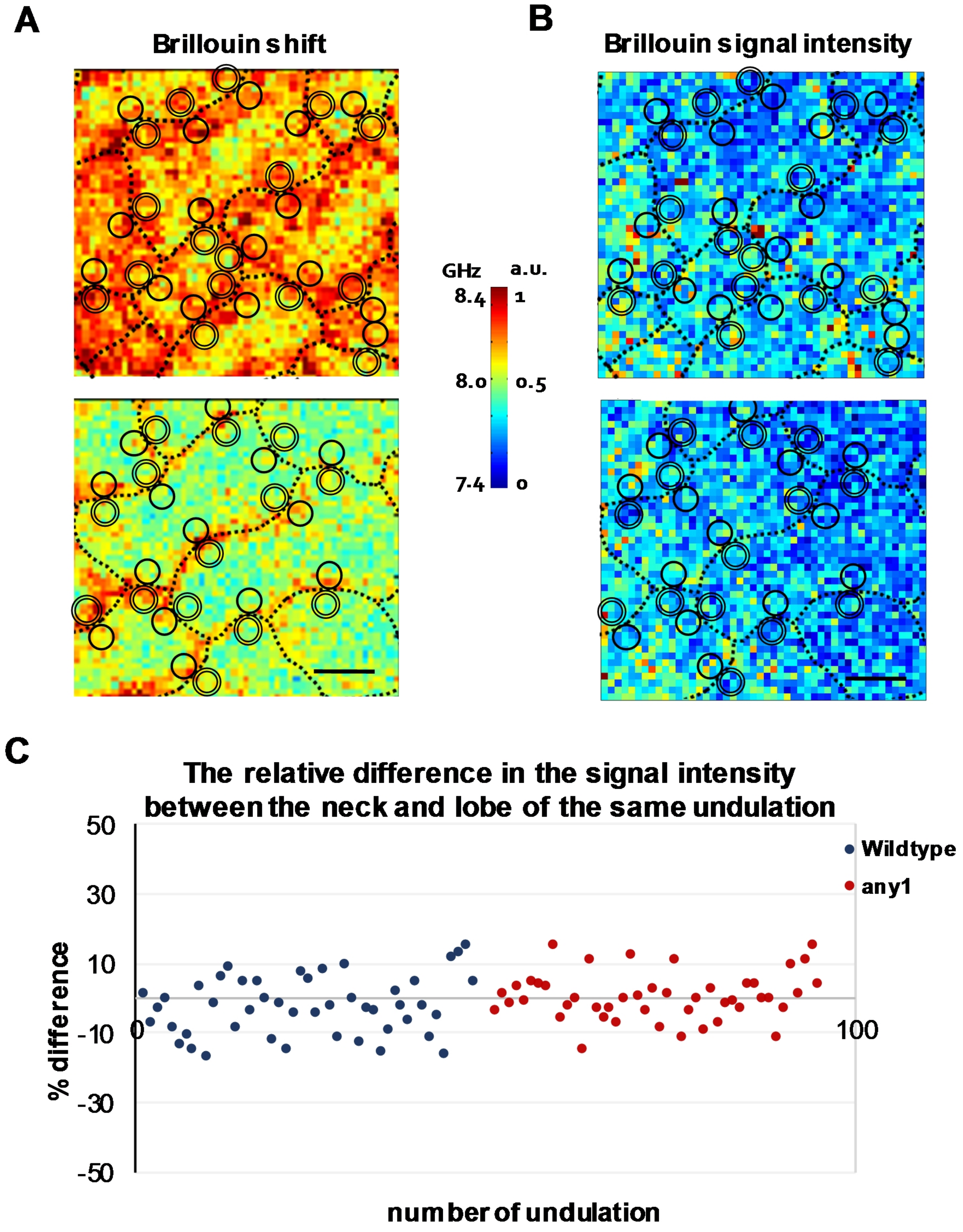

Supplemental Figure 2.4: Effect of pavement cell geometry on Brillouin signal intensity and Brillouin frequency shift.

A and B, Brillouin shift (left panel) and Brillouin signal intensity (right panel) of wildtype (A) and *any1* mutant (B) pavement cells at 1 day after germination. The Brillouin shift is given in GHz and is an indicator for the stiffness of the cell wall. Brillouin signal intensity is given in arbitrary unit (a.u.) and represents the amount of the reflected Brillouin shifts. In the micrographs, the dotted lines indicate cell outlines. Double lined circles (lobe region) and solid lined circles (neck region) indicate examples of ROIs used in C. Scale bars = 10 µm. **C**, Distribution of the relative differences in the Brillouin signal intensity between the neck and the corresponding lobe of the same undulation. The relative difference was calculated as (signal intensity at neck region – signal intensity at lobe region) / (signal intensity at lobe region). The data represent the same undulations that are used to generate Figs. 3 C and D.

Supplemental Figure 2.5

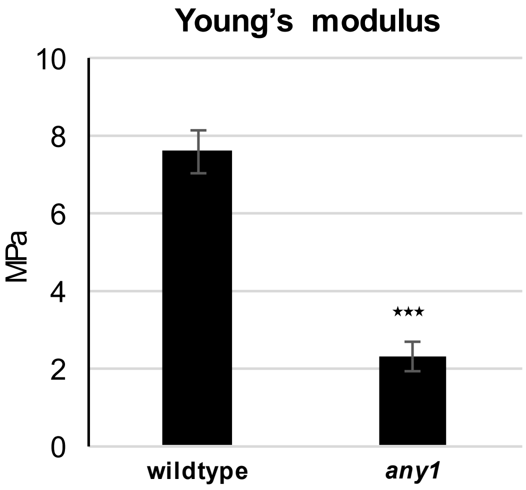

Supplemental Figure 2.5: Mechanical tensile test of wildtype and *any1* hypocotyls.

Apparent Young's modulus of plasmolyzed dark-grown hypocotyls of wildtype and *any1* mutant at 5 days after germination obtained by mechanical tensile test. Asterisks indicate statistically significant differences compared to the wildtype ($P < 0.001$, *student's t*-test). Error bars represent standard errors. N = 15 – 17 hypocotyls for each measurement.

Supplemental Figure 2.6

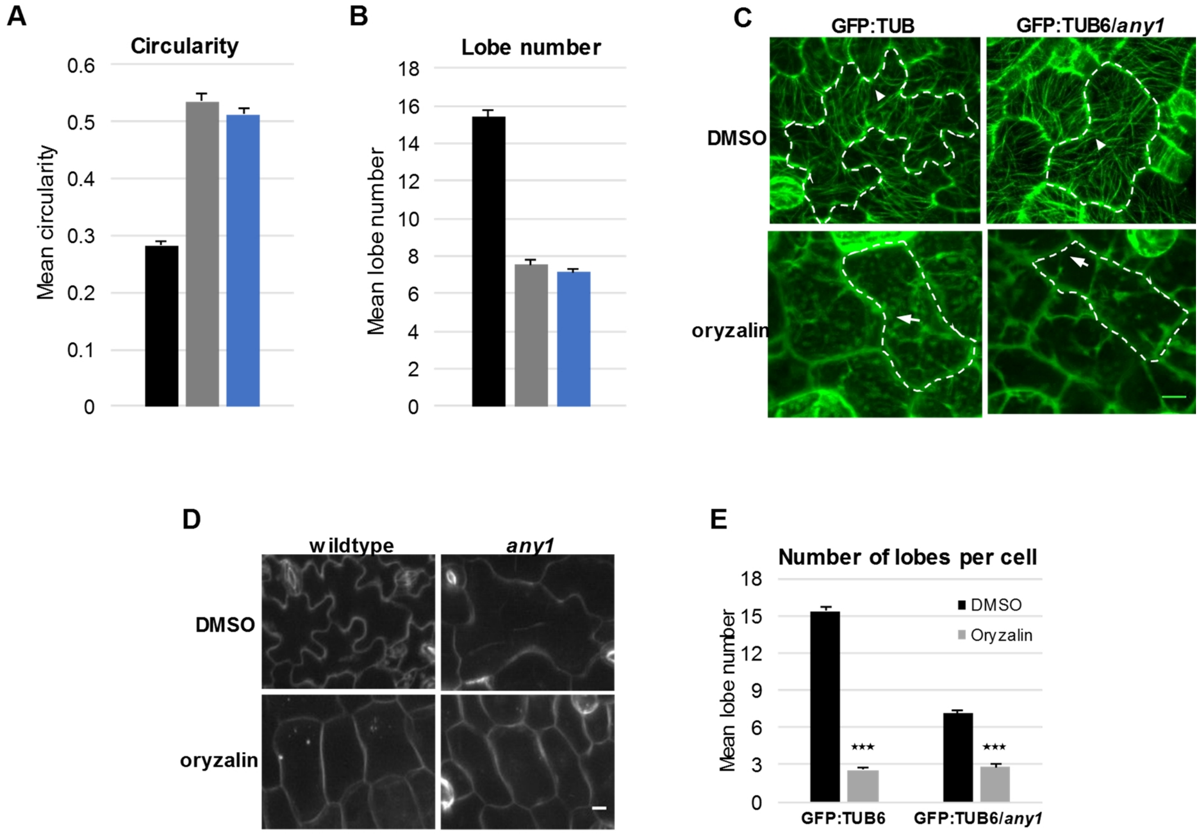

Supplemental Figure 2.6: Shape analysis of GFP:TUB6 and GFP:TUB6/*any1* pavement cells.

A and B, Changes in mean circularity (A) and lobe number per cell (B) of GFP:TUB6 (black bars), *any1* (gray bars) and GFP:TUB6/*any1* (blue bars) pavement cells at 4 days after germination. Error bars represent the standard error. N = 40 cell from 6 seedlings for each measurement. **C**, Cortical microtubules in GFP:TUB6 (left panel) and GFP:TUB6/*any1* (right panel) pavement cells in DMSO (control; upper panel) and oryzalin (lower panel) treated cells. In the micrographs, the dashed lines indicate cell outlines. Arrowheads indicate instances of presence of cortical microtubules at the neck side of the undulation. Arrows indicate instances of absence of cortical microtubules at the neck side of the undulation. Brightness and contrast adjustments were done to ensure optimal contrast of microtubules on the presented micrographs. **D**, Effect of oryzalin treatment (lower panel) on the shape of pavement cells in wildtype (left panel) and *any1* (right panel) compared to the control treatment (DMSO; upper panel). **E**, Mean number of lobes per cell in wildtype and *any1* pavement cells in oryzalin (treatment) and DMSO (control). Error bars represent standard error. N = 35 cells from 6 different cotyledons. Asterisks indicate statistically significant differences between the DMSO control and the oryzalin treatment ($P < 0.001$, *student's t*-test). Scale bars = 10 µm.

Supplemental Figure 2.7

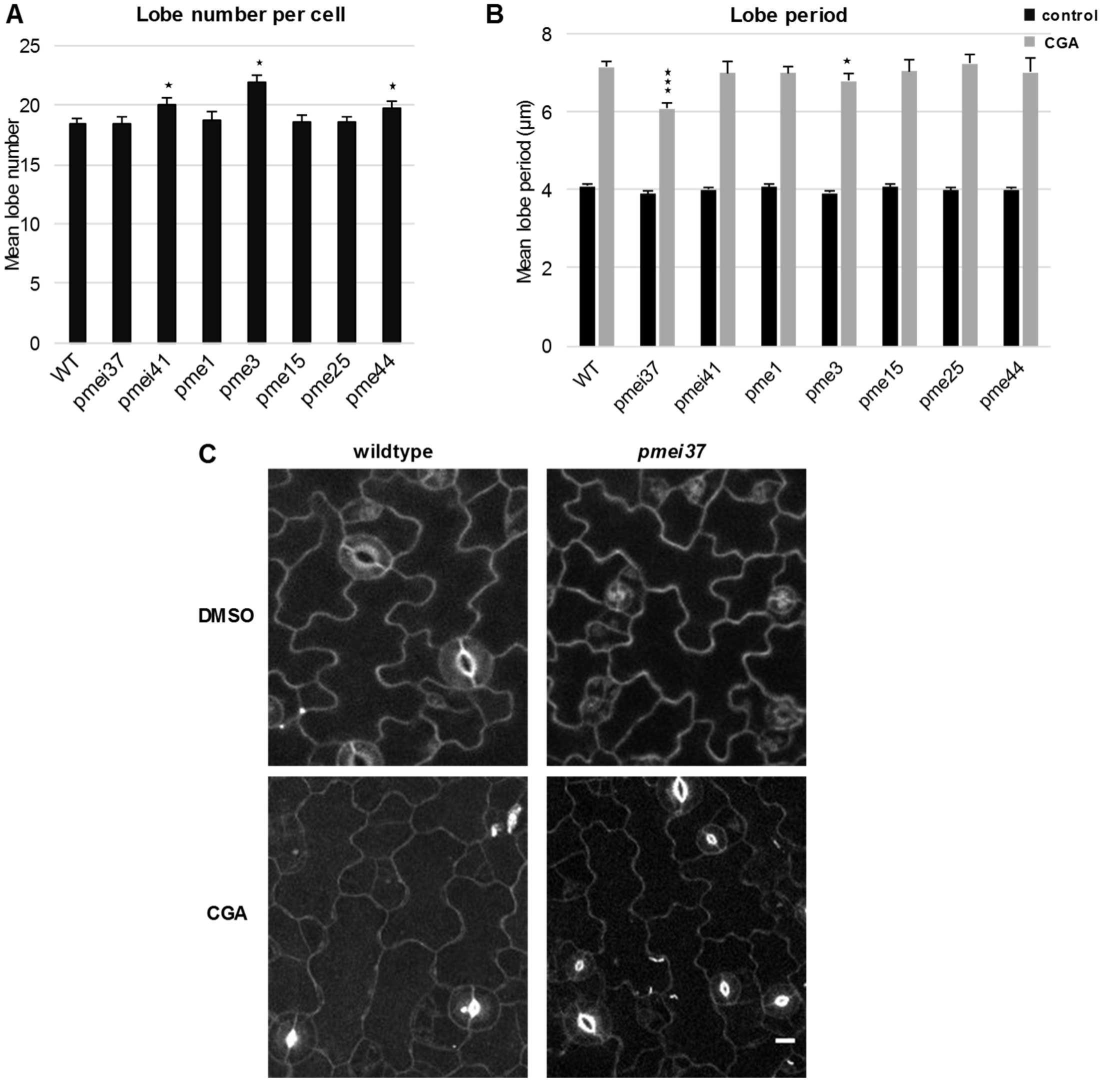

Supplemental Figure 2.7: Shape analysis of *Arabidopsis* wildtype, PME and PMEI mutant pavement cells.

A, Mean lobe number per cell of the wildtype and PME and PMEI mutant pavement cells at 4 days after germination. Asterisks indicate statistically significant differences compared to the wildtype ($0.01 < P < 0.05$, *student's t*-test). **B**, Mean lobe period of the wildtype and PME and PMEI mutants at 4 days after germination for control (black) and seedlings grown in the presence of CGA (grey). Lobe period equals square root convex hull area divided by number of lobes per cell. Asterisks in B indicate statistically significant differences compared to the wildtype of the same treatment (* for $P < 0.05$ and *** for $P < 0.001$, *student's t*-test). Error bars in A and B represent standard error. $70 > N > 50$ cell from 10 to 15 seedlings for each measurement. **C**, Effect of CGA treatment (lower panel) on the shape of pavement cells in wildtype (left panel) and *pmei37* (right panel) compared to the control treatment (DMSO; upper panel). Scale bar = 10 µm.

Supplemental Figure 2.8

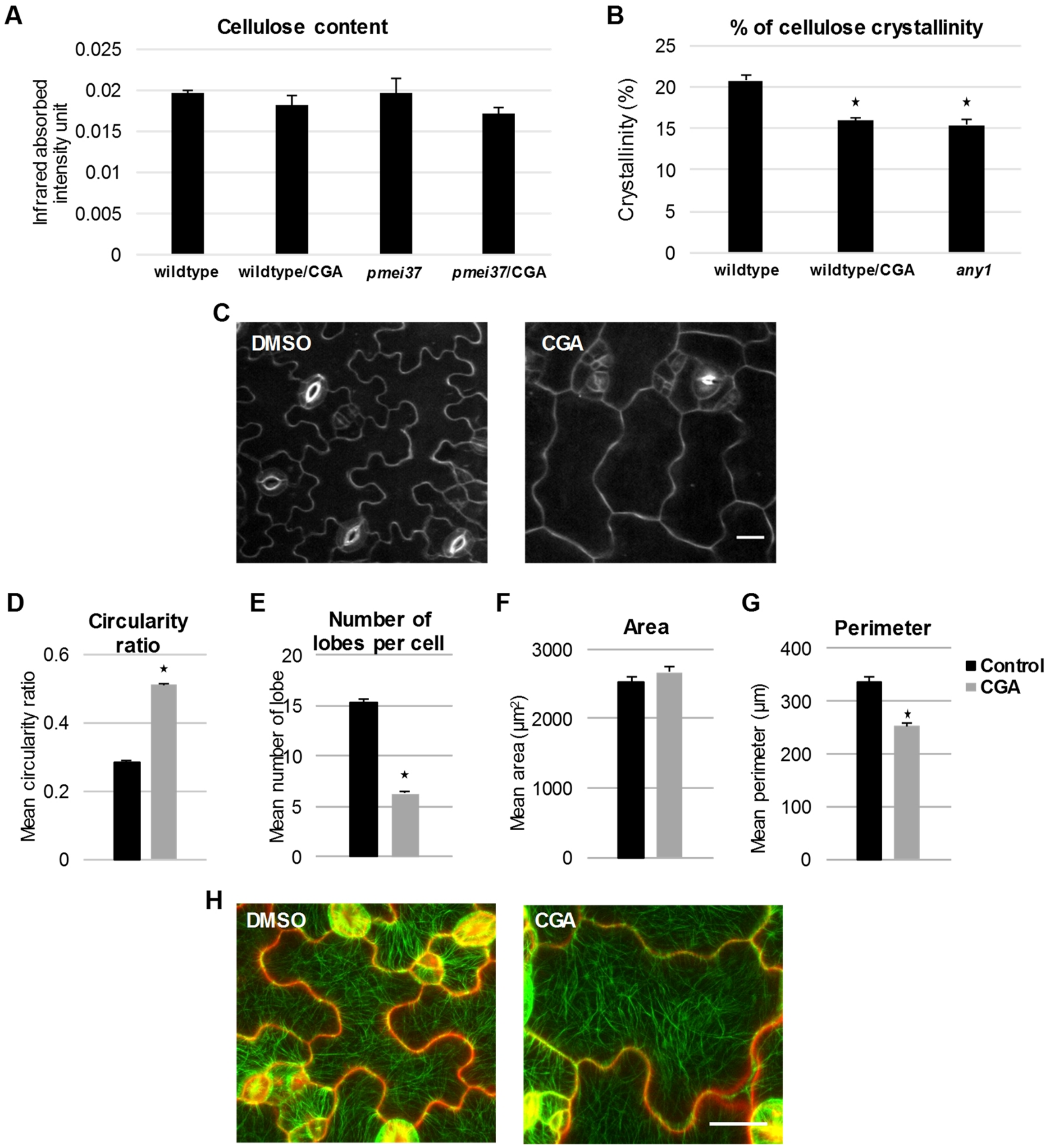

Supplemental Figure 2.8: Effect of CGA treatment on pavement cell shape and cellulose content.

A, Cellulose content in the wildtype and *pmei37* seedlings 4 days after germination under control and 0.9 nM CGA treatment determined using Attenuated Total Reflection spectroscopy. **B**, Degree of cellulose crystallinity in the cotyledons of wildtype seedlings 4 days after germination in presence of

DMSO (control) and 0.9 nM CGA and in *any1* mutant using X-ray diffractometer. Error bars in A and B represent the standard error. Asterisks indicate statistically significant differences compared to the wildtype ($P < 0.05$, *student's t*-test). Each bar represents data from 3 measurements, each measurement is a pool of 3 – 5 cotyledons. **C**, Fluorescence micrographs of pavement cells on the abaxial side of a cotyledon at 4 days after germination of wildtype grown in presence of DMSO (control) and 0.9 nM CGA (treatment), stained with propidium iodide. **D to G**, Mean circularity (D), number of true lobes per cell (E), cell area (F) and cell perimeter (G) at 4 days after germination of wildtype pavement cells treated with 0.9 nM CGA (gray bars) and control cells (treated with DMSO; black bars). Error bars represent the standard error. Asterisks indicate statistically significant differences ($P < 0.001$, *student's t*-test). N = 40 - 60 cell from 8 - 10 seedlings for each measurement in D-G. **H**, Fluorescence micrographs of GFP:TUB6 pavement cells show cortical microtubules (green color) and cell wall (red color, stained with propidium iodide) grown in presence of DMSO (control) and 0.9 nM CGA (treatment). Scale bars = 20 µm.

Supplemental Figure 2.9

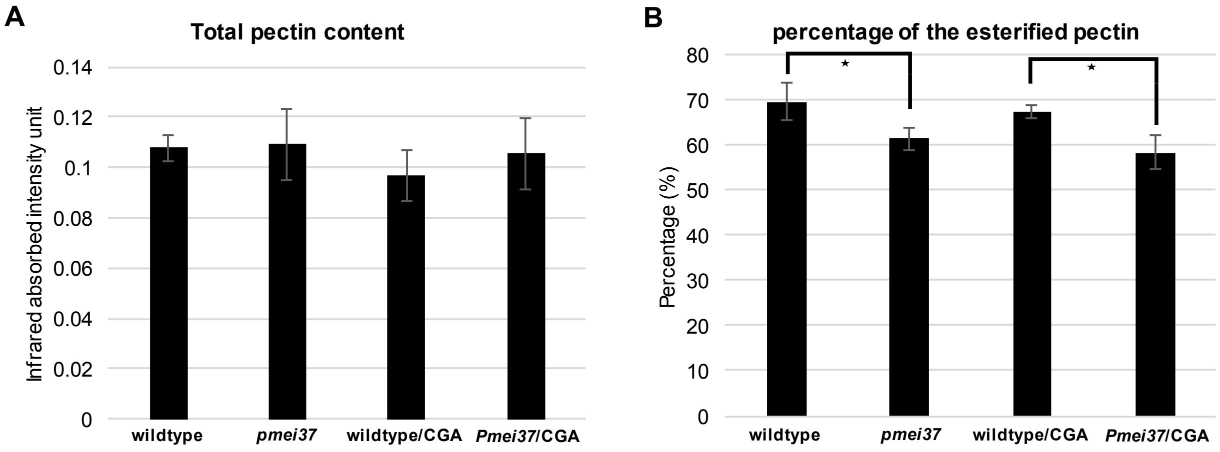

Supplemental Figure 2.9: Pectin content and percentage of esterified pectin in the in the wildtype and *pmei37* seedlings 4 days after germination under control and 0.9 nM CGA treatment obtained using Attenuated Total Reflection spectroscopy.

A, Total pectin content, **B**, percentage of esterified pectin. Asterisks indicate statistically significant differences ($0.01 < P < 0.05$, *student's t*-test). Error bars represent standard error. $4 < N < 7$ measurements, each measurement is a pool of 3 – 5 cotyledons.

Supplemental Figure 2.10

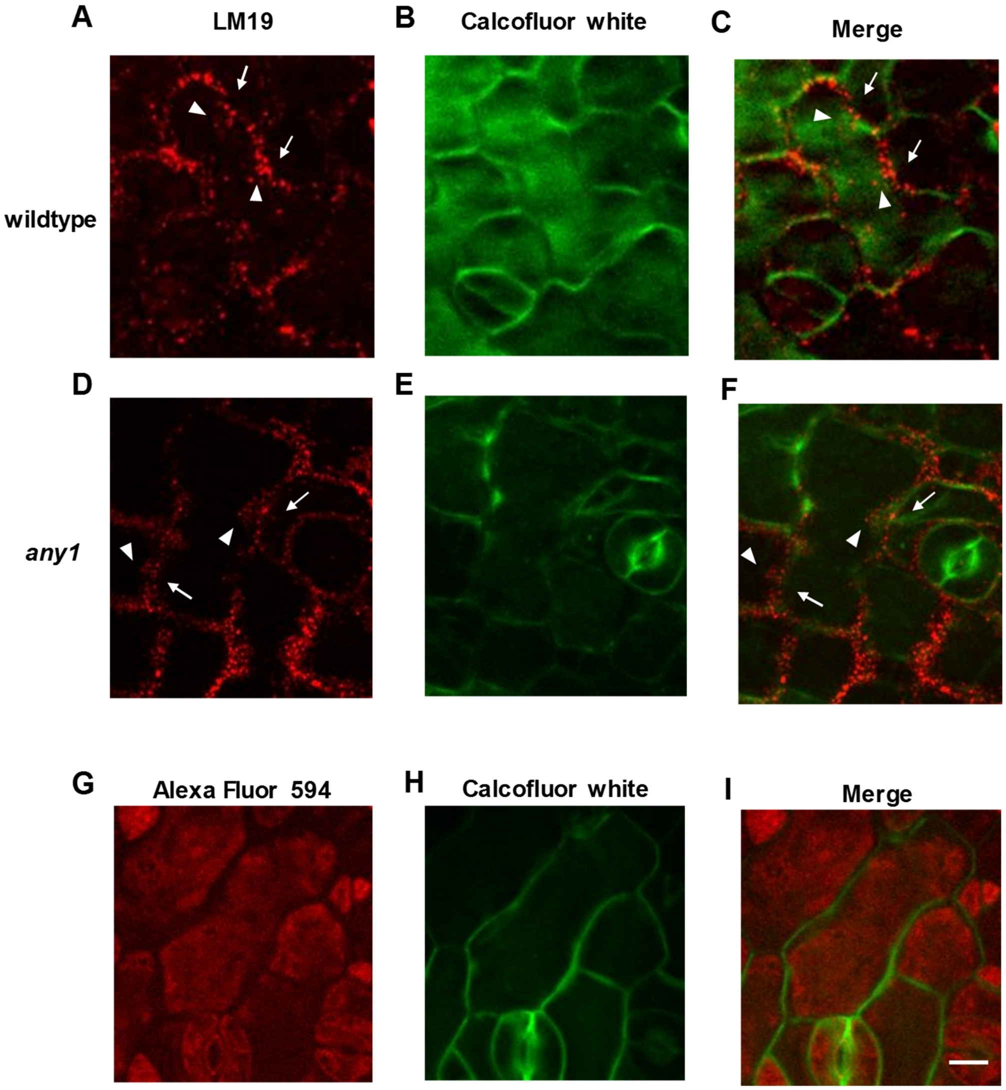

Supplemental Figure 2.10: Spatial arrangement of demethyl-esterified pectin in the pavement cells of wildtype and *any1* detected by monoclonal antibody (LM19).

A and D, Maximum projections of z-stack images of pavement cells labeled with LM19 for demethyl-esterified pectin. **B and E**, Calcofluor white label (presenting cell shape). **C and F**, Merge of the LM19 and the calcofluor white fluorescence micrographs of wildtype (A, B and C) and *any1* mutant (D, E and F). Arrowhead (neck region) and arrow (lobe region) indicate instances of high and low abundance of demethyl-esterified pectin at the neck and lobe regions, respectively. **G**, Maximum projections of z-stack of pavement cells stained only with Alexa Fluor 594, negative control for (A) and (D). **H**, Calcofluor white label (presenting cell shape in G). **I**, Merge of Alexa Flour 594 and the calcofluor white micrographs. Scale bar = 10 µm.

Supplemental Figure 2.11

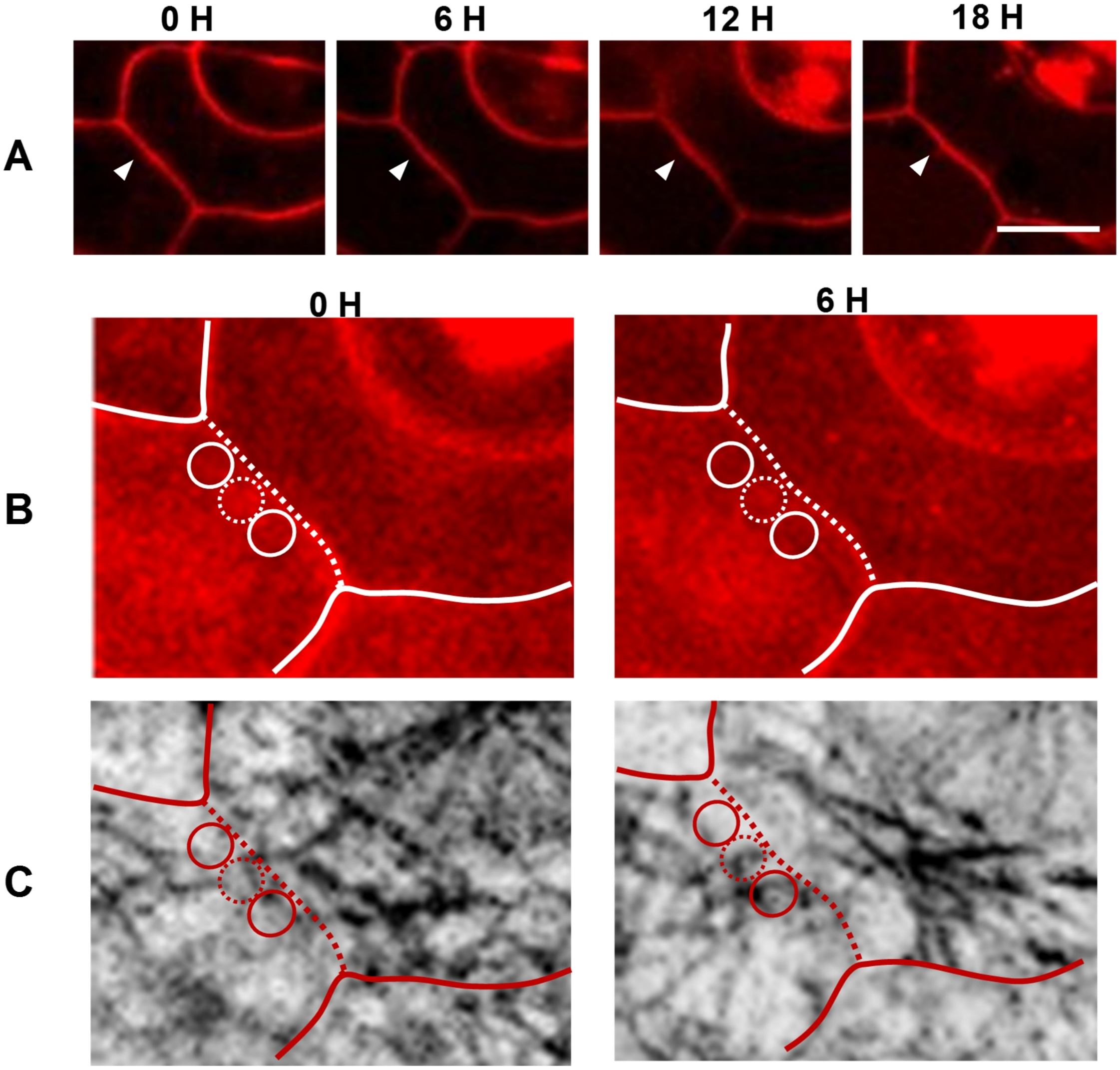

Supplemental Figure 2.11: Image analysis of pectin and microtubule dynamics during time lapse monitoring.

Fluorescence micrographs of wildtype pavement cells were monitored over 18 hours and visualized in 6 hour time-lapse intervals. To correlate the dynamics of demethyl-esterified pectin and cortical microtubules with developing cell border curvatures, the fluorescence intensity was measured at the future border undulation and compared with that in adjacent regions. **A**, Single optical sections showing the anticlinal wall stained with propidium iodide over time. Arrowheads indicate the location on the cell border monitored over time in B and C. The prospective curvature of the straight line at time 0 was selected based on the curvature at 18 H. **B and C**, Maximum projections of z-stacks of same sample as in A, at 0 and 6 hours, showing propidium iodide signal for demethyl-esterified pectin (B) and cortical microtubules at the periclinal wall (GFP:TUB6) (C). Dotted circles in B and C indicate tip of the prospective neck region (region of interest). Solid-line circles represent adjacent regions. The signal intensity of the dotted ROI was divided by the mean intensity signal of the two adjacent solid line ROIs in order to obtain the relative intensity difference. The dotted circles in (B) illustrate enrichment of pectin label at the prospective neck region before the curve appears (i.e. 0 time) compared to the solid-line circles at the same time point. In C, no difference in microtubule density between dotted and solid-line circles appears before the curvature (i.e. time 0), but at 6h the density of microtubules changes. White and red lines in B and C show the anticlinal wall that is shown in A. The dotted regions of the white and red lines in in B and C represents the anticlinal wall of interest. Scale bars = 10 µm.

3 Impact of pectin esterification and cellulose crystallinity on the elongation pattern of dark-grown hypocotyls of *Arabidopsis*

Individual cells of dark-grown hypocotyls experience a highly anisotropic expansion during the elongation process of the organ. How pectin esterification and cellulose crystallinity impact the anisotropic expansion and the biomechanical properties of the cell wall during the elongation of the dark-grown hypocotyl is investigated in this chapter. This chapter presents a manuscript in preparation for submission. The authors of this manuscript are:

Bara Altartouri[a], Amir J Bidhendi[b], Mohammad S Zamil[b], Youssef Chebli[b], Na Liu[c], Chithra Karunakaran[c], Anja Geitmann[ab]

[a] Département de sciences biologiques, Université de Montréal, Montréal, QC H1X2B2, Canada
[b] Department of Plant Science, McGill University, Sainte-Anne-de-Bellevue, QC H9X3V9, Canada
[c] Canadian Light Source, 44 Innovation Boulevard Saskatoon, SK S7N 2V3, Canada

I am responsible for all experimental design, data acquisition, processing and analysis, and discussion of the results. I am also responsible for writing the paper. Amir J Bidhendi and Mohammad S Zamil developed the tensile testing device and participated in the experimental design for mechanical measurements. For the FTIR experiment, I designed the experiment, Na Liu acquired the data, Youssef Chebli analyzed the data. Chithra Karunakaran and Anja Geitmann supervised this part of the work. Anja Geitmann supervised the research process and the experimental design and helped in the preparation of the manuscript with edits and advice on content.

Keywords: Cellulose microfibril, crystallinity, pectin, pectin methylesterase, cell expansion, cell wall mechanics, dark-grown hypocotyl, *Arabidopsis*.

3.1 Abstract

The expansion pattern of the cell wall determines cellular development and ultimately organ formation in the plant. For example, elongation of dark-grown hypocotyls is a result of a highly anisotropic expansion of the wall of each of the individual cells composing the organ. How biochemical and biomechanical properties of the cell wall regulate such anisotropic expansion warrants further investigation with the emergence of contradicting results regarding the role of homogalacturonan pectin. Here, we used genetic, biochemical and biomechanical approaches to study the impact of the esterification status of homogalacturonan pectin and cellulose crystallinity during the elongation of the dark-grown hypocotyl of *Arabidopsis thaliana*. We show that these polymers make distinct contributions in each developmental phase of hypocotyl elongation. An increase in the proportion of methyl-esterified pectin increases the elongation of the hypocotyl during the first developmental phase while a reduction in the cellulose crystallinity decreases the elongation of the hypocotyl at the second developmental phase. Our data also show a correlation between cellular expansion and cell wall stiffness during the first developmental phase of hypocotyl elongation. An increase in the proportion of methyl-esterified pectin and a reduction in cellulose crystallinity are characterized by a reduction in cell wall stiffness and an increase in cell wall expansion.

3.2 Introduction

Cellular proliferation and expansion are well regulated during organ growth in plants in order to ensure specific biological functions that define individual tissues. Cell proliferation increases the number of cells while cell expansion enlarges the individual cells. Cellular expansion occurs under tensile stress that is generated on the cell wall by the internal turgor pressure. As a result of the tensile stress, the existing wall polymers elastically stretch or plastically deform by sliding against each other and new cell wall material may be added (Refregier et al., 2004). This process allows enlargement of the cell and is controlled by wall-loosening agents and wall-mechanical properties. Both mechanisms play an important role in regulating the expansion pattern characterized by the rate and the directionality of the expansion

(Taiz, 1984; Carpita and Gibeaut, 1993; Geitmann and Ortega, 2009; Cosgrove, 2016, 2018, 2018). The impact of some of the wall polymers on the mechanical behavior of the cell wall has been addressed in previous studies. For example, reduction in the amount of cellulose microfibrils or homogalacturonan pectin reduces the wall stiffness in the hypocotyl of *Arabidopsis thaliana* (Ryden et al., 2003; Abasolo et al., 2009), whereas reduction in the linear pectic arabinan increases the stiffness of the inflorescent stem of *Arabidopsis* (Verhertbruggen et al., 2013). However, the correlation between the mechanical impact of the wall polymers and the expansion of the cell wall remains to be investigated.

During the expansion of dark-grown hypocotyls of *Arabidopsis*, several cell wall modifying enzymes are involved including pectin methylesterases (PMEs) (Pelletier et al., 2010). This family of enzymes and their inhibitors (pectin methylesterase inhibitors; PMEIs) regulate the esterification status of the homogalacturonan pectin in the wall. The ratio between the methyl-esterified to demethyl-esterified pectin in the cell wall is important during the elongation process (Derbyshire et al., 2007). Two different mechanisms are proposed to explain the role of the de-esterification of homogalacturonan pectin during cell wall expansion. These mechanisms differ depending on the de-esterification pattern; blockwise demethyl-esterification allows calcium cross-linking between the polymers whereas random demethyl-esterification may promote the degradation of the polymer (Palin and Geitmann, 2012; Levesque-Tremblay et al., 2015; Bidhendi and Geitmann, 2016; Hocq et al., 2017). The latter mechanism proposes that de-esterification activity decreases the extracellular pH which in turn activates the degradation process of demethyl-esterified pectin by the enzyme polygalacturonase resulting in wall loosening. This notion is supported by the observation that overexpression of *PME5* induces organ growth and reduces the stiffness of the shoot apical meristem in *Arabidopsis thaliana* (Peaucelle et al., 2011). Moreover, overexpression of *PMEI4* delays the elongation of dark-grown hypocotyls (Pelletier et al., 2010). On the other hand, the blockwise mechanism is based on the mechanical properties of methyl- and demethyl-esterified pectin and suggests different roles for these polymers during wall expansion. *In vitro* studies show that the esterification degree of homogalacturonan in a Ca^{2+}-pectin gel is correlated with the stiffness of the gel, with high stiffness resulting from the high degree of de-esterification as it is able to bind with calcium ions and form a rigid matrix (Ngouemazong et al., 2012). Consistent with this notion, methyl-esterified pectin coincides spatially with the soft and rapidly expanding regions of the cell wall in the pollen tube (Zerzour et al., 2009; Chebli et al., 2012). Moreover, it was observed that the methyl-esterified pectin is predominantly present in the fast-growing region of the inflorescence stem of *Arabidopsis* (Phyo et al., 2017). Conversely, demethyl-esterified pectin is correlated with a decrease in the expansion rate and an increase in the stiffness of the wall (Derbyshire et al., 2007; Guénin et al., 2011; Hongo et al., 2012; Bou Daher et al., 2018). Derbyshire et al. (2007) showed that an increase in the demethyl-esterified pectin in the dark-grown hypocotyl of *Arabidopsis* restricts its elongation. Overexpression of *PMEI3* and *PME5* genes causes a decrease and an increase in the stiffness of the wall of dark-grown hypocotyl cells, respectively (Bou Daher et al., 2018). These results are difficult to reconcile with the results reported by Peaucelle et al. (2015), thus necessitating further investigation of the role of esterified pectin on the expansion and the mechanical properties of the cell wall in dark-grown hypocotyls.

The elongation of dark-grown hypocotyls is a result of anisotropic expansion of the individual cells. Anisotropic expansion of the epidermal layer of dark-grown hypocotyls is suggested to be controlled by a regulated spatial distribution of homogalacturonan pectin (i.e. methyl- and demethyl-esterified pectin) and the orientation of cellulose microfibrils (Peaucelle et al., 2015; Bou Daher et al., 2018). At the early expansion phase, while cells still have a largely cubic shape, the difference in the spatial distribution between methyl- and demethyl-esterified pectin at the anticlinal walls can initiate anisotropic expansion. At this phase, the orientation of cellulose microfibrils is suggested to be random as inferred from the observation of the cortical microtubules. At the next phase of the expansion, cellulose microfibrils orient perpendicular to the long axis of the hypocotyl in the inner wall (Crowell et al., 2011). Such orientation promotes further anisotropic expansion perpendicular to the direction of cellulose microfibrils (Baskin, 2005). The role of cellulose in these models is based on the concept that random and parallel orientation of the microfibrils leads to isotropic and anisotropic expansion, respectively (Verbelen et al., 2001; Baskin, 2005; Chan, 2012). However, certain mutants with a swelling phenotype (isotropically expanding) do not show a random orientation of cellulose microfibrils suggesting an involvement not only of the orientation but also of other physical properties of cellulose microfibrils (Sugimoto et al., 2003; Fujita et al., 2011). Cellulose microfibrils occur in crystalline and non-crystalline forms in the primary cell wall with a higher abundance of the latter. Crystallinity is believed to confer elevated tensile strength to the microfibrils (Eichhorn and Young, 2001). Whether crystallinity of the cellulose plays a role during the expansion steps of the dark-grown hypocotyl cells has not been addressed in detail.

Here, we investigate the influence of the esterification status of homogalacturonan pectin and the reduction in the cellulose crystallinity on the expansion pattern and the mechanical properties of dark-grown hypocotyls of *Arabidopsis thaliana*. We used wildtype and the *anisotropy1* (*any1*) mutant, which is characterized by a significant reduction in cellulose crystallinity without a reduction in overall cellulose content (Fujita et al., 2013). Moreover, we used *pme* mutants (*pme3* and *pme44*) that are expressed in the hypocotyl during its elongation period (Pelletier et al., 2010; Guénin et al., 2011; Guénin et al., 2017).

3.3 Results

3.3.1 Methyl-esterified pectin accelerates anisotropic expansion at the early phases of hypocotyl elongation while cellulose crystallinity has a major impact during the later phases of the expansion

We investigated the elongation pattern of hypocotyls during the first 6 days of germination in dark-growth conditions in the wildtype of *Arabidopsis thaliana* and compared it with the *pme3*, *pme44*, and *any1* mutants. In addition, we investigated the expansion pattern of individual epidermal cells at the mid-region of the hypocotyl (Fig. 3.1A).

The elongation pattern of the wildtype hypocotyl over the first 4 days of elongation was characterized by a slow elongation phase followed by a rapid elongation phase which is consistent with previously reported results (Fig. 3.1B) (Refregier et al., 2004; Peaucelle et al., 2015). At five and six days after germination, wildtype hypocotyl elongation slowed again. The elongation patterns of the *pme3* and *pme44* mutants were similar and hypocotyl length of these mutants at the sixth day of elongation was similar to the wildtype (Fig. 3.1B; Fig. 3.2A).

However, the main difference in the elongation pattern between the wildtype and the *pme3* and *pme44* hypocotyls occurred during the first two days (first phase) of elongation. During this phase, the elongation rates of *pme3* and *pme44* hypocotyls were substantially higher than that of the wildtype. Our measurements started at seed germination (0 hour) rather than seed imbibition to avoid any differences generated by different germination times that might occur between the wildtype and the mutants. At two days after germination, the hypocotyl lengths of the *pme3* and *pme44* mutants were about two times the length of the wildtype hypocotyl ($P < 0.001$, *student t*-test) (Fig. 3.1B; Fig. 3.2A). The diameters of the hypocotyl did not change significantly during the 6 day observation period in wildtype or mutants (Figs. 3.1D,H). The acceleration and the increase in the length of the hypocotyl were correlated with the axial anisotropic expansion of the hypocotyl epidermal cells (Fig. 3.1C; Fig. 3.2B). Epidermal cell area and perimeter increased significantly during the developmental phases in the wildtype and *pme3* and *pme44* mutants (Figs. 3.1E,F). The increase in the area and the perimeter were mainly a result of cell elongation and involved only a minor increase in cell width (Fig. 3.1G). Given the substantial differences between the growth patterns of the *pme* mutants and the wildtype, these results indicate that methyl-esterified pectin accelerates elongation rate and anisotropic expansion at the early phases of hypocotyl elongation.

In the *any1* mutant, the elongation of the hypocotyl after six days of germination was significantly reduced compared to the wildtype. During the first two days of elongation, the width both of the hypocotyls and the individual epidermal cells in the *any1* mutant were significantly higher compared to the wildtype (Figs. 3.1D,G,H). However, during this early phase, there was no significant difference in the length of the hypocotyl nor the length of the epidermal cells between the *any1* mutant and the wildtype (Figs. 3.1B,C; Fig. 3.2B). These results show that while cell width in the *any1* was higher than the wildtype during the first phase, the effect of cellulose crystallinity on hypocotyl length is apparent only during the second phase of the expansion.

To further examine the involvement of methyl-esterified pectin during the anisotropic expansion at the early phases of dark-grown hypocotyl cells, we reduced cellulose crystallinity in the wildtype and *pme3* and *pme44* mutants by growing the seedlings in the presence of CGA

325’615 (CGA) and monitored the elongation rate of the hypocotyls. CGA reduces significantly the crystallinity ratio and increases the relative abundance of non-crystalline cellulose (Peng et al., 2001). CGA treatment had a more pronounced effect on hypocotyl length during the second phase than the first phase of elongation when comparing wildtype treated CGA with *any1* mutant (Fig. 3.1B; Fig. 3.3A). This difference may occur because of the prolonged treatment with CGA. Therefore, we focused on the first phase of elongation. As a result of CGA treatment, cell width, perimeter and cell area in the wildtype, *pme3* and *pme44* mutants were increased during the hypocotyl elongation (Figs. 3.3C-E). Hypocotyl length of treated wildtype, *pme3* and *pme44* was similar after six days of germination. However, at two days of germination, hypocotyls of *pme3* and *pme44* mutants were about 45 percent longer than the wildtype (Fig. 3.3A). This increase correlated with an increased length of the individual epidermal cells (Fig. 3.3B). To summarize, these observations suggest that methyl-esterified pectin accelerates the anisotropic expansion during the early phases of the elongation and the involvement of cellulose crystallinity occurs mainly during the second phase of the elongation.

3.3.2 Level of methyl-esterified pectin is increased at the early phases of hypocotyl elongation in the *pme3* and *pme44* mutants

The difference in the hypocotyl length between the *pme* mutants and the wildtype and *any1* mutant at the early phases of the elongation suggests a difference in the cell wall components. We, therefore, used ATR-FTIR (Attenuated total reflection – Fourier transform infrared spectroscopy) (Lahlali et al., 2014; Lee et al., 2017; Canteri et al., 2019) to quantitatively assess the content of pectin, homogalacturonan pectin and its esterification status and cellulose at two different developmental phases: i) at 2 days after germination (DAG), when hypocotyl length in the wildtype and *any1* is similar and significantly lower than that of the *pme3* and *pme44* mutants (Figs. 3.1B,C) and ii) at 5 DAG, when wildtype, *pme3,* and *pme44* have similar hypocotyl length that is higher than that of the *any1* hypocotyl (Figs. 3.1B,C).

The content of homogalacturonan pectin in *pme3* and *pme44* was not different from that in the wildtype and *any1* mutant at 2 DAG. It was reduced significantly during the subsequent elongation process in the wildtype, *pme3* and *pme44*, but not in the *any1* mutant (Fig. 3.4A).

Although the content of homogalacturonan pectin at 2 DAG was similar in the wildtype, *pme3* and *pme44*, the degree of the methyl-esterification was different. At that time point, the relative abundance of methyl-esterified pectin in *pme3* and *pme44* was significantly higher than that of the wildtype and *any1*. At 5 DAG, the level of methyl-esterified pectin was reduced in the *pme3* and *pme44* mutants compared to the 2 DAG time point and they reached the same level as those in the wildtype and *any1* hypocotyls at that time point (Fig. 3.4B). It is worth noting that the content of total pectin was not altered in the *pme* mutants compared to the wildtype and *any1* at all phases (Fig. 3.4C). On the other hand, the change in cellulose crystallinity (i.e. *any1* hypocotyl) did not affect significantly the cellulose content compared to the wildtype and *pme* mutants at 2 DAG. However, there was a reduction in the cellulose content of the *any1* hypocotyl at 5 DAG compared to wildtype of the same phase (Fig. 3.4D). These data suggest that the increase in hypocotyl elongation of *pme3* and *pme44* at the early phases is due to the elevated amount of the methyl-esterified pectin in their cell walls.

3.3.3 Cell wall density is elevated at the early phases of the dark-grown hypocotyl in the *pme3* and *pme44* mutants

We speculated that changes in the cell wall composition between the wildtype and *pme* mutants might affect the density of the polymer per wall section area. Such changes may alter the mechanical properties of a given wall segment and this possibility is addressed in the following section of the results. To be able to characterize the material properties, we had to first determine the density of the wildtype, *pme3*, *pme44,* and *any1* hypocotyls at 2 and 5 DAG by calculating the ratio of dry weight to wet volume of the dark-grown hypocotyl. At 2 DAG, the densities of the *pme3* and *pme44* hypocotyls were significantly higher than in the wildtype and the *any1* hypocotyls ($P < 0.05$, *student t*-test). At 5 DAG, the densities of the hypocotyls in the wildtype and all mutants was reduced compared to the respective values at the 2 DAG time point. This reduction was significant in the *pme3*, *pme44,* and *any1* ($P < 0.01$, *paired t*-test). However, the difference in the density between wildtype and all mutants at 5 DAG was diminished (Fig. 3.5). The density of the wildtype hypocotyl at 5 DAG is in agreement with the density at the same developmental phase reported earlier by Saxe et al. (2016).

3.3.4 Reduced cell wall stiffness is associated with increased cell wall expansion at the early developmental phase of the dark-grown hypocotyl

The variation in the expansion between the wildtype, *pme3*, *pme44*, and *any1* suggests differences in the mechanical properties of the cell walls. We therefore wanted to examine the mechanical properties of the hypocotyl that corresponds to this variation. We used tensile testing to examine the stiffness and the fracture strain of the hypocotyls and we used a cyclic test to determine the elastic/plastic behavior of the cell wall.

In order to determine the stiffness of the cell wall material in the wildtype, *pme3*, *pme44,* and *any1* hypocotyl, we used a specific modulus instead of the apparent Young’s modulus. The apparent Young’s modulus reflects the stiffness of the hypocotyl tissue regardless of the density of the cell wall material (Figs. 3.6A,B). The specific modulus (stiffness hereafter), on the other hand, reflects the Young's modulus per mass density of the cell wall. The reliability of our device for determining the stress-strain curve of the cell wall was confirmed by performing a mechanical tensile test on turgid and plasmolyzed hypocotyls. The apparent Young’s moduli of turgid hypocotyls were significantly higher than those of plasmolyzed hypocotyls (Figs. 3.6A,B). This is in agreement with most documented studies of turgid and plasmolyzed plant tissue as the loss of turgor lets the cell wall material relax (Cosgrove, 2016). At 2 DAG, the hypocotyl stiffness in the wildtype was significantly higher than that of the *pme* mutants ($P < 0.05$, *student t*-test) (Fig. 3.6C). This difference was diminished at 5 DAG as the values for the mutants increased relative to the earlier time point (Fig. 3.6D). On the other hand, the stiffness of *any1* mutant hypocotyls was significantly lower than that of wildtype hypocotyls at both phases ($P < 0.001$, *student t*-test) (Figs. 3.6C,D). In all samples, wildtype, *pme3*, *pme44*, and *any1* hypocotyls, the stiffness values at the later developmental phases were higher than those in the corresponding samples at earlier phases. This might be because of an increase in the amount cell wall material per cross section and/or an increase in the ratio of the cellulose crystallinity.

The response of the cell wall to the force that is generated by the turgor pressure inside the cell depends on the composition and conformation of the wall polymers. Wall polymers respond to an external force by an elastic deformation that may include their rotation and straightening or by a permanent deformation (plastic). Plastic deformation occurs when the applied force exceeds the capacity of the elastic deformation and causes breakage of inter- and intra-molecular bonds, such as hydrogen bonds, that allows sliding of the polymers against each other. We, therefore, wanted to determine the elastic-plastic portion of the cell wall in the wildtype, *pme3*, *pme44*, and *any1* hypocotyls at 2 DAG by using cyclic loading and unloading experiment. The plastic component of the cell wall behavior in the wildtype hypocotyl is about 38 percent. This percentage of plasticity is the same in *pme3* and *pme44*. However, the reduction in the crystallinity of cellulose in the *any1* was associated with a significant increase in plasticity (Figs. 3.7A-C). Moreover, it correlated with a significant increase in the fracture strain and decrease in fracture stress compared to the wildtype. A reduction in the demethyl-esterified pectin in *pme3* and *pme44* hypocotyl on the other hand did not change significantly fracture stress or strain compared to the wildtype (Fig. 3.7D).

3.4 Discussion

Dark-grown hypocotyls feature two distinct elongation phases with a slow phase preceding a more rapid one (Refregier et al., 2004). In this study, we examined the impact of the esterification status of homogalacturonan pectin and the crystallinity of cellulose on the regulation of these developmental phases and the mechanical properties of dark-grown hypocotyls. The effect of the esterification status of homogalacturonan pectin and the crystallinity of cellulose become apparent at different elongation phases. A reduction in the proportion of demethyl-esterified pectin increases the elongation and the anisotropic expansion of the cells and decreases the stiffness of the cell wall during the first phase of the elongation. Reduction in the degree of cellulose crystallinity, on the other hand, acts predominantly during the second elongation phase reducing cell elongation and anisotropic expansion.

Cellulose microfibrils are the mechanically dominant feature that provides strength to the cell walls of dark-grown hypocotyls. Consistent with this concept, a reduction in the total content of cellulose by applying cellulose inhibitor, 2,6-dichlorobenzonitrile (DCB) significantly reduces the stiffness of the hypocotyl (Ryden et al., 2003). The mechanical strength conferred by cellulose is believed to be associated predominantly with the crystalline component (Eichhorn and Young, 2001; Quesada Cabrera et al., 2011). Here we were able to test exclusively the effect of cellulose crystallinity on the anisotropic expansion without a significant change in either the total content of cellulose (shown here) nor the orientation of the microfibrils, as reported previously by Fujita et al. (2013). Our results show that the involvement of cellulose crystallinity in the anisotropic expansion of the cell is distinct between the first and the second developmental phase. At the first phase of the elongation, hypocotyls with reduced cellulose crystallinity (i.e. *any1* mutant) were still able to elongate and the epidermal cells expanded and reached the same length as the wildtype epidermal cells. However, cell expansion in the *any1* mutant was less anisotropic during this phase as the reduction in cellulose crystallinity allowed a significant increase in cell width of the cell compared to the wildtype. At the second phase of the elongation, *any1* hypocotyls were not able to elongate as rapidly as wildtype hypocotyls. These results suggest that the role of cellulose crystallinity serves to provide prominent mechanical support during the second phase of elongation and to prevent growth in width during the first phase. We suspect that the first phase of the anisotropic expansion might be regulated by the esterification status of the homogalacturonan pectin and consistent with this, a decrease in the proportion of demethyl-esterified pectin in the *pme3* and *pme44* cell wall altered the anisotropic expansion during the early developmental phase. This result was confirmed further by growing *pme3* and *pme44* mutants in the presence of the herbicide CGA. In the presence of the herbicide, the expansion of *pme3* and *pme44* hypocotyls was only altered during the first phase compared to the wildtype that was grown in the same condition.

The increased cell elongation in *pme3* and *pme44* relative to the wildtype is associated with a decrease in the proportion of demethyl-esterified pectin. We suspected this increase in cell expansion to be a result of wall softening as shown by Bou Daher et al. (2018) rather than wall stiffening as reported by Peaucelle et al. (2015). Our mechanical testing data confirm that the wall stiffness in *pme3* and *pme44* was significantly reduced. The reduced hypocotyl stiffness in *pme3* and *pme44* reflects the stiffness of the cell wall rather than an alteration or reduction in cell adhesion since neither total homogalacturonan content (measured by ATR-FTIR) nor the apparent Young's modulus (measured by tensile test) was significantly reduced in these mutants compared to the wildtype (Krupkova et al., 2007; Mouille et al., 2007). Our results suggest that the de-esterification of the homogalacturonan pectin during the first developmental phase of dark-grown hypocotyls probably occurs in a blockwise manner thus enabling calcium gelation and, in turn, restricting the elongation of the hypocotyls. This is in agreement with previously reported results regarding the effect of the esterification status of homogalacturonan pectin on the elongation of the hypocotyl (Derbyshire et al., 2007; Guénin et al., 2011; Hongo et al., 2012). However, it is opposite to the results reported by (Pelletier et al., 2010).

Reduced stiffness in the *pme3*, *pme44* and *any1* cell wall was correlated with increased expansion of the epidermal cells at 2 DAG, but the cellular expansion patterns differed between the mutants. *any1* epidermal cells underwent isotropic expansion, whereas epidermal cells of *pme3* and *pme44* mutants experienced anisotropic expansion. The anisotropic expansion of the *pme* mutants may arise from the spatial regulation of the de-esterification process (Peaucelle et al., 2015; Bou Daher et al., 2018). Methyl-esterified pectin is more abundant at the long side wall while demethyl-esterified pectin is more abundant at the short side wall (Bou Daher et al., 2018). Such spatial regulation promotes anisotropic expansion at early phases. On the other hand, the more isotropic expansion in the *any1* cells results from the overall reduction in cellulose crystallinity which is probably not confined to specific subcellular regions. The esterification status of the homogalacturonan pectin and its spatial arrangement play an important role during the early phase of the anisotropic expansion but may not be the only player. The stress that is generated from the overall shape of the hypocotyl and from the expansion of the inner tissue layers may play a role as well during the first phase of the epidermal cell expansion and elongation (Baskin and Jensen, 2013).

3.5 Materials and Methods

3.5.1 Plant material and growth conditions

Arabidopsis (*Arabidopsis thaliana*) wildtype (ecotype Columbia-0), *pme3* (AT3G14310; CS2103492) and *pme44* (AT4G33220; CS837906) were obtained from the Arabidopsis Biological Resource Center. *any1* mutant seeds were obtained from the lab of Dr. Geoffrey Wasteneys (University of British Columbia, Canada) (Fujita et al., 2013). PCR on genomic DNA was performed to confirm the heterogeneity of the T-DNA insertions with the following LP/RP primer pairs; 5'-AATTGGTTGAATGACGAAACG-3' and 5'-TACGTACCTGCCCCTTCAAC-3' for *pme3* and 5'-AGCAACCAGTTTCACAAACG-3' and 5'-CTTTTGTACCAGCGAAACCC-3' for *pme44*.

Seeds were sterilized and imbibed and kept at 4°C in the dark condition for 48 - 72 hours. Seeds were grown in plates containing half-strength Murashige and Skoog salt (MS; Fisher Scientific - cat# ICN2623220), 1% (w/v) sucrose and 0.8% (w/v) plant agar (Sigma-Aldrich – cat# A1296). For all dark-grown hypocotyl experiments, seeds were germinated in Petri-dishes at 22°C under an 8/16-h dark/light cycle until the first sign of germination occurred. Then Petri-dishes were wrapped with aluminum foil and kept vertically in *in vitro* growth chamber. For the same experiment, all genotypes were grown in the same petri-dish. In each petri-dish and for each genotype, 30 – 40 seedlings were presented.

3.5.2 Drug treatment

CGA (CGA 325'615, 1-cyclohexyl-5-(2,3,4,5,6-pentafluorophenoxy)-1λ4,2,4,6-thiatriazin-3-amine; (Syngenta - Basel, Switzerland)) was used to reduce cellulose crystallinity. 0.9 nM was the working concentration prepared from a 10 μM stock solution dissolved in DMSO (Sigma-Aldrich, cat# D8418). For the control experiment, the same volume of DMSO (v/v) was used. Seedlings were grown in a solidified 0.5x MS medium in the presence of the drug.

3.5.3 Measurement of the content of cellulose, homogalacturonan pectin and percentage of the methyl-esterified pectin

Mid-region of hypocotyls of dark-grown seedlings (2 and 5 days after germination) of wildtype, *pme3*, *pme44* and *any1* mutants were cut and fixed in 100% methanol for 3 - 4 hours. Methanol was substituted with 100% ethanol and samples were critical point dried using a Leica EM CPD300. The epidermal surface composition of the dark-grown hypocotyl was analyzed using ATR-FTIR at the mid-infrared beamline at the Canadian Light Source synchrotron (Lahlali et al., 2014; Lee et al., 2017). The globar source was employed as the infrared source. This ATR method used a germanium crystal (angle of incidence of 45°) attached to an Agilent Cary 600 Series FTIR spectrometer. Each infrared spectrum was recorded in the mid-infrared range of 4000 – 800 cm^{-1} wavenumbers at a spectral resolution of 4 cm^{-1}.

The data were analyzed with Orange 3.14. The data were corrected by performing a baseline correction (Rubber band) and by subtracting the background. The data were then normalized using the vector normalization algorithm and a Gaussian smoothing of 7 points was applied. The corrected data were transformed into the second derivative form by using the Savitzky–Golay algorithm. The estimation of components was determined by integrating the area between the baseline and specific bands, for cellulose (1145 - 1173 cm^{-1}), pectin (1404 – 1465 cm^{-1}), demethyl-esterified pectin (1590 - 1675 cm^{-1}) and methyl-esterified pectin (1722 – 1760 cm^{-1}). The total content of the homogalacturonan pectin is the sum of methyl- and demethyl-esterified pectins. The percentage of the methyl-esterified pectin equals the amount of methyl-esterified pectin / the amount of homogalacturonan pectin *100%.

3.5.4 Determination of mechanical properties of dark-grown hypocotyls

Dark-grown *Arabidopsis* hypocotyls (2 and 5 days after germination) of wildtype, *pme3*, *pme44* and *any1* mutants were either used fresh or plasmolyzed with 0.8 M mannitol (Sigma-Aldrich, cat# M9647) for 20 minutes. The mid-region of the dark-grown hypocotyl was mounted on a custom-built tensile device between two gripping ends; one is fixed and the position of the other one is controlled by a linear motorized stage (Thorlabs). The distance between the two gripping ends is adjustable to fit the sample size. In general, two distances were used; 1.5 mm and 4 mm for samples of 2 DAG and 5 DAG, respectively. A drop of deionized water (for the turgid experiment) or 0.8 M mannitol solution (for plasmolyzed hypocotyls) was added to the mounted samples to keep it moisturized during the experiment. A micro load cell sensor was attached to the movable gripping end. This sensor measure forces up to 5 gf (0.049 N) with a resolution of 10 µgf (0.098 µN). The sensor was calibrated against a series of known weights each time that the device was reconfigured. A linear variable displacement transducer (LVDT) with micrometer resolution was used to measure the displacement of the movable grip. The displacement speed was 40 µm for all experiments. The force-displacement data were collected at the PC and registered using a custom Python code and were used to generate the stress-strain curves. The custom-built tensile device was used under a Zeiss Discovery V8 stereomicroscope, 0.63x and 8x zoom, to allow measuring the diameter of each sample that was used to calculate the area of the hypocotyl cross-section. The apparent Young's modulus was calculated from the slope in the elastic range of the stress-strain curve. Fracture stress and strain were obtained from the stress-strain curve.

For the cyclic loading and unloading experiment, 6 cycles were performed. For the first cycle, samples were stretched by 2.5% of the original length. For the following cycles, samples were stretched an additional 2.5% to the previous cycle. The speed of the loading and unloading cycles was 40 µm/s. The plastic-elastic portion of the cell wall was calculated from the first cycle.

3.5.5 Density measurement

Sections of identical length were cut from hypocotyls of wildtype, *pme3*, *pme44* and *any1* mutant. The diameter of the hypocotyls was measured under a Zeiss Discovery V8 stereomicroscope, 0.63x and 8x zoom. 4 – 5 pools of hypocotyls were prepared; each pool contained 40 – 50 hypocotyls. Each pool of hypocotyls was air dried at room temperature for two days. Then, the weight of each pool was recorded using a 0.1 mg microbalance. The density was calculated as dried mass divided by the volume of the hydrated hypocotyl.

3.5.6 Cross sections

Dark-grown hypocotyls (2 days after germination) were fixed with freshly prepared 3.5% formaldehyde in phosphate buffered saline (PBS; 135 mM NaCl, 6.5 mM Na_2HPO_4, 2.7 mM KCl, 1.5 mM KH_2PO_4, pH 7.3). This was followed with three-time washes with PBS buffer. Then, samples were dehydrated with 20%, 50%, 70%, 80%, 90% ethanol 3 hours for each step and kept in 95% ethanol overnight following incubation in 100% ethanol with three changes. LR White (soft grade) were used to infiltrate the samples gradually; 33%, 66% each for 3 hours and then 100% LR White overnight. After that, samples were mounted in molds and the LR white was polymerized in an oven at 65°C for 48 hours. The cross sections with a thickness of 1 μm were obtained using a Leica Ultracut UCT.

3.5.7 Microscopy, image acquisition, and image analysis

For cell shape analysis a Zeiss spinning disk Axio Observer Z1 system was used. The 560-nm laser was used with an emission filter 590-625 nm to visualize the cell wall that is labeled with 0.01 mg/ml propidium iodide (PI; Sigma-Aldrich, cat# P4170) for 20 minutes. A 10x objective lens (NA = 0.45) was used for cell shape measurements. For visualizing hypocotyl cross sections, a Zeiss AxioImager Z1 was used. Sections were stained with 0.1% toluidine blue for 10 minutes then washed three times with distilled water before visualization. Brightfield optics with a 20x objective lens (NA = 0.5) was used to visualize the cross-sections. To visualize the length and the width of the hypocotyls, a Zeiss Discovery V8 stereomicroscope was used.

ImageJ software (http://imagej.nih.gov/ij) was used for measuring hypocotyl length, width and for cell shape analysis. Maximum projections of z-stack images were used for the analysis. Cell outlines were traced manually. Area and perimeter were determined automatically for each cell by the ImageJ software. We used the fit ellipse function in ImageJ to determine the length (major axis of the ellipse) and the width (minor axis of the ellipse) of epidermal cells. Data of the cell shape analysis at days 1, 2, 3, and 4 after germination were taken from different seedlings. Data of the hypocotyl length at days 1 to 6 after germination were taken from the same seedlings.

3.6 Figures

Figure 3.1

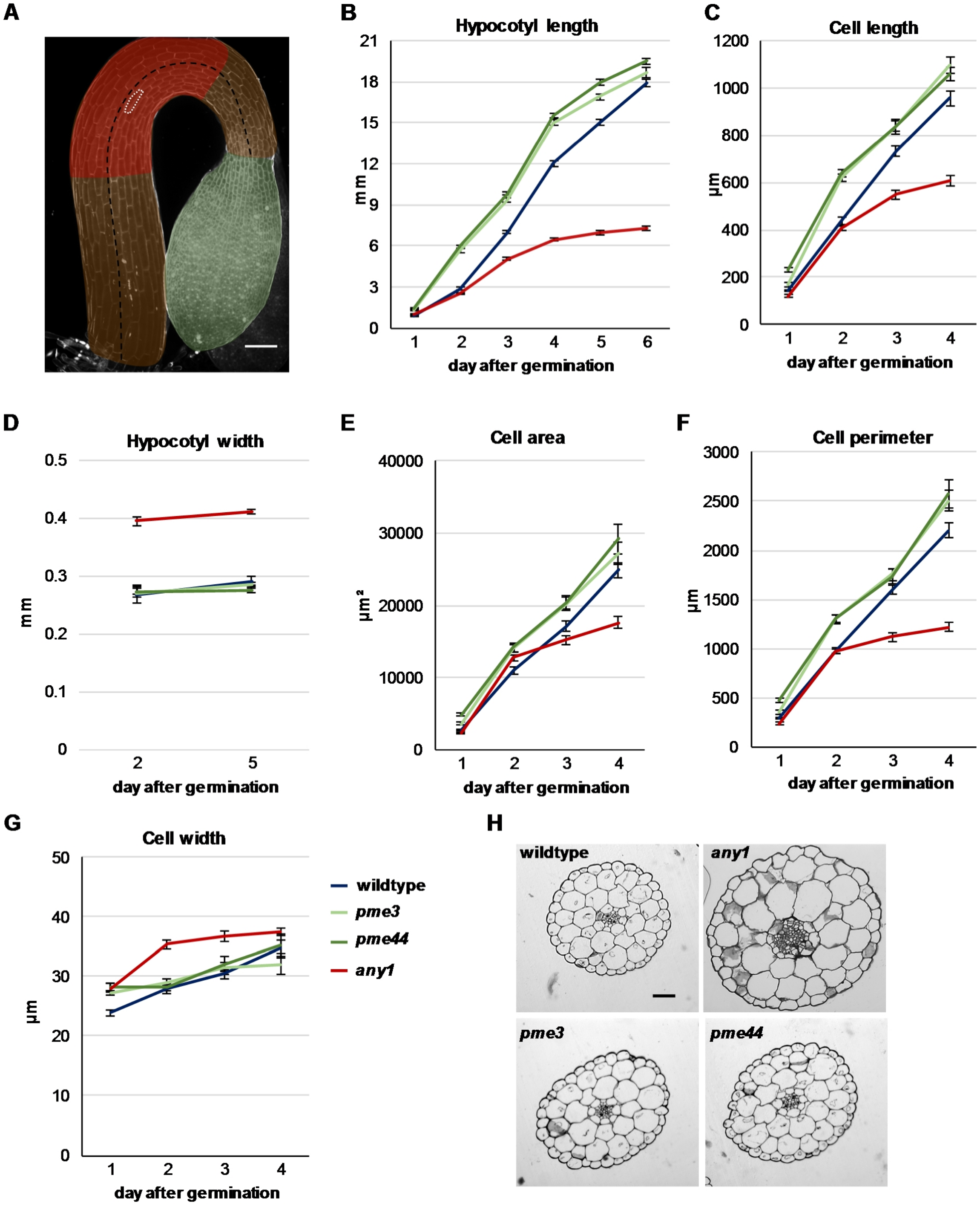

Figure 3.1: Elongation of dark-grown hypocotyls and hypocotyl epidermal cells of *Arabidopsis* wildtype, *pme3*, *pme44* and *any1* mutants.

A, wildtype seedling 20 hours after germination illustrating an example of hypocotyl length (dashed black line), a region of interest for epidermal cell measurements (shaded red region) and epidermal cell outline (dashed white line). In the micrograph, shaded brown and shaded green regions indicate hypocotyl and cotyledon of the seedling, respectively. Scale bar = 100 µm. **B and C**, length of the hypocotyl (B) and hypocotyl epidermal cells (C) for seedling grown in controlled condition. **D**, width of hypocotyls at 2 and 5 days after germination. **E - G**, cell area (E), cell perimeter (F) and cell width (G). Error bars represent the standard error. 50 - 60 dark-grown hypocotyls for each time point and 40 – 50 epidermal cells from 6 to 8 seedlings for each measurement. H, cross sections of wildtype, *any1*, *pme3* and *pme44* hypocotyls at 2 DAG. Scale bar = 50 µm.

Figure 3.2

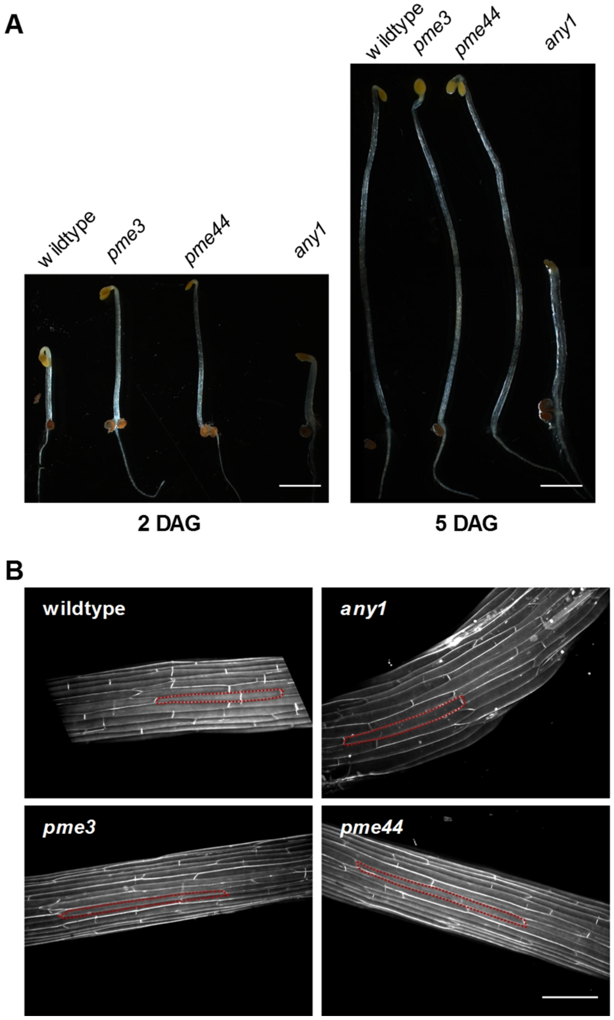

Figure 3.2: Micrographs of dark-grown hypocotyls of *Arabidopsis* wildtype, *pme3*, *pme44* and *any1*.

A, Micrographs illustrate hypocotyl lengths at 2 and 5 DAG. Scale bars = 2 mm. **B**, Fluorescence micrographs of dark-grown epidermal hypocotyl cells labeled with propidium iodide at 2 DAG. In the micrographs, the dashed lines indicate examples of cell outlines. Scale bar = 200 μm.

Figure 3.3

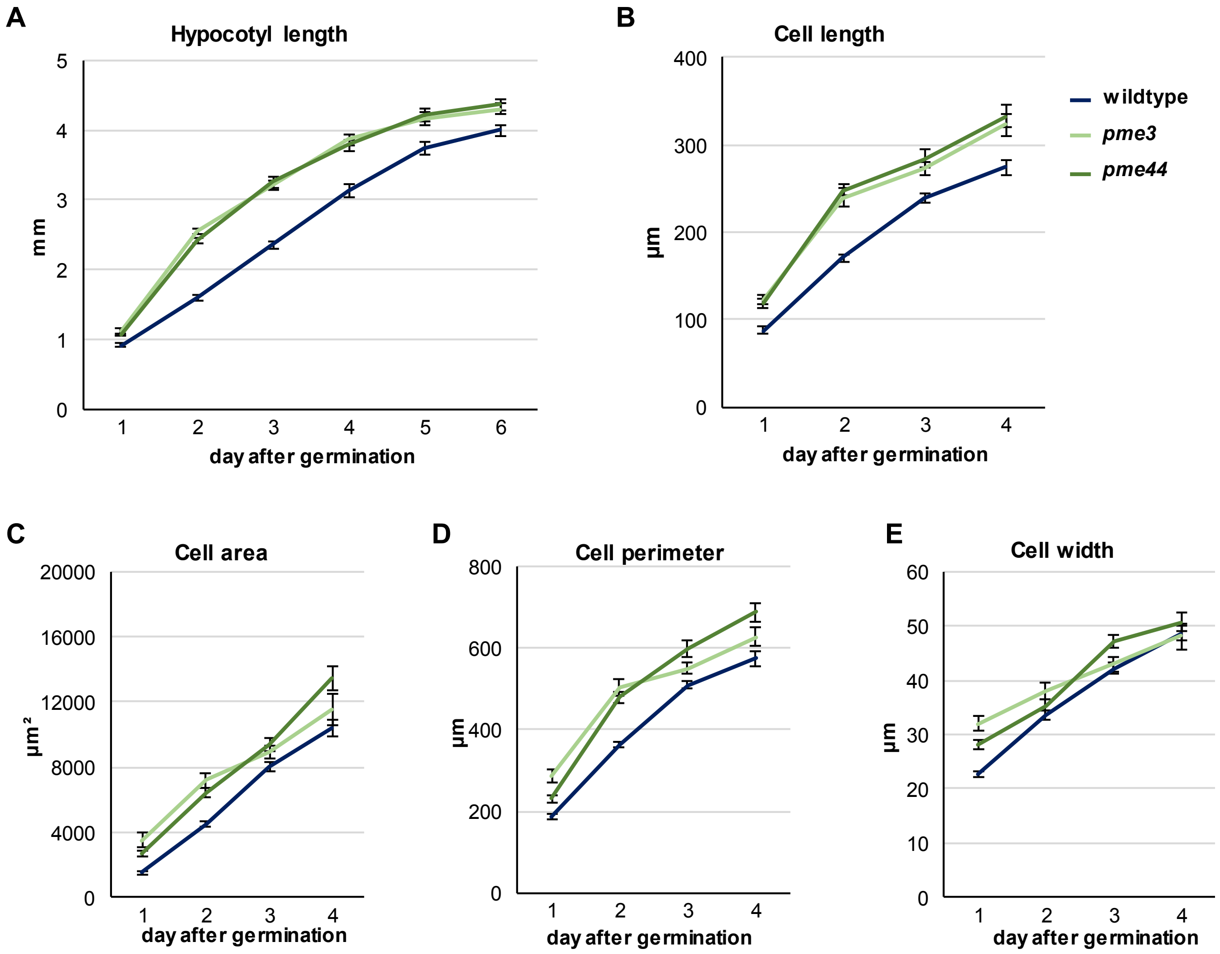

Figure 3.3: Effect of CGA treatment on the elongation of dark-grown hypocotyl and hypocotyl epidermal cells of *Arabidopsis* wildtype, *pme3*, *pme44* and *any1* mutants during elongation.

A and B, length of the hypocotyl (A) and hypocotyl epidermal cells (B). **C - E**, cell area (C), cell perimeter (D) and cell width (E). Error bars represent the standard error. 50 - 60 dark-grown hypocotyls for each time point and 40 – 50 cells from 6 to 8 seedlings for each measurement.

Figure 3.4

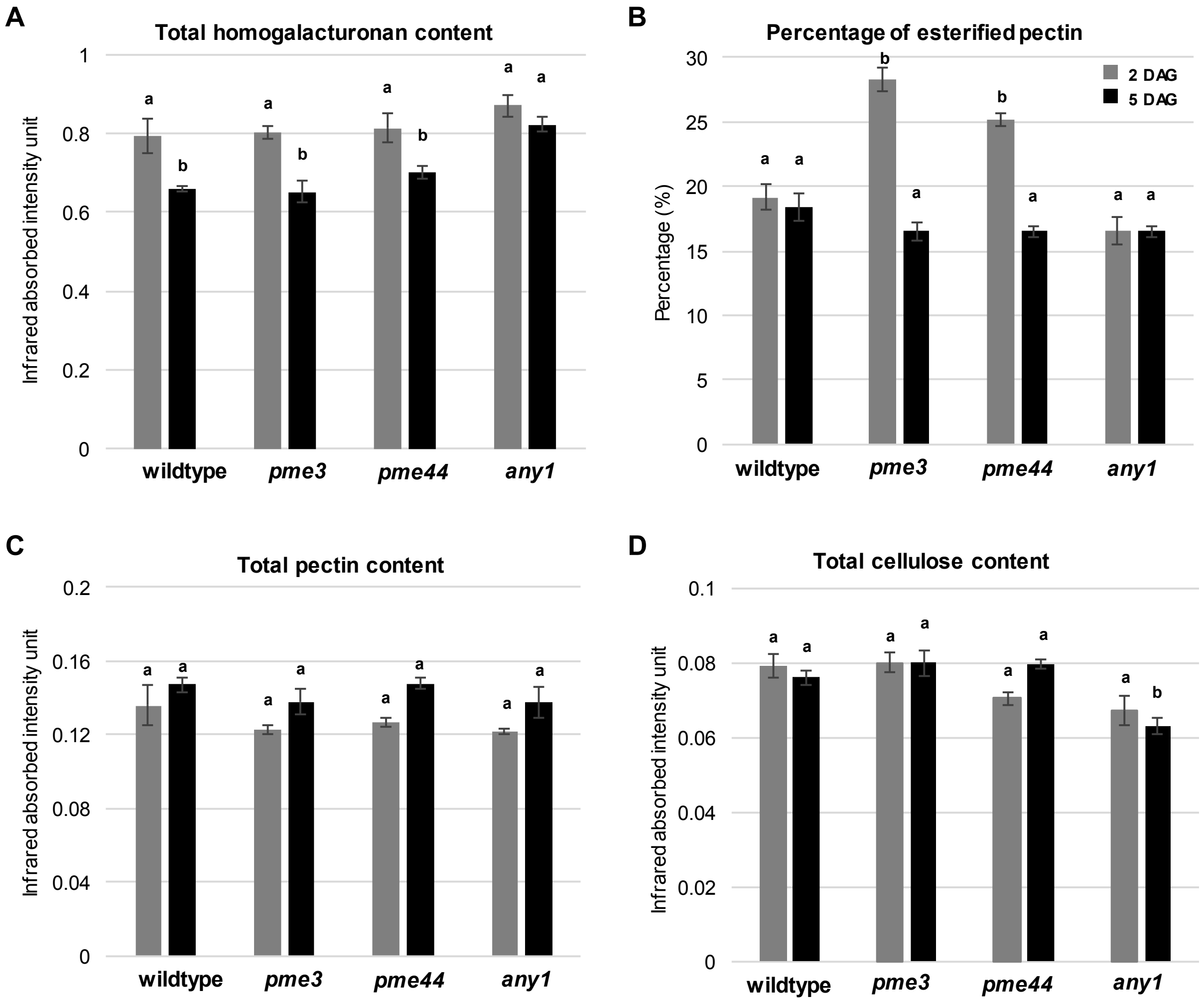

Figure 3.4: Analysis of cell wall components during the elongation of the dark-grown hypocotyl obtained using ATR-FTIR spectroscopy.

A - D, Total homogalacturonan pectin content (A), percentage of esterified pectin (B), total pectin (C), and total cellulose content (C) in the wildtype, *pme3*, *pme44* and *any1* at 2 DAG (gray bars) and 5 DAG (black bars). Letters a and b indicate similarity based on *student's t*-test (0.01 < P < 0.05). Error bars represent standard error. N = 4 or 5 pools of hypocotyls for each measurement.

Figure 3.5

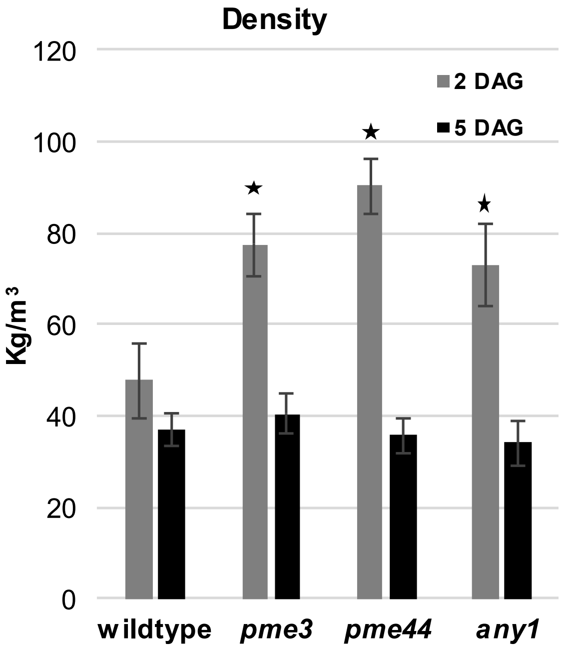

Figure 3.5: Density of hypocotyls in *Arabidopsis* wildtype, *pme3*, *pme44* and *any1* during their elongation.

Gray and black bars represent densities at 2 and 5 DAG, respectively. Asterisks indicate statistically significant differences compared to the wildtype (0.01 < P < 0.05, *student's t*-test). Error bars represent standard error. N = 4 or 5 pools of hypocotyls for each measurement.

Figure 3.6

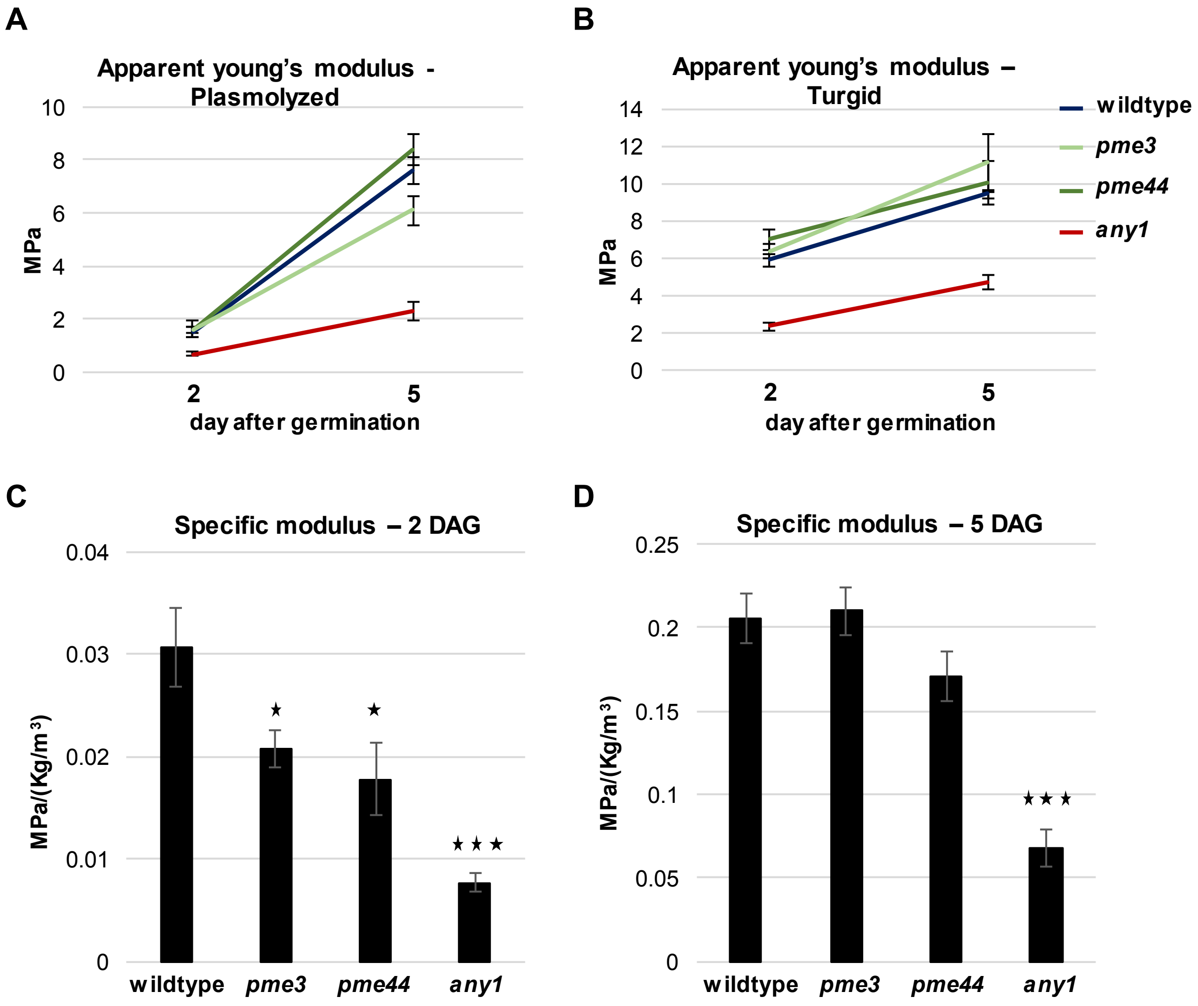

Figure 3.6: Stiffness of dark-grown hypocotyls of *Arabidopsis* wildtype, *pme3*, *pme44* and *any1*.

A and B, Apparent Young's modulus of plasmolyzed (A) and turgid (B). **C and D**, specific modulus at 2 DAG (C) and 5 DAG (D). Error bars represent standard error. Asterisks in C and D indicate statistically significant differences compared to the wildtype (* for $P < 0.05$ and *** for $P < 0.001$, *student's t*-test).

Figure 3.7

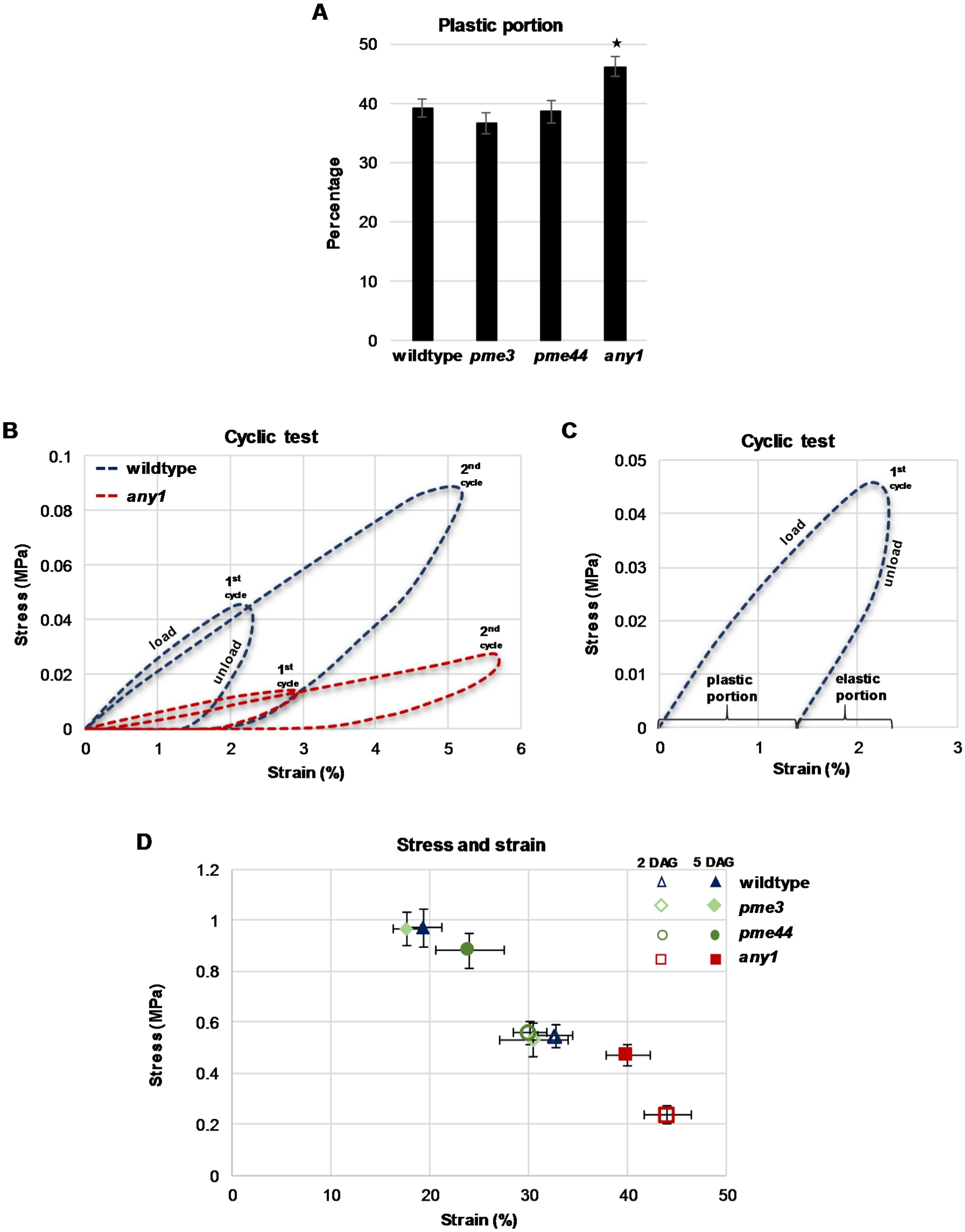

Figure 3.7: Mechanical behavior of dark-grown hypocotyls of *Arabidopsis* wildtype, *pme3*, *pme44* and *any1*.

A, percentage of the plasticity at 2 DAG. **B**, Example of cyclic test showing first two cycles (i.e. 5% stretch) of loading and unloading experiment for dark-grown hypocotyl of wildtype and *any1* mutant. **C**, Plastic and elastic portions are shown for the first cycle (i.e. 2.5% stretch) of loading and unloading experiment for dark-grown hypocotyl of wildtype. **D**, Fracture stress and strain at 2 and 5 DAG. Error bars represent standard error. Asterisks in A indicate statistically significant differences compared to the wildtype (P < 0.05, *student's t*-test).

3.7 Supplemental data

Supplemental movie 3.1

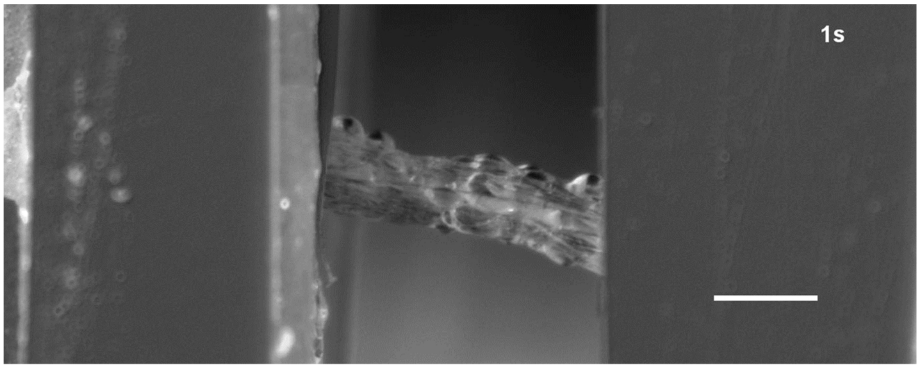

Supplemental movie 3.1: Tensile test of dark-grown turgid hypocotyl of *any1* mutant at 5 DAG. Displacement speed is 100 µm/s. Scale bar = 0.5 mm.

4 Conclusions and perspectives

The morphogenetic differentiation of plants is determined by the pattern of expansion of the individual cells. Several studies have investigated cell expansion by studying cortical cytoskeletal dynamics during cell development (Fu et al., 2005; Armour et al., 2015). Although the cytoskeletal arrays guide the insertion, deposition and synthesis of the wall polymers (Marchant, 1979; Cai, 2011; Kim and Brandizzi, 2014; Szymanski and Staiger, 2018), they cannot inform about changes of cell wall polymers. Therefore, monitoring dynamic modification of wall components is important during the development. In an attempt to understand how cell wall polymers regulate morphogenetic differentiation, I used molecular, imaging, biochemical and biomechanical approaches. I investigated how cellulose and homogalacturonan pectin impact the morphogenesis of epidermal cells of hypocotyls and epidermal pavement cells of cotyledons in *Arabidopsis thaliana*. These two wall polymers may control the expansion as they exhibit mechanical features and can be modified during their synthesis and/or once they are deposited on the wall.

Crystallinity is one of the physiochemical properties of cellulose that can define the interaction of cellulose with other wall polymers through its effect on the hydrophilic and hydrophobic phases of the microfibrils (Cosgrove, 2014; Park and Cosgrove, 2015). By using Brillouin scattering, tensile testing and cyclic testing, I showed that a decrease in cellulose crystallinity is correlated with a decrease in the stiffness and elasticity of the wall. Moreover, I showed that an elevated degree of cellulose crystallinity can promote the anisotropic expansion of the wall in two cases: first, when the crystallinity is coupled with the anisotropic orientation of the microfibrils as during the expansion of the epidermal cells of the hypocotyl, and second, when the crystallinity is controlled spatially. The latter conclusion is drawn from the results of the *any1* mutant and CGA treatment during pavement cell morphogenesis. A higher degree of cellulose crystallinity at the neck region of an undulation may restrict the expansion at that region and, therefore, allow lobe formation. However, it will be important to examine the subcellular variation in the crystallinity during undulation formation. This can be done by electron diffraction using transmission electron microscopy (Chanzy et al., 1978; Sugiyama et al., 1985; Sugiyama et al., 1991). Since this technique is not suitable for live cells, the crystallinity can only be examined at the fully developed neck and lobe regions. The question is how cells can control the degree of cellulose crystallinity during the expansion process? Recent studies suggest that the speed of cellulose synthase movement may be associated with the degree of cellulose crystallinity, as a higher speed of CESA movement is correlated with a higher degree of crystallinity as shown in the *mor1-1* mutant (Fujita et al., 2011; Fujita et al., 2013). Taking advantage of a possible subcellular difference in cellulose crystallinity between lobe and neck regions, a correlation between CESA movement and cellulose crystallinity could be drawn by investigating the speed of CESA at both regions. The regulation of cellulose crystallinity may be mediated by cortical microtubules or by glycophosphatidylinositol (GPI)-anchored proteins such as the COBRA protein. A reduction in microtubule polymer mass decreases cellulose crystallinity (Fujita et al., 2011). On the other hand, COBRA binds with cellulose via an extracellular binding domain and cellulose crystallinity is decreased in *cobra* mutants (Schindelman et al., 2001; Roudier et al., 2005; Liu et al., 2013). However, a genetic screen is warranted to identify direct regulators that control the crystallinity of cellulose during its synthesis.

The epidermal pavement cell is an excellent model to investigate how cell wall polymers are regulated spatially and temporally during the morphogenetic process. Based on alteration of cellulose crystallinity and methylation status of homogalacturonan pectin, I observed two events leading to lobe formation that are differently regulated, an initial and a subsequent expansion event. The initial event is regulated by the de-esterification status of the homogalacturonan pectin and triggers the subsequent expansion event that is regulated by the crystallinity and the orientation of cellulose microfibrils. It is still to be answered what triggers the initial event, and how the de-esterification process is defined at the prospective neck region of the undulation. *In silico* simulation suggests that instability of the wall at a specific spatial region at the junction of the anticlinal and periclinal walls can occur as a result of the internal turgor pressure and cell geometry. This instability may result in deforming or buckling the wall and, therefore, create stress inhomogeneity over the wall (Bidhendi et al., 2019). This, in turn, may trigger the auxin-Rho-GTPase signaling pathway and ultimately pectin modification (Fu et al., 2005; Chen et al., 2015; Majda and Robert, 2018). Although recent studies suggest that microtubules are involved in the modification of wall pectin (Oda et al., 2015; Zhu et al., 2015), live-imaging data from our studies showed that persistence of the cortical microtubules occurs after the visual evidence of pectin modification (Fig. 2.6). Therefore, I propose that cortical actin filaments are involved in the initial event, not as originally thought by promoting the outgrowth of prospective lobe region but instead through pectin modification at the prospective neck region. The relation of actin filaments to cell shape is still poorly understood, maybe because it is highly networked and cannot be easily analyzed and correlated with cell morphogenesis (Szymanski and Staiger, 2018). To examine the role of actin filaments during the early stages of lobe initiation, live-imaging of cortical actin filaments and an analytical method to quantify global cellular changes in actin cytoskeletal dynamics are required, as illustrated by Tolmie et al. (2017). Although I provided a detailed spatiotemporal profile of demethyl-esterified pectin, it would be important to identify through transcripts and protein levels the PMEs that are involved in the esterification process during pavement cell development. The putative candidates can be tested for their interaction with the PMEI that was examined in this study (PMEI37). Tagging the PME of interest with fluorescent protein would be the next step to investigate its spatiotemporal occurrence during undulation formation.

Epidermal cells of the hypocotyl experience different patterns of anisotropic expansion compared to the epidermal pavement cells, however, both cell types share similar sequences of events. Homogalacturonan pectin is involved during the initial steps of the anisotropic expansion and cellulose seems to be important predominantly during the second developmental step, the subsequent elongation process. Recent studies, including the data presented in this thesis, regarding the initial events of pavement cell morphogenesis, indicate that the esterification status of homogalacturonan pectin is as important as the orientation of cellulose microfibrils with respect to the anisotropic expansion, as the esterification process is controlled spatially (Peaucelle et al., 2015; Bou Daher et al., 2018). ATR-FTIR data indicate that a large percentage of the homogalacturonan during the elongation of the dark-grown hypocotyl is demethylated in the wall. However, not all demethylated pectin may be cross-linked with calcium to increase the rigidity of the wall. Calcium may selectively cross-link with demethylated pectin at the short walls of the epidermal cells residing perpendicular to the long axis of the hypocotyl, to prevent an increase in the width of the cell. Detection of calcium in the wall is a key to resolve the selective cross linkage. Monoclonal 2F4 antibodies were used to detect demethyl-esterified pectin cross-linked with calcium. However, because of limited tissue permeability for the antibodies and because the epitopes can be masked, contradictory results were described (Peaucelle et al., 2015; Bou Daher et al., 2018). The presence of calcium in the transverse and axial walls of dark grown hypocotyls of wildtype, *pme* mutants that are presented in this study and *pme* mutants that were examined by Peaucelle et al. (2015) and Bou Daher et al. (2018) can be further done by using scanning transmission X-ray spectromicroscopy (Karunakaran et al., 2015). This technique has a high spatial resolution and has already been used successfully to detect the spatial distribution of calcium ions in the secondary cell wall (Thyrel et al., 2016).

Studying how cell wall polymers regulate cell shape during the morphogenetic process is challenging not only because of the limited availability of tools, such as live-cell imaging, but also because disruption of polysaccharide biosynthesis may activate compensatory mechanisms leading to alteration of other wall components (Ringli, 2010; Hamann and Denness, 2011; Pogorelko et al., 2013). For example, alteration in cellulose synthase leads to an increase in the amount of lignin in the secondary cell wall (Cano-Delgado et al., 2003). Moreover, disruption of pectin synthesis may alter cell to cell adhesion (Bouton et al., 2002; Daher and Braybrook, 2015) thus leading to misjudgment of cell wall stiffness when it is evaluated through conventional mechanical methods such as tensile tests. Therefore, investigating cell wall polymers through mutation or drug-induced disruption requires biochemical and biomechanical approaches in addition to observation of the phenotype.

Recent advances in live-cell imaging techniques are a major step forward in understanding how cell wall polymers regulate the morphogenetic differentiation of plant cells since they allow observations while the expansion process is ongoing. Brillouin microscopy can be used to non-invasively assess cell wall stiffness at subcellular level with light wave resolution limit. Using this method, I was able to map cell wall stiffness at the two sides of the undulation of living cells. As this method is light based, it can be further combined with confocal microscopy and therefore, cell wall modification and cytoskeletal dynamics can be live-monitored together with the changes in the wall stiffness. Brillouin microscopy can be further used to measure the wall stiffness at different angles. As a further advantage, this technique allows to investigate how wall stiffness is changes based on the orientation of cellulose microfibrils. Other live-cell methods for measuring mechanical properties of the cell wall are continuously being developed for cellular and tissue levels such as cellular force microscopy and automated confocal micro-extensometer (Routier-Kierzkowska and Smith, 2013; Robinson et al., 2017). Real-time monitoring of cell wall polymers, for example, cellulose and demethylated pectin, can be done by fluorescent dyes such as S4B and propidium iodide. S4B has a high affinity to cellulose and when bound to cellulose microfibrils it can be used as a proxy to determine their alignment as seen in the epidermal pavement cell and guard cells. Moreover, S4B dye is a stable dye and has been used for super-resolution methods (Liesche et al., 2013). Propidium iodide dye is suitable for live cell imaging and can be used to monitor modifications of homogalacturonan pectin *in muro* (Rounds et al., 2011). To further expand the tool set for real-time monitoring of major cell wall polymers, a library of fluorescent dyes should be screened (Anderson et al., 2010; Rounds et al., 2011; Anderson and Carroll, 2014; Mravec et al., 2014). Another promising approach that allows tracking a single polymer over long periods of time is metabolic labeling (Anderson et al., 2012). This method requires the generation of metabolically tagged polymers through the manipulated synthesis of azide-monosaccharides and alkyne-monosaccharides. In conclusion, the advances in live-cell techniques for wall polymers will improve our understanding of the feedback relationship between wall polymers and the intracellular dynamics in the context of cellular development and differentiation.

References

Abasolo W, Eder M, Yamauchi K, Obel N, Reinecke A, Neumetzler L, Dunlop JW, Mouille G, Pauly M, Höfte H, Burgert I (2009) Pectin may hinder the unfolding of xyloglucan chains during cell deformation: implications of the mechanical performance of Arabidopsis hypocotyls with pectin alterations. *Mol Plant* **2:** 990-999

Altartouri B, Geitmann A (2015) Understanding plant cell morphogenesis requires real-time monitoring of cell wall polymers. *Curr Opin Plant Biol* **23:** 76-82

Anderson CT, Carroll A (2014) Identification and use of fluorescent dyes for plant cell wall imaging using high-throughput screening. *Methods Mol Biol* **1056:** 103-109

Anderson CT, Carroll A, Akhmetova L, Somerville C (2010) Real-time imaging of cellulose reorientation during cell wall expansion in Arabidopsis roots. *Plant Physiol* **152:** 787-796

Anderson CT, Wallace IS, Somerville CR (2012) Metabolic click-labeling with a fucose analog reveals pectin delivery, architecture, and dynamics in Arabidopsis cell walls. *Proc Natl Acad Sci U S A* **109:** 1329-1334

Aouar L, Chebli Y, Geitmann A (2010) Morphogenesis of complex plant cell shapes: the mechanical role of crystalline cellulose in growing pollen tubes. *Sex Plant Reprod* **23:** 15-27

Armour WJ, Barton DA, Law AM, Overall RL (2015) Differential growth in periclinal and anticlinal walls during lobe formation in Arabidopsis cotyledon pavement cells. *Plant Cell* **27:** 2484-2500

Bacete L, Melida H, Miedes E, Molina A (2018) Plant cell wall-mediated immunity: cell wall changes trigger disease resistance responses. *Plant J* **93:** 614-636

Baskin TI (2005) Anisotropic expansion of the plant cell wall. *Annu Rev Cell Dev Biol* **21:** 203-222

Baskin TI, Jensen OE (2013) On the role of stress anisotropy in the growth of stems. *J Exp Bot* **64:** 4697-4707

Belteton S, Sawchuk MG, Donohoe BS, Scarpella E, Szymanski DB (2017) Reassessing the roles of PIN proteins and anticlinal microtubules during pavement cell morphogenesis. *Plant Physiol* **176**:432-449

Bidhendi AJ, Altartouri B, Gosselin FP, Geitmann A (2019) Mechanical stress initiates and sustains the morphogenesis of wavy leaf epidermal cells. *Cell Rep* **28.**

Bidhendi AJ, Geitmann A (2016) Relating the mechanics of the primary plant cell wall to morphogenesis. *J Exp Bot* **67:** 449-461

Bidhendi AJ, Geitmann A (2018) Finite element modeling of shape changes in plant cells. *Plant Physiol* **176:** 41-56

Bidhendi AJ, Geitmann A (2018) Tensile testing of primary plant cells and tissues. *In* Plant Biomechanics. Springer, pp 321-347

Bidhendi AJ, Geitmann A (2019) Geometrical details matter for mechanical modeling of cell morphogenesis. *Dev Cell* **50:** 117-125 e112

Bosch M, Cheung AY, Hepler PK (2005) Pectin methylesterase, a regulator of pollen tube growth. *Plant Physiol* **138:** 1334-1346

Bou Daher F, Chen Y, Bozorg B, Clough J, Jonsson H, Braybrook SA (2018) Anisotropic growth is achieved through the additive mechanical effect of material anisotropy and elastic asymmetry. *Elife* **7**

Bou Daher F, Geitmann A (2011) Actin is involved in pollen tube tropism through redefining the spatial targeting of secretory vesicles. *Traffic* **12:** 1537-1551

Boudaoud A (2010) An introduction to the mechanics of morphogenesis for plant biologists. *Trends Plant Sci* **15:** 353-360

Boudaoud A, Burian A, Borowska-Wykret D, Uyttewaal M, Wrzalik R, Kwiatkowska D, Hamant O (2014) FibrilTool, an ImageJ plug-in to quantify fibrillar structures in raw microscopy images. *Nat Protoc* **9:** 457-463

Bouton S, Leboeuf E, Mouille G, Leydecker MT, Talbotec J, Granier F, Lahaye M, Höfte H, Truong HN (2002) QUASIMODO1 encodes a putative membrane-bound glycosyltransferase required for normal pectin synthesis and cell adhesion in Arabidopsis. *Plant Cell* **14:** 2577-2590

Bukowski N, Pandey JL, Doyle L, Richard TL, Anderson CT, Zhu Y (2014) Development of a clickable designer monolignol for interrogation of lignification in plant cell walls. *Bioconjug Chem* **25:** 2189-2196

Burton RA, Fincher GB (2014) Plant cell wall engineering: applications in biofuel production and improved human health. *Curr Opin Biotechnol* **26:** 79-84

Burton RA, Gidley MJ, Fincher GB (2010) Heterogeneity in the chemistry, structure and function of plant cell walls. *Nat Chem Biol* **6:** 724-732

Caffall KH, Mohnen D (2009) The structure, function, and biosynthesis of plant cell wall pectic polysaccharides. *Carbohydr Res* **344:** 1879-1900

Cai G (2011) How do microtubules affect deposition of cell wall polysaccharides in the pollen tube? *Plant Signal Behav* **6:** 732-735

Cano-Delgado A, Penfield S, Smith C, Catley M, Bevan M (2003) Reduced cellulose synthesis invokes lignification and defense responses in Arabidopsis thaliana. *Plant J* **34:** 351-362

Canteri MHG, Renard C, Le Bourvellec C, Bureau S (2019) ATR-FTIR spectroscopy to determine cell wall composition: Application on a large diversity of fruits and vegetables. *Carbohydr Polym* **212:** 186-196

Carpita NC, Gibeaut DM (1993) Structural models of primary cell walls in flowering plants: consistency of molecular structure with the physical properties of the walls during growth. *Plant J* **3:** 1-30

Chan J (2012) Microtubule and cellulose microfibril orientation during plant cell and organ growth. *J Microsc* **247:** 23-32

Chanzy H, Imada K, Vuong R (1978) Electron diffraction from the primary wall of cotton fibers. *Protoplasma* **94:** 299-306

Chebli Y, Geitmann A (2017) Cellular growth in plants requires regulation of cell wall biochemistry. *Curr Opin Cell Biol* **44:** 28-35

Chebli Y, Kaneda M, Zerzour R, Geitmann A (2012) The cell wall of the Arabidopsis pollen tube--spatial distribution, recycling, and network formation of polysaccharides. *Plant Physiol* **160:** 1940-1955

Chen J, Wang F, Zheng S, Xu T, Yang Z (2015) Pavement cells: a model system for non-transcriptional auxin signalling and crosstalks. *J Exp Bot* **66:** 4957-4970

Cosgrove DJ (1998) Cell wall loosening by expansins. *Plant Physiol* **118:** 333-339

Cosgrove DJ (2005) Growth of the plant cell wall. *Nat Rev Mol Cell Biol* **6:** 850-861

Cosgrove DJ (2014) Re-constructing our models of cellulose and primary cell wall assembly. *Curr Opin Plant Biol* **22:** 122-131

Cosgrove DJ (2016) Plant cell wall extensibility: connecting plant cell growth with cell wall structure, mechanics, and the action of wall-modifying enzymes. *J Exp Bot* **67:** 463-476

Cosgrove DJ (2018) Diffuse growth of plant cell walls. *Plant Physiol* **176:** 16-27

Cosgrove DJ (2018) Nanoscale structure, mechanics and growth of epidermal cell walls. *Curr Opin Plant Biol* **46:** 77-86

Cosgrove DJ, Jarvis MC (2012) Comparative structure and biomechanics of plant primary and secondary cell walls. *Front Plant Sci* **3:** 204

Crowell EF, Bischoff V, Desprez T, Rolland A, Stierhof YD, Schumacher K, Gonneau M, Höfte H, Vernhettes S (2009) Pausing of Golgi bodies on microtubules regulates secretion of cellulose synthase complexes in Arabidopsis. *Plant Cell* **21:** 1141-1154

Crowell EF, Timpano H, Desprez T, Franssen-Verheijen T, Emons AM, Höfte H, Vernhettes S (2011) Differential regulation of cellulose orientation at the inner and outer face of epidermal cells in the Arabidopsis hypocotyl. *Plant Cell* **23:** 2592-2605

Daher FB, Braybrook SA (2015) How to let go: pectin and plant cell adhesion. *Front Plant Sci* **6:** 523

Derbyshire P, McCann MC, Roberts K (2007) Restricted cell elongation in Arabidopsis hypocotyls is associated with a reduced average pectin esterification level. *BMC Plant Biol* **7:** 31

Desprez T, Juraniec M, Crowell EF, Jouy H, Pochylova Z, Parcy F, Höfte H, Gonneau M, Vernhettes S (2007) Organization of cellulose synthase complexes involved in primary cell wall synthesis in Arabidopsis thaliana. *Proc Natl Acad Sci U S A* **104:** 15572-15577

Diddens I, Murphy B, Krisch M, Müller M (2008) Anisotropic elastic properties of cellulose measured using inelastic X-ray scattering. *Macromolecules* **41:** 9755-9759

Dumont M, Lehner A, Vauzeilles B, Malassis J, Marchant A, Smyth K, Linclau B, Baron A, Mas Pons J, Anderson CT, Schapman D, Galas L, Mollet JC, Lerouge P (2016) Plant cell wall imaging by metabolic click-mediated labelling of rhamnogalacturonan II using azido 3-deoxy-D-manno-oct-2-ulosonic acid. *Plant J* **85:** 437-447

Eichhorn S, Young R (2001) The Young's modulus of a microcrystalline cellulose. *Cellulose* **8:** 197-207

Elsayad K, Werner S, Gallemi M, Kong J, Sanchez Guajardo ER, Zhang L, Jaillais Y, Greb T, Belkhadir Y (2016) Mapping the subcellular mechanical properties of live cells in tissues with fluorescence emission-Brillouin imaging. *Sci Signal* **9:** rs5

Elsner J, Lipowczan M, Kwiatkowska D (2018) Differential growth of pavement cells of Arabidopsis thaliana leaf epidermis as revealed by microbead labeling. *Am J Bot* **105:** 257-265

Emons AM, van Maaren N (1987) Helicoidal cell-wall texture in root hairs. *Planta* **170:** 145-151

Eng RC, Sampathkumar A (2018) Getting into shape: the mechanics behind plant morphogenesis. *Curr Opin Plant Biol* **46:** 25-31

Engelsdorf T, Gigli-Bisceglia N, Veerabagu M, McKenna JF, Vaahtera L, Augstein F, Van der Does D, Zipfel C, Hamann T (2018) The plant cell wall integrity maintenance and immune signaling systems cooperate to control stress responses in Arabidopsis thaliana. *Sci Signal* **11**

Fayant P, Girlanda O, Chebli Y, Aubin CE, Villemure I, Geitmann A (2010) Finite element model of polar growth in pollen tubes. *Plant Cell* **22:** 2579-2593

Fu Y, Gu Y, Zheng Z, Wasteneys G, Yang Z (2005) Arabidopsis interdigitating cell growth requires two antagonistic pathways with opposing action on cell morphogenesis. *Cell* **120:** 687-700

Fu Y, Li H, Yang Z (2002) The ROP2 GTPase controls the formation of cortical fine F-actin and the early phase of directional cell expansion during Arabidopsis organogenesis. *Plant Cell* **14:** 777-794

Fujita M, Himmelspach R, Hocart CH, Williamson RE, Mansfield SD, Wasteneys GO (2011) Cortical microtubules optimize cell-wall crystallinity to drive unidirectional growth in Arabidopsis. *Plant J* **66:** 915-928

Fujita M, Himmelspach R, Ward J, Whittington A, Hasenbein N, Liu C, Truong TT, Galway ME, Mansfield SD, Hocart CH, Wasteneys GO (2013) The anisotropy1 D604N mutation in the Arabidopsis cellulose synthase1 catalytic domain reduces cell wall crystallinity and the velocity of cellulose synthase complexes. *Plant Physiol* **162:** 74-85

Fujita M, Wasteneys GO (2014) A survey of cellulose microfibril patterns in dividing, expanding, and differentiating cells of Arabidopsis thaliana. *Protoplasma* **251:** 687-698

Geitmann A (2006) Experimental approaches used to quantify physical parameters at cellular and subcellular levels. *Am J Bot* **93:** 1380-1390

Geitmann A (2010) Mechanical modeling and structural analysis of the primary plant cell wall. *Curr Opin Plant Biol* **13:** 693-699

Geitmann A, Dyson R (2013) Modeling of the primary plant cell wall in the context of plant development. *Cell Biology*: 1-17

Geitmann A, Ortega JK (2009) Mechanics and modeling of plant cell growth. *Trends Plant Sci* **14:** 467-478

Glover BJ (2000) Differentiation in plant epidermal cells. *J Exp Bot* **51:** 497-505

Gonneau M, Höfte H, Vernhettes S (2012) Fluorescent tags to explore cell wall structure and dynamics. *Front Plant Sci* **3:** 145

Guénin S, Hardouin J, Paynel F, Muller K, Mongelard G, Driouich A, Lerouge P, Kermode AR, Lehner A, Mollet JC, Pelloux J, Gutierrez L, Mareck A (2017) AtPME3, a ubiquitous cell wall pectin methylesterase of Arabidopsis thaliana, alters the metabolism of cruciferin seed storage proteins during post-germinative growth of seedlings. *J Exp Bot* **68:** 1083-1095

Guénin S, Mareck A, Rayon C, Lamour R, Assoumou Ndong Y, Domon JM, Senechal F, Fournet F, Jamet E, Canut H, Percoco G, Mouille G, Rolland A, Rusterucci C, Guerineau F, Van Wuytswinkel O, Gillet F, Driouich A, Lerouge P, Gutierrez L, Pelloux J (2011) Identification of pectin methylesterase 3 as a basic pectin methylesterase isoform involved in adventitious rooting in Arabidopsis thaliana. *New Phytol* **192:** 114-126

Gutierrez R, Lindeboom JJ, Paredez AR, Emons AM, Ehrhardt DW (2009) Arabidopsis cortical microtubules position cellulose synthase delivery to the plasma membrane and interact with cellulose synthase trafficking compartments. *Nat Cell Biol* **11:** 797-806

Hamann T, Denness L (2011) Cell wall integrity maintenance in plants: lessons to be learned from yeast? *Plant Signal Behav* **6:** 1706-1709

Hamant O, Heisler MG, Jonsson H, Krupinski P, Uyttewaal M, Bokov P, Corson F, Sahlin P, Boudaoud A, Meyerowitz EM, Couder Y, Traas J (2008) Developmental patterning by mechanical signals in Arabidopsis. *Science* **322:** 1650-1655

Harholt J, Suttangkakul A, Vibe Scheller H (2010) Biosynthesis of pectin. *Plant Physiol* **153:** 384-395

Hepler PK, Rounds CM, Winship LJ (2013) Control of cell wall extensibility during pollen tube growth. *Mol Plant* **6:** 998-1017

Higaki T, Takigawa-Imamura H, Akita K, Kutsuna N, Kobayashi R, Hasezawa S, Miura T (2017) Exogenous cellulase switches cell interdigitation to cell elongation in an RIC1-dependent manner in Arabidopsis thaliana cotyledon pavement cells. *Plant Cell Physiol* **58:** 106-119

Himmelspach R, Williamson RE, Wasteneys GO (2003) Cellulose microfibril alignment recovers from DCB-induced disruption despite microtubule disorganization. *Plant J* **36:** 565-575

Hocq L, Pelloux J, Lefebvre V (2017) Connecting homogalacturonan-type pectin remodeling to acid growth. *Trends Plant Sci* **22:** 20-29

Hongo S, Sato K, Yokoyama R, Nishitani K (2012) Demethylesterification of the primary wall by PECTIN METHYLESTERASE35 provides mechanical support to the Arabidopsis stem. *Plant Cell* **24:** 2624-2634

Hooke R (1667) Micrographia, or, Some physiological descriptions of minute bodies made by magnifying glasses : with observations and inquiries thereupon. London : Printed for Jo. Martyn, and Ja. Allestry, MDCLXV11 [1667]

Jacques E, Verbelen J-P, Vissenberg K (2014) Review on shape formation in epidermal pavement cells of the Arabidopsis leaf. *Functional Plant Biology* **41:** 914-921

Jacques E, Verbelen JP, Vissenberg K (2013) Mechanical stress in Arabidopsis leaves orients microtubules in a 'continuous' supracellular pattern. *BMC Plant Biol* **13:** 163

Kafle K, Xi X, Lee CM, Tittmann BR, Cosgrove DJ, Park YB, Kim SH (2014) Cellulose microfibril orientation in onion (Allium cepa L.) epidermis studied by atomic force microscopy (AFM) and vibrational sum frequency generation (SFG) spectroscopy. *Cellulose* **21:** 1075-1086

Karunakaran C, Christensen CR, Gaillard C, Lahlali R, Blair LM, Perumal V, Miller SS, Hitchcock AP (2015) Introduction of soft X-ray spectromicroscopy as an advanced technique for plant biopolymers research. *PLoS One* **10:** e0122959

Keegstra K (2010) Plant cell walls. *Plant Physiol* **154:** 483-486

Kerstens S, Decraemer WF, Verbelen JP (2001) Cell walls at the plant surface behave mechanically like fiber-reinforced composite materials. *Plant Physiol* **127:** 381-385

Kim SJ, Brandizzi F (2014) The plant secretory pathway: an essential factory for building the plant cell wall. *Plant Cell Physiol* **55:** 687-693

Knox JP, Linstead PJ, King J, Cooper C, Roberts K (1990) Pectin esterification is spatially regulated both within cell walls and between developing tissues of root apices. *Planta* **181:** 512-521

Kotzer A, Wasteneys G (2006) Mechanisms behind the puzzle: microtubule–microfilament cross-talk in pavement cell formation. *Botany* **84:** 594-603

Krupkova E, Immerzeel P, Pauly M, Schmulling T (2007) The TUMOROUS SHOOT DEVELOPMENT2 gene of Arabidopsis encoding a putative methyltransferase is required for cell adhesion and co-ordinated plant development. *Plant J* **50:** 735-750

Lahlali R, Jiang Y, Kumar S, Karunakaran C, Liu X, Borondics F, Hallin E, Bueckert R (2014) ATR-FTIR spectroscopy reveals involvement of lipids and proteins of intact pea pollen grains to heat stress tolerance. *Front Plant Sci* **5:** 747

Lampugnani ER, Khan GA, Somssich M, Persson S (2018) Building a plant cell wall at a glance. *J Cell Sci* **131**

Laughlin ST, Bertozzi CR (2009) Imaging the glycome. *Proc Natl Acad Sci U S A* **106:** 12-17

Lee GY, Cheung K, Chang W, Lee LP (2000) Mechanical interlocking with precisely controlled nano-and microscale geometries for implantable microdevices. *In* 1st Annual International IEEE-EMBS Special Topic Conference on Microtechnologies in Medicine and Biology. Proceedings (Cat. No. 00EX451). IEEE, pp 537-541

Lee Y, Karunakaran C, Lahlali R, Liu X, Tanino KK, Olsen JE (2017) Photoperiodic Regulation of Growth-Dormancy Cycling through Induction of Multiple Bud-Shoot Barriers Preventing Water Transport into the Winter Buds of Norway Spruce. *Front Plant Sci* **8:** 2109

Levesque-Tremblay G, Pelloux J, Braybrook SA, Muller K (2015) Tuning of pectin methylesterification: consequences for cell wall biomechanics and development. *Planta* **242:** 791-811

Li S, Lei L, Somerville CR, Gu Y (2012) Cellulose synthase interactive protein 1 (CSI1) links microtubules and cellulose synthase complexes. *Proc Natl Acad Sci U S A* **109:** 185-190

Liesche J, Ziomkiewicz I, Schulz A (2013) Super-resolution imaging with Pontamine Fast Scarlet 4BS enables direct visualization of cellulose orientation and cell connection architecture in onion epidermis cells. *BMC Plant Biol* **13:** 226

Liu L, Shang-Guan K, Zhang B, Liu X, Yan M, Zhang L, Shi Y, Zhang M, Qian Q, Li J, Zhou Y (2013) Brittle Culm1, a COBRA-like protein, functions in cellulose assembly through binding cellulose microfibrils. *PLoS Genet* **9:** e1003704

Loque D, Scheller HV, Pauly M (2015) Engineering of plant cell walls for enhanced biofuel production. *Curr Opin Plant Biol* **25:** 151-161

Majda M, Grones P, Sintorn IM, Vain T, Milani P, Krupinski P, Zagorska-Marek B, Viotti C, Jonsson H, Mellerowicz EJ, Hamant O, Robert S (2017) Mechanochemical polarization of contiguous cell Walls shapes plant pavement cells. *Dev Cell* **43:** 290-304 e294

Majda M, Robert S (2018) The role of auxin in cell wall expansion. *Int J Mol Sci* **19**

Majda M, Krupinski P, Jönsson H, Hamant O, Robert S (2019) Mechanical asymmetry of the cell wall predicts changes in pavement cell geometry. *Dev Cell* **50**: 9–10

Marchant HJ (1979) Microtubules, cell wall deposition and the determination of plant cell shape. *Nature* **278:** 167

McKenna ST, Kunkel JG, Bosch M, Rounds CM, Vidali L, Winship LJ, Hepler PK (2009) Exocytosis precedes and predicts the increase in growth in oscillating pollen tubes. *Plant Cell* **21:** 3026-3040

Mehta SB, McQuilken M, La Riviere PJ, Occhipinti P, Verma A, Oldenbourg R, Gladfelter AS, Tani T (2016) Dissection of molecular assembly dynamics by tracking orientation and position of single molecules in live cells. *Proc Natl Acad Sci U S A* **113:** E6352-E6361

Milani P, Braybrook SA, Boudaoud A (2013) Shrinking the hammer: micromechanical approaches to morphogenesis. *J Exp Bot* **64:** 4651-4662

Mohnen D (2008) Pectin structure and biosynthesis. *Curr Opin Plant Biol* **11:** 266-277

Mollet JC, Kim S, Jauh GY, Lord EM (2002) Arabinogalactan proteins, pollen tube growth, and the reversible effects of Yariv phenylglycoside. *Protoplasma* **219:** 89-98

Mouille G, Ralet MC, Cavelier C, Eland C, Effroy D, Hematy K, McCartney L, Truong HN, Gaudon V, Thibault JF, Marchant A, Höfte H (2007) Homogalacturonan synthesis in Arabidopsis thaliana requires a Golgi-localized protein with a putative methyltransferase domain. *Plant J* **50:** 605-614

Mravec J, Kracun SK, Rydahl MG, Westereng B, Miart F, Clausen MH, Fangel JU, Daugaard M, Van Cutsem P, De Fine Licht HH, Höfte H, Malinovsky FG, Domozych DS, Willats WG (2014) Tracking developmentally regulated post-synthetic processing of homogalacturonan and chitin using reciprocal oligosaccharide probes. *Development* **141:** 4841-4850

Ngouemazong DE, Jolie RP, Cardinaels R, Fraeye I, Van Loey A, Moldenaers P, Hendrickx M (2012) Stiffness of Ca(2+)-pectin gels: combined effects of degree and pattern of methylesterification for various Ca(2+) concentrations. *Carbohydr Res* **348:** 69-76

Oda Y, Iida Y, Nagashima Y, Sugiyama Y, Fukuda H (2015) Novel coiled-coil proteins regulate exocyst association with cortical microtubules in xylem cells via the conserved oligomeric golgi-complex 2 protein. *Plant Cell Physiol* **56:** 277-286

Pabst M, Fischl RM, Brecker L, Morelle W, Fauland A, Kofeler H, Altmann F, Leonard R (2013) Rhamnogalacturonan II structure shows variation in the side chains monosaccharide composition and methylation status within and across different plant species. *Plant J* **76:** 61-72

Palin R, Geitmann A (2012) The role of pectin in plant morphogenesis. *Biosystems* **109:** 397-402

Pandey JL, Kiemle SN, Richard TL, Zhu Y, Cosgrove DJ, Anderson CT (2016) Investigating Biochemical and Developmental Dependencies of Lignification with a Click-Compatible Monolignol Analog in Arabidopsis thaliana Stems. *Front Plant Sci* **7:** 1309

Pandey JL, Wang B, Diehl BG, Richard TL, Chen G, Anderson CT (2015) A versatile click-compatible monolignol probe to study lignin deposition in plant cell walls. *PLoS One* **10:** e0121334

Panteris E, Apostolakos P, Galatis B (1994) Sinuous ordinary epidermal cells: behind several patterns of waviness, a common morphogenetic mechanism. *New phytologist* **127:** 771-780

Panteris E, Galatis B (2005) The morphogenesis of lobed plant cells in the mesophyll and epidermis: organization and distinct roles of cortical microtubules and actin filaments. *New Phytol* **167:** 721-732

Paredez AR, Somerville CR, Ehrhardt DW (2006) Visualization of cellulose synthase demonstrates functional association with microtubules. *Science* **312:** 1491-1495

Park YB, Cosgrove DJ (2012) Changes in cell wall biomechanical properties in the xyloglucan-deficient xxt1/xxt2 mutant of Arabidopsis. *Plant Physiol* **158:** 465-475

Park YB, Cosgrove DJ (2012) A revised architecture of primary cell walls based on biomechanical changes induced by substrate-specific endoglucanases. *Plant Physiol* **158:** 1933-1943

Park YB, Cosgrove DJ (2015) Xyloglucan and its interactions with other components of the growing cell wall. *Plant Cell Physiol* **56:** 180-194

Pattathil S, Avci U, Baldwin D, Swennes AG, McGill JA, Popper Z, Bootten T, Albert A, Davis RH, Chennareddy C, Dong R, O'Shea B, Rossi R, Leoff C, Freshour G, Narra R, O'Neil M, York WS, Hahn MG (2010) A comprehensive toolkit of plant cell wall glycan-directed monoclonal antibodies. *Plant Physiol* **153:** 514-525

Peaucelle A, Braybrook S, Höfte H (2012) Cell wall mechanics and growth control in plants: the role of pectins revisited. *Front Plant Sci* **3:** 121

Peaucelle A, Braybrook SA, Le Guillou L, Bron E, Kuhlemeier C, Höfte H (2011) Pectin-induced changes in cell wall mechanics underlie organ initiation in Arabidopsis. *Curr Biol* **21:** 1720-1726

Peaucelle A, Wightman R, Höfte H (2015) The control of growth symmetry breaking in the Arabidopsis hypocotyl. *Curr Biol* **25:** 1746-1752

Pelletier S, Van Orden J, Wolf S, Vissenberg K, Delacourt J, Ndong YA, Pelloux J, Bischoff V, Urbain A, Mouille G, Lemonnier G, Renou JP, Höfte H (2010) A role for pectin de-methylesterification in a developmentally regulated growth acceleration in dark-grown Arabidopsis hypocotyls. *New Phytol* **188:** 726-739

Peng L, Xiang F, Roberts E, Kawagoe Y, Greve LC, Kreuz K, Delmer DP (2001) The experimental herbicide CGA 325'615 inhibits synthesis of crystalline cellulose and causes accumulation of non-crystalline beta-1,4-glucan associated with CesA protein. *Plant Physiol* **126:** 981-992

Phyo P, Wang T, Kiemle SN, O'Neill H, Pingali SV, Hong M, Cosgrove DJ (2017) Gradients in wall mechanics and polysaccharides along growing inflorescence stems. *Plant Physiol* **175:** 1593-1607

Pique N, Gomez-Guillen MDC, Montero MP (2018) Xyloglucan, a plant polymer with barrier protective properties over the mucous membranes: an overview. *Int J Mol Sci* **19**

Pogorelko G, Lionetti V, Bellincampi D, Zabotina O (2013) Cell wall integrity: targeted post-synthetic modifications to reveal its role in plant growth and defense against pathogens. *Plant Signal Behav* **8**

Prescher JA, Bertozzi CR (2005) Chemistry in living systems. *Nat Chem Biol* **1:** 13-21

Preston RD (1982) The case for multinet growth in growing walls of plant cells. *Planta* **155:** 356-363

Quesada Cabrera R, Meersman F, McMillan PF, Dmitriev V (2011) Nanomechanical and structural properties of native cellulose under compressive stress. *Biomacromolecules* **12:** 2178-2183

Refregier G, Pelletier S, Jaillard D, Höfte H (2004) Interaction between wall deposition and cell elongation in dark-grown hypocotyl cells in Arabidopsis. *Plant Physiol* **135:** 959-968

Ringli C (2010) Monitoring the outside: cell wall-sensing mechanisms. *Plant Physiol* **153:** 1445-1452

Robinson S, Huflejt M, Barbier de Reuille P, Braybrook SA, Schorderet M, Reinhardt D, Kuhlemeier C (2017) An automated confocal micro-extensometer enables in Vivo quantification of mechanical properties with cellular resolution. *Plant Cell* **29:** 2959-2973

Roudier F, Fernandez AG, Fujita M, Himmelspach R, Borner GH, Schindelman G, Song S, Baskin TI, Dupree P, Wasteneys GO, Benfey PN (2005) COBRA, an Arabidopsis extracellular glycosyl-phosphatidyl inositol-anchored protein, specifically controls highly anisotropic expansion through its involvement in cellulose microfibril orientation. *Plant Cell* **17:** 1749-1763

Rounds CM, Lubeck E, Hepler PK, Winship LJ (2011) Propidium iodide competes with Ca(2+) to label pectin in pollen tubes and Arabidopsis root hairs. *Plant Physiol* **157:** 175-187

Routier-Kierzkowska AL, Smith RS (2013) Measuring the mechanics of morphogenesis. *Curr Opin Plant Biol* **16:** 25-32

Ryden P, Sugimoto-Shirasu K, Smith AC, Findlay K, Reiter WD, McCann MC (2003) Tensile properties of Arabidopsis cell walls depend on both a xyloglucan cross-linked microfibrillar network and rhamnogalacturonan II-borate complexes. *Plant Physiol* **132:** 1033-1040

Sampathkumar A, Gutierrez R, McFarlane HE, Bringmann M, Lindeboom J, Emons AM, Samuels L, Ketelaar T, Ehrhardt DW, Persson S (2013) Patterning and lifetime of plasma membrane-localized cellulose synthase is dependent on actin organization in Arabidopsis interphase cells. *Plant Physiol* **162:** 675-688

Sampathkumar A, Krupinski P, Wightman R, Milani P, Berquand A, Boudaoud A, Hamant O, Jonsson H, Meyerowitz EM (2014) Subcellular and supracellular mechanical stress prescribes cytoskeleton behavior in Arabidopsis cotyledon pavement cells. *Elife (Cambridge)* **3:** e01967

Sanati Nezhad A, Geitmann A (2014) Tip growth in walled cells: Cellular expansion and invasion mechanisms. *In* C Cuerrier, A Pelling, eds, Cells, Forces and the Microenvironment. Pan Stanford Publishing Pte Ltd

Sapala A, Runions A, Routier-Kierzkowska AL, Das Gupta M, Hong L, Hofhuis H, Verger S, Mosca G, Li CB, Hay A, Hamant O, Roeder AH, Tsiantis M, Prusinkiewicz P, Smith RS (2018) Why plants make puzzle cells, and how their shape emerges. *Elife* **7**

Saxe F, Weichold S, Reinecke A, Lisec J, Doring A, Neumetzler L, Burgert I, Eder M (2016) Age effects on hypocotyl mechanics. *PLoS One* **11:** e0167808

Scarcelli G, Kim P, Yun SH (2011) In vivo measurement of age-related stiffening in the crystalline lens by Brillouin optical microscopy. *Biophys J* **101:** 1539-1545

Scarcelli G, Polacheck WJ, Nia HT, Patel K, Grodzinsky AJ, Kamm RD, Yun SH (2015) Noncontact three-dimensional mapping of intracellular hydromechanical properties by Brillouin microscopy. *Nat Methods* **12:** 1132-1134

Scarcelli G, Yun SH (2007) Confocal Brillouin microscopy for three-dimensional mechanical imaging. *Nat Photonics* **2:** 39-43

Scarcelli G, Yun SH (2011) Multistage VIPA etalons for high-extinction parallel Brillouin spectroscopy. *Opt Express* **19:** 10913-10922

Scheller HV, Ulvskov P (2010) Hemicelluloses. *Annu Rev Plant Biol* **61:** 263-289

Schindelman G, Morikami A, Jung J, Baskin TI, Carpita NC, Derbyshire P, McCann MC, Benfey PN (2001) COBRA encodes a putative GPI-anchored protein, which is polarly localized and necessary for oriented cell expansion in Arabidopsis. *Genes Dev* **15:** 1115-1127

Schopfer P (2006) Biomechanics of plant growth. *Am J Bot* **93:** 1415-1425

Sebastian J, Ravi M, Andreuzza S, Panoli AP, Marimuthu MP, Siddiqi I (2009) The plant adherin AtSCC2 is required for embryogenesis and sister-chromatid cohesion during meiosis in Arabidopsis. *Plant J* **59:** 1-13

Siegrist MS, Whiteside S, Jewett JC, Aditham A, Cava F, Bertozzi CR (2013) (D)-Amino acid chemical reporters reveal peptidoglycan dynamics of an intracellular pathogen. *ACS Chem Biol* **8:** 500-505

Somerville C (2006) Cellulose synthesis in higher plants. *Annu Rev Cell Dev Biol* **22:** 53-78

Sotiriou P, Giannoutsou E, Panteris E, Galatis B, Apostolakos P (2018) Local differentiation of cell wall matrix polysaccharides in sinuous pavement cells: its possible involvement in the flexibility of cell shape. *Plant Biol (Stuttg)* **20:** 223-237

Sugimoto K, Himmelspach R, Williamson RE, Wasteneys GO (2003) Mutation or drug-dependent microtubule disruption causes radial swelling without altering parallel cellulose microfibril deposition in Arabidopsis root cells. *Plant Cell* **15:** 1414-1429

Sugiyama J, Harada H, Fujiyoshi Y, Uyeda N (1985) Lattice images from ultrathin sections of cellulose microfibrils in the cell wall of Valonia macrophysa Kutz. *Planta* **166:** 161-168

Sugiyama J, Vuong R, Chanzy H (1991) Electron diffraction study on the two crystalline phases occurring in native cellulose from an algal cell wall. *Macromolecules* **24:** 4168-4175

Suslov D, Verbelen JP (2006) Cellulose orientation determines mechanical anisotropy in onion epidermis cell walls. *J Exp Bot* **57:** 2183-2192

Swaminathan V, Kalappurakkal JM, Mehta SB, Nordenfelt P, Moore TI, Koga N, Baker DA, Oldenbourg R, Tani T, Mayor S, Springer TA, Waterman CM (2017) Actin retrograde flow actively aligns and orients ligand-engaged integrins in focal adhesions. *Proc Natl Acad Sci U S A* **114:** 10648-10653

Szymanski D, Staiger CJ (2018) The actin cytoskeleton: functional arrays for cytoplasmic organization and cell shape control. *Plant Physiol* **176:** 106-118

Szymanski DB (2014) The kinematics and mechanics of leaf expansion: new pieces to the Arabidopsis puzzle. *Curr Opin Plant Biol* **22:** 141-148

Szymanski DB, Cosgrove DJ (2009) Dynamic coordination of cytoskeletal and cell wall systems during plant cell morphogenesis. *Curr Biol* **19:** R800-811

Taiz L (1984) Plant cell expansion: regulation of cell wall mechanical properties. *Annual review of plant physiology* **35:** 585-657

Thomas J, Idris NA, Collings DA (2017) Pontamine fast scarlet 4B bifluorescence and measurements of cellulose microfibril angles. *J Microsc* **268:** 13-27

Thomas LH, Forsyth VT, Sturcova A, Kennedy CJ, May RP, Altaner CM, Apperley DC, Wess TJ, Jarvis MC (2013) Structure of cellulose microfibrils in primary cell walls from collenchyma. *Plant Physiol* **161:** 465-476

Thompson DS (2005) How do cell walls regulate plant growth? *J Exp Bot* **56:** 2275-2285

Thyrel M, Backman R, Thånell K, Karunakaran C, Skyllberg U, Lestander TA (2016) Nanomapping and speciation of C and Ca in thermally treated lignocellulosic cell walls using scanning transmission X-ray microscopy and K-edge XANES. *Fuel* **167:** 149-157

Tian GW, Chen MH, Zaltsman A, Citovsky V (2006) Pollen-specific pectin methylesterase involved in pollen tube growth. *Dev Biol* **294:** 83-91

Tolmie F, Poulet A, McKenna J, Sassmann S, Graumann K, Deeks M, Runions J (2017) The cell wall of Arabidopsis thaliana influences actin network dynamics. *J Exp Bot* **68:** 4517-4527

Verbelen J-P, Vissenberg K, Kerstens S, Le J (2001) Cell expansion in the epidermis: microtubules, cellulose orientation and wall loosening enzymes. *Journal of Plant Physiology* **158:** 537-543

Verhertbruggen Y, Marcus SE, Chen J, Knox JP (2013) Cell wall pectic arabinans influence the mechanical properties of Arabidopsis thaliana inflorescence stems and their response to mechanical stress. *Plant Cell Physiol* **54:** 1278-1288

Verhertbruggen Y, Marcus SE, Haeger A, Verhoef R, Schols HA, McCleary BV, McKee L, Gilbert HJ, Knox JP (2009) Developmental complexity of arabinan polysaccharides and their processing in plant cell walls. *Plant J* **59:** 413-425

Vofely RV, Gallagher J, Pisano GD, Bartlett M, Braybrook SA (2019) Of puzzles and pavements: a quantitative exploration of leaf epidermal cell shape. *New Phytol* **221:** 540-552

Wan JX, Zhu XF, Wang YQ, Liu LY, Zhang BC, Li GX, Zhou YH, Zheng SJ (2018) Xyloglucan fucosylation modulates arabidopsis Cell wall hemicellulose aluminium binding capacity. *Sci Rep* **8:** 428

Wang B, McClosky DD, Anderson CT, Chen G (2016) Synthesis of a suite of click-compatible sugar analogs for probing carbohydrate metabolism. *Carbohydr Res* **433:** 54-62

Wang T, Park YB, Caporini MA, Rosay M, Zhong L, Cosgrove DJ, Hong M (2013) Sensitivity-enhanced solid-state NMR detection of expansin's target in plant cell walls. *Proc Natl Acad Sci U S A* **110:** 16444-16449

Wang T, Zabotina O, Hong M (2012) Pectin-cellulose interactions in the Arabidopsis primary cell wall from two-dimensional magic-angle-spinning solid-state nuclear magnetic resonance. *Biochemistry* **51:** 9846-9856

Wei C, Lintilhac LS, Lintilhac PM (2006) Loss of stability, pH, and the anisotropic extensibility of Chara cell walls. *Planta* **223:** 1058-1067

Winter D, Vinegar B, Nahal H, Ammar R, Wilson GV, Provart NJ (2007) An "Electronic Fluorescent Pictograph" browser for exploring and analyzing large-scale biological data sets. *PLoS One* **2:** e718

Wu TC, Belteton SA, Pack J, Szymanski DB, Umulis DM (2016) LobeFinder: a convex Hull-based method for quantitative boundary analyses of lobed plant cells. *Plant Physiol* **171:** 2331-2342

Yanagisawa M, Alonso JM, Szymanski DB (2018) Microtubule-dependent confinement of a cell signaling and actin polymerization control module regulates polarized cell growth. *Curr Biol* **28:** 2459-2466 e2454

Yanagisawa M, Desyatova AS, Belteton SA, Mallery EL, Turner JA, Szymanski DB (2015) Patterning mechanisms of cytoskeletal and cell wall systems during leaf trichome morphogenesis. *Nat Plants* **1:** 15014

Yi H, Rui Y, Kandemir B, Wang JZ, Anderson CT, Puri VM (2018) Mechanical effects of cellulose, xyloglucan, and pectins on stomatal guard cells of Arabidopsis thaliana. *Front Plant Sci* **9:** 1566

Yun SH, Chernyak D (2018) Brillouin microscopy: assessing ocular tissue biomechanics. *Curr Opin Ophthalmol* **29:** 299-305

Zerzour R, Kroeger J, Geitmann A (2009) Polar growth in pollen tubes is associated with spatially confined dynamic changes in cell mechanical properties. *Dev Biol* **334:** 437-446

Zhang C, Halsey LE, Szymanski DB (2011) The development and geometry of shape change in Arabidopsis thaliana cotyledon pavement cells. *BMC Plant Biol* **11:** 27

Zhang T, Mahgsoudy-Louyeh S, Tittmann B, Cosgrove DJ (2014) Visualization of the nanoscale pattern of recently-deposited cellulose microfibrils and matrix materials in never-dried primary walls of the onion epidermis. *Cellulose* **21:** 853-862

Zhu C, Ganguly A, Baskin TI, McClosky DD, Anderson CT, Foster C, Meunier KA, Okamoto R, Berg H, Dixit R (2015) The fragile Fiber1 kinesin contributes to cortical microtubule-mediated trafficking of cell wall components. *Plant Physiol* **167:** 780-792

Zykwinska A, Thibault JF, Ralet MC (2007) Organization of pectic arabinan and galactan side chains in association with cellulose microfibrils in primary cell walls and related models envisaged. *J Exp Bot* **58:** 1795-1802